9-1-2000

A Study of the effects of strain on NiTi shape memory alloy

Bret Oltmans

A STUDY OF THE EFFECTS OF STRAIN ON NiTi SHAPE MEMORY ALLOY

by

Bret Allen Oltmans

**A Thesis Submitted in
Partial Fulfillment of the
Requirement for the**

MASTER OF SCIENCE
IN
MECHANICAL ENGINEERING

Approved by:

Dr. Surendra K. Gupta _____
Department of Mechanical Engineering (Thesis advisor)

Dr. Hany Ghoneim _____
Department of Mechanical Engineering

Dr. Andreas Langner _____
Department of Chemistry

Dr. Satish G. Kandlikar _____
Department Head of Mechanical Engineering

**DEPARTMENT OF MECHANICAL ENGINEERING
ROCHESTER INSTITUTE OF TECHNOLOGY**

September, 2000

Thesis Reproduction Permission Statement

A Study of the Effects of Strain on NiTi Shape Memory Alloy

I, Bret Oltmans, hereby grant permission to the Wallace Library of the Rochester Institute of Technology to reproduce my thesis in whole or in part. Any reproduction will not be for commercial use or profit.

Date: 10/23/2000 **Signature of Author:** _____

Abstract

Shape memory alloys are materials that are capable of returning to an original shape after large deformations in response to a stimulus. Shape memory alloys can be metals, ceramics, polymers and gels. This thesis studies the changes of various properties of NiTi metal as samples are prestrained various amounts. After conducting various characterization techniques, relationships were developed for the changes in transformation temperatures, Knoop hardness number, and crystal lattice parameters.

Through the use of differential scanning calorimetry and dynamic mechanical analysis the transformation temperatures were determined. It was observed in both experiments that the initial austenite start temperature(A_s) increased parabolically while austenite finish temperature (A_f)increased linearly with prestrain. Also, DSC showed that Martensite start temperature (M_s) increased linearly with prestrain, however, DMA did not show any trend for M_s.

Knoop hardness tests as well as deformation tests were performed to investigate changes in the mechanical properties of NiTi with increased prestrain. It was found that the Knoop hardness number increased linearly with increased prestrain. Additionally, from tensile data collected during the deformation testing, it was found that the maximum flow stress at each strain amount follows a parabolic trend. Also from the stress-strain data, it was found that NiTi has a higher strain hardening coefficient than most materials. When Knoop hardness numbers were compared to the true stress values, it was found that the hardness number increased following a cubic trend with increasing stress.

Using X-Ray diffracton, the crystal structure of the NiTi was found to be monoclinic with lattice parameters, a = 2.884, b = 4.637, c = 4.101, $\gamma = 97.7°$. It was also observed that the volume of the unit cell remained constant regardless of prestrain.

Using an optical microscope, large grains with stripes perpendicular to the prestrain direction were observed. The occurrence and size of these grains increased with the amount of prestrain. Surface scans using atomic force microscopy showed that these stripes were all approximately the same depth and regularly spaced. These grains appeared to be self-accommodated martensite regions but could not be fully characterized using these experiments.

Acknowledgements

First I would like to say a huge thank you to my family and friends for supporting me through the ups and downs of my research.

I also owe a debt of gratitude to Dr. Gupta for serving as my thesis advisor. Without his extensive knowledge and experience in the materials science field, this thesis would not have been possible. I would also like to thank him for encouraging me to participate in the Undergraduate Materials Research Initiative sponsored by the Materials Research Society in which I was awarded an honorable mention for an initial proposal of my research.

I would also like to thank Dr. Langner for letting me use his lab equipment and for spending many hours teaching me how to use DSC and DMA.

Also, both Dr. Langner and Dr. Ghoneim deserve a huge thank you for taking time out of their busy schedules to serve on my thesis committee.

Table of Contents

Index of Figures

List of Tables

List of Terms & Symbols

A	Instantaneous Area of the Specimen
A_0	Original Area of the Specimen
A_f	Austenite Finish Temperature
AFM	Atomic Force Microscopy
A_s	Austenite Start Temperature
A_y	Area of the Specimen at Yield Point
D	Interplanar Spacing
δ	Change in Specimen Length
DMA	Dynamic Mechanical Analysis
DSC	Differential Scanning Calorimetry
E*	Complex Modulus
E, E'	Modulus of Elasticity (Young's Modulus)
E"	Imaginary Loss Modulus
ε_{ave}	Average Strain
ε_t	True Strain
KHN	Knoop Hardness Number
L	Instantaneous Length of the Specimen
L_0	Original Length of the Specimen
L_f	Final Length of the Specimen
L_y	Length of the Specimen at Yield Point
M_f	Martensite Finish Temperature
M_s	Martensite Start Temperature
ν	Poisson's Ratio
SE	Superelasticity
SMA	Shape Memory Alloy
SME	Shape Memory Effect
σ_{eng}	Engineering Tensile Stress
σ_{true}	True Tensile Stress
t	Instantaneous Thickness of the Specimen
t_0	Original Thickness of the Specimen
θ	Bragg Angle
w	Instantaneous width of the Specimen
w_0	Original width of the Specimen
XRD	X-ray Diffraction

Introduction

Shape Memory Alloys (SMA) are very interesting alloys that have become a part of everyday life for many people without them even knowing it. Shape memory alloys get their name because of their unique ability to "remember" their original shape even after the alloy is apparently plastically deformed. The shape that a SMA remembers is determined by the user, and it can be easily changed with proper heat treatment. Depending on the certain characteristics of the alloy, it can recover the deformation once it is heated above a certain temperature or, it will automatically return to its original shape once the stress is removed. *In the case of the material used in this study, the alloy remembers its original shape after it is heated above a certain temperature.* The first recorded incident of a material exhibiting shape memory characteristics was in 1951, and the material was an Au-Cd alloy. Later in 1963 at the Naval Ordinance Laboratory (NOL), the shape memory phenomenon was observed in an equiatomic NiTi alloy, and the alloy was given the acronym NiTi-NOL or Nitinol[1]. Since its discovery in 1963, NiTi has beeen used in many different applications such as pipe couplings, antennas, actuators, and they are also being used extensively in the medical and dental fields.

The shape memory phenomenon occurs because of a crystallographically reversible martensitic phase transformation. The transformation is diffusionless, where the atoms shift small distances from an ordered high temperature phase (austenite) to a lower energy phase (martensite). Another interesting characteristic of NiTi is superelasticity (SE). In SE, large stress induced deformations are recovered when the stress is removed and it doesn't require a change in temperature[2]. Just as in SME, a reversible martensite transformation occurs allowing the deformations to be recovered.

The shape memory phenomenon and superelasticity will be discussed at a greater length in the subsequent pages.

The goal of this research is to study the changes of various properties of shape memory NiTi when specimens are prestrained different amounts. The properties that will be investigated are hardness, transformation temperatures, modulus of elasticity, and microstructure. Different characterization techniques will be used to record the changes in these properties as the pre-strain amount is varied.

Shape Memory Effect

The mechanism behind SME is a shear-like deformation where a diffusionless phase transformation occurs. This transformation is a crystallographically reversible martensitic transformation. Figure 1 is a simple schematic showing the shape memory process from a microscopic point of view. Depending on the temperature, the SMA can either be austenite or martensite, the latter being the low energy (temperature) phase. Assuming the SMA is at a temperature below the martensite transformation finish temperature (M_f) temperature and undeformed, the SMA will be in the twinned martensite stage.

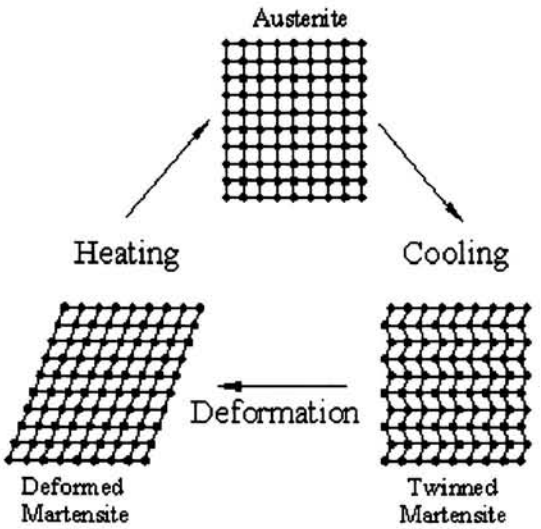

Figure 1 Shape Memory Process[1]

In twinned martensite, there may be many regions of martensite that have the same structure but are oriented differently, and these are called correspondence variants. When a stress is applied to the twinned martensite, it deforms by the movement of twin boundaries. As the stress is increased, the variants begin to orient themselves into a preferred orientation that permits the largest deformation.[3] In the case of a single crystal as in Figure 1, one single variant can be produced as shown by the deformed martensite stage. If the SMA is then heated, reverse transformation will take place and the martensite will transform into the parent austenite.[1-3] If the SMA is then cooled again, self-accommodating martensite will be formed, and the SMA will be in the same state as the beginning of the description of the shape memory process. If the unstrained self-accommodated martensite is heated, it will still revert to the parent austenite even though no deformation takes place. It is the reverse transformation from the deformed martensite to parent austenite that gives NiTi its shape memory.

Something not mentioned in the previous example is that these transformations start and end at certain temperatures. The transformation from parent austenite to martensite begins at the M_s temperature and is completed at the M_f temperature. The transformation from martensite to austenite begins at A_s and finishes at A_f. Figure 2 graphically portrays the phase that NiTi is in as it is heated and cooled. It is important to notice that when the temperature of NiTi falls between either M_s and M_f or A_s and A_f, both phases are present.

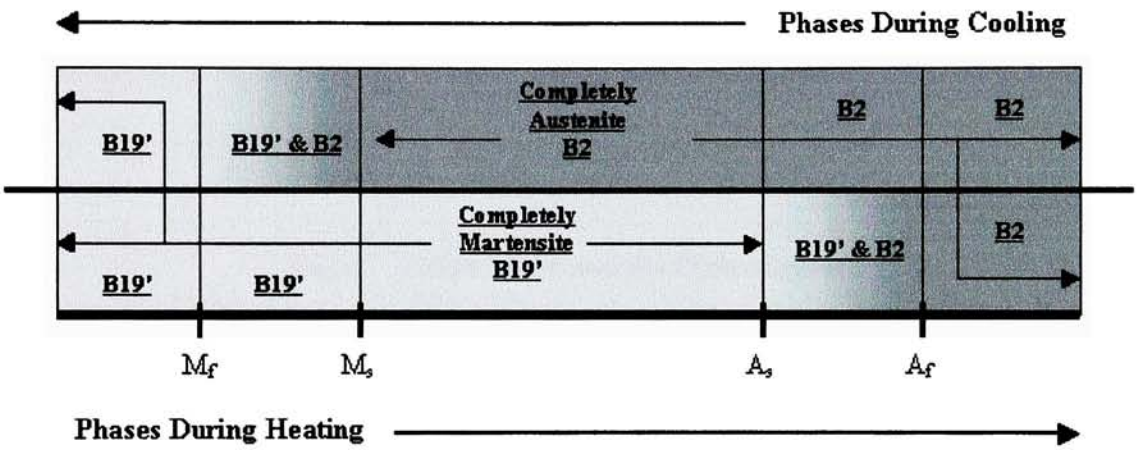

Figure 2 Diagram of phases as NiTi is heated and cooled

Another important thing to notice is that there is a hysteresis associated with the phase transformations. This means that the forward and reverse transformation temperatures are different. Typically NiTi has a 20 – 40°C hysteresis, but it is extremely alloy dependent.

Crystallography of the Shape Memory Effect

The shape memory effect occurs because a SMA undergoes a crystallographically reversible martensitic transformation. Depending on temperature, NiTi has several

different phases that it can be in. In its high-temperature form, NiTi is in its parent austinitic state which has a CsCl body centered cubic (BCC) crystal structure which is denoted by B2. The B2 CsCl crystal has side lengths where $a = b = c = 0.301 - 0.302$ nm and $\alpha = \beta = \gamma = 90°$.[3] See Figure 3 for the side and angle designations.

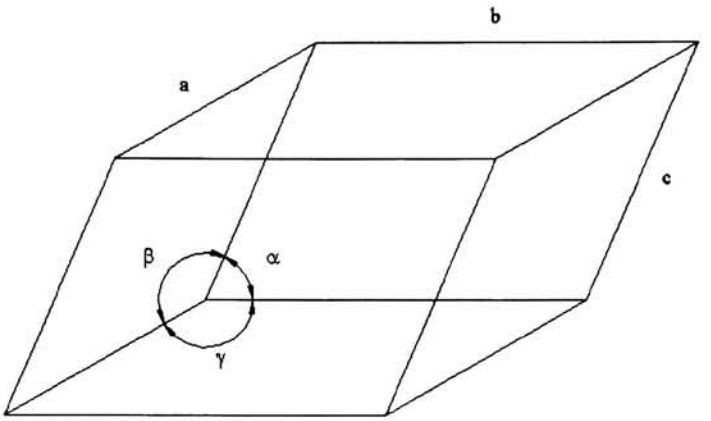

Figure 3 Lattice Parameters of a Crystal System[4]

In its low temperature state, NiTi is in a low energy martensitic phase which has a monoclinic structure which is denoted by B19' with lattice parameters $a \neq b \neq c$, and $\alpha = \gamma = 90° \neq \beta$. For a monoclinic crystal, the lattice parameters reported by Sinclair et al were, $a = 0.2885$ nm, $b = 0.4622$ nm, $c = 0.4120$ nm, and $\gamma = 96.8°$.[5]

As mentioned previously, the shape memory effect and superelasticity depend heavily on a martensitic transformation (MT). In MT, the atoms move cooperatively, often by a shear-like mechanism. The martensitic transformation begins from the ordered parent austenite phase and ends with the lower symmetry monoclinic phase. Previously it was mentioned that low temperature martensite may consist of many regions with the same structure but different orientations known as correspondence variants. These variants arise because the low temperature phase has a lower symmetry than the cubic

parent phase. It has also been proven that MT is a linear transformation. To see this, one can go through all the linear algebra behind MT[2], or one can take a single crystal SMA and scratch a straight line in the surface and allow it to cool. Upon cooling, the line will change direction and remain straight. Since a line and a surface become a different line and surface, it demonstrates that a shape change associated with MT is linear.

In terms of crystallography, each (110) plane of the parent phase deforms nearly to a hexagonal network and shifts in the $[1\,\bar{1}\,0]$ direction by a shear resulting in a stacking arrangement as shown in Figure 4.

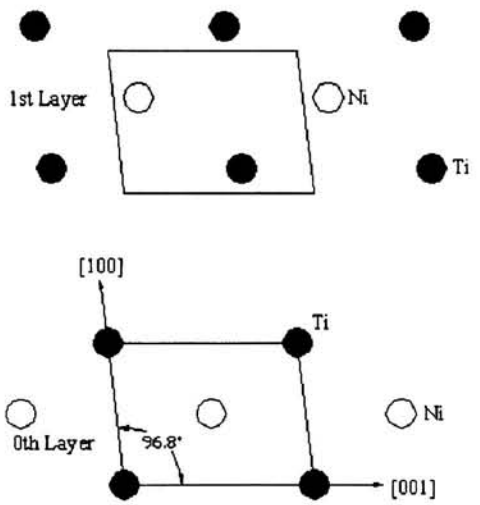

Figure 4 Crystal Strucure of B19' NiTi[6]

It was previously mentioned that during the phase transformation from the parent austenite phase to the martensite phase that self-accommodation occurs. Self-accommodation is the ability of the microstructure to change phases without changing shape. In a self-accommodating microstructure, there is a coherent arrangement of martensite variants occupying a region whose boundary suffers no displacement with respect to the parent austenite[7]. Self-accommodation is important to shape memory

materials because it aids in making the transformation to martensite reversible or thermoelastic.

Since most shape memory materials in use are polycrystalline, self-accommodation greatly facilitates the reversibility of phase transformations. In a polycrystalline SMA there are a large number of randomly oriented grains. Since these grains are all randomly oriented, any change in shape would develop internal stresses or possibly cracks because of the mismatch of the grain boundaries. Since internal stresses would oppose the reversibility of the phase transformation, the material accommodates these differences which is known as "self-accommodation". Because of the accommodation phenomenon, it would be possible to put a self-accommodating microstructure within austenite without introducing macroscopic stresses. Similarly, for the same reason, martensite can nucleate within austenite during cooling in a stress-free manner, which eases the transition from austenite to martensite.

A key part of self-accommodation that allows the material to change shape is "twinning." Generally, there are only two mechanisms by which a material deforms: slip and twinning. Slip is a permanent process and is common in many martensites. Obviously since slip is a permanent phenomenon whereas the shape memory effect is reversible, it is clear that NiTi undergoes twinning to accommodate the new structure upon transformation. Twin boundaries are planes across which there is a mirror image misorientation of the lattice structure[4]. A schematic of a twin boundary can be seen in Figure 5. Atoms that are along the twin boundary see the same number and types of bonds in both directions.

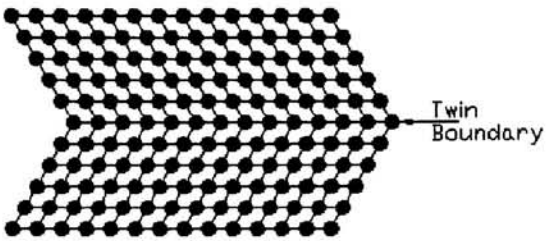

Figure 5 Example of a Twin Boundary

Twin Boundaries are capable of interfering with the slip process and increase the strength of the material. Another key property of twin boundary is that they are of a very low activation energy and are quite mobile. The energy is low because the atoms that are along the boundary are bonded very similarly to those that are not along the boundary. This bonding causes the boundaries to be very mobile. In most materials, the movement of twin boundaries can cause the material to deform, but in SMA, twinning allows the material to change phases without changing the volume or causing any internal stresses. One of the reasons that NiTi does not undergo slip to accommodate martensite is because slip requires atomic bonds to be broken, and twinning allows all atomic bonds to remain intact.

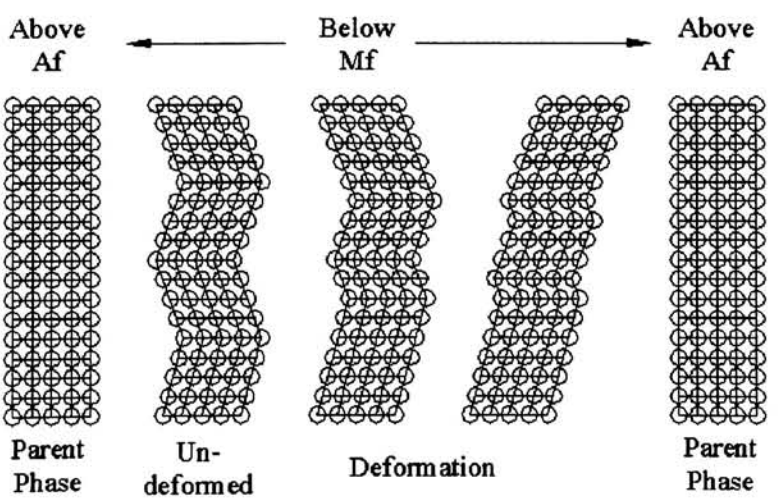

Figure 6 Twinning during heating and cooling[2]

Figure 6 shows a microscopic explanation of twinning through a heating-cooling-heating cycle. From the left, the material starts in the ordered parent state then is cooled and self-accommodated martensite is formed. Upon deformation, the twin boundaries easily move and convert to a different orientation that better accommodates the stress. When the material is then heated above A_f, it returns to the ordered parent austenite phase. Figure 7 demonstrates this phenomenon in Cu-Al-Ni. As one can see from this figure, the twin boundaries move and convert to a different preferred orientation according to the applied stress. This process of condensing many twin variants into a single favored variant is called detwinning.[1]

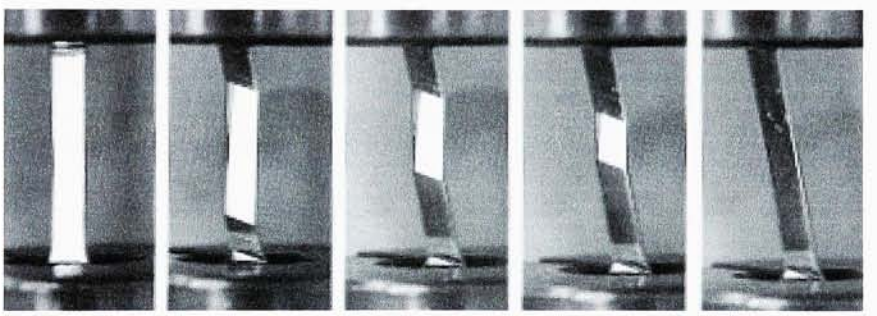

Figure 7 Example of self-accommodation[2]

The occurrence of self-accommodating martensite and deformation twinning in SMA leads to interesting mechanical properties.

Mechanical Properties of NiTi

Before studying the mechanics of a material, there are a few concepts that must be introduced. The first concept is strain. There are two types that are used, engineering

strain and true strain. Engineering strain is defined as the ratio of the change in length to the original length.

$$\varepsilon_{ave} = \frac{\delta}{L_0} = \frac{L - L_0}{L_0} \quad (1)$$

True strain, which is the instantaneous change in linear dimension divided by the instantaneous value of the dimension, is extremely useful when dealing with plastic deformation[8].

$$\varepsilon_t = \int_{L_0}^{L_f} \frac{dL}{L} = \ln \frac{L_f}{L_0} \quad (2)$$

Another concept that is key to studying mechanics is stress. Again there are two types, engineering stress and true stress. Engineering stress is the load divided by the cross-sectional area of the unloaded material. True stress is the load divided by the instantaneous cross-sectional area.

$$\sigma_{eng} = \frac{P}{A_0} \quad (3)$$

$$\sigma_{true} = \frac{P}{A} \quad (4)$$

Given the previous definitions, the tensile properties of a material can be studied. When an axial tensile load is applied to a metal, the metal goes through several stages of deformation. During the first stage of deformation, the specimen exhibits elastic behavior. This means that the specimen will recover its original dimensions when the load is removed. This recovery should not be confused with the shape recovery process or superelasticity of NiTi. Elastic recovery in most metals occurs at fractions of a percent strain, while superelastic NiTi is capable of recovering up to approximately 8% strain upon unloading.[9,10]

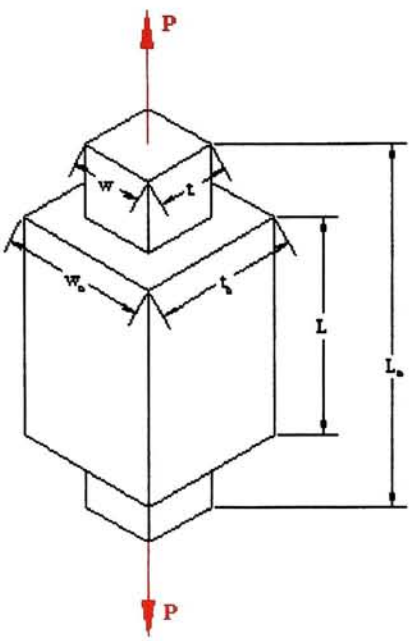

Figure 8 Specimen in Tension

When most materials are deformed elastically, the resulting stress is proportional to the strain and is governed by Hooke's Law.

$$\sigma = E\,\varepsilon \tag{5}$$

Also in the elastic region, the contraction in the y and z-directions (Figure 8) is directly proportional to the elongation in the x-directions.

$$\varepsilon_x = -\nu\varepsilon_y = -\nu\varepsilon_z \tag{6}$$

Using the previous equation, expressions for the instantaneous length, width, and thickness can be developed.

$$L = L_0\left(1+\varepsilon_x\right) \tag{7}$$

$$w = w_0\left(1-\nu\varepsilon_x\right) \tag{8}$$

$$t = t_0\left(1-\nu\varepsilon_x\right) \tag{9}$$

Since an engineering stress-strain curve does not completely depict the deformation characteristics of a material, it is imperative to calculate the true strain and

true stress from equations (2) and (4). For true stress the instantaneous area is needed, and it is found by multiplying the instantaneous width and thickness.

$$A = w_0 t_0 (1 - \nu \varepsilon_x)^2 \qquad (10)$$

Using this equation, the final equation for true stress is,

$$\sigma_{true} = \frac{\sigma_{eng}}{(1 - \nu \varepsilon_x)^2} \qquad (11)$$

This elastic behavior continues until the load reaches the elastic limit. When the elastic limit is exceeded, the second stage is encountered where yielding occurs, which means the material will not return to its original dimensions when the load is completely removed. This is called plastic deformation. In this stage of deformation, the material deforms uniformly. Although the deformation is uniform, the strain is no longer directly proportional to the stress, so equation 10 no longer correctly describes the instantaneous area. A better representation of the area comes from the assumption that the volume of the specimen remains constant after yielding occurs. This assumption allows an expression for instantaneous area to be written,

$$V_y = V = \text{Constant}$$
$$L_y A_y = L A$$

where V_y, L_y, and A_y are the volume, length and area at the elastic limit. Solving for instantaneous area (A),

$$A = A_y \frac{L_y}{L} \qquad (12)$$

With a new expression for area, the new equation for true stress in the uniform plastic region is,

$$\sigma_{true} = \frac{PL}{A_y L_y} \quad (13)$$

Once the material reaches its ultimate strength, the deformation becomes unstable and necking occurs, and this is the third stage of deformation. Necking is a localized deformation where the increase in stress is due to a decrease in the cross-sectional area, and the deformation is no longer uniform. In this study, the specimens never entered the necking region so this stage will not be discussed at length.

In NiTi, the stress-strain diagram looks quite a bit different than a standard stress-strain curve that one would see for a typical ductile material. Martensitic NiTi exhibits the stress-strain characteristics that are shown in Figure 9. As one can see, the material appears to initially deform like a standard ductile material, until point A. According to Liu et al, this deformation is due to the elastic accommodation of twin bands.[11]

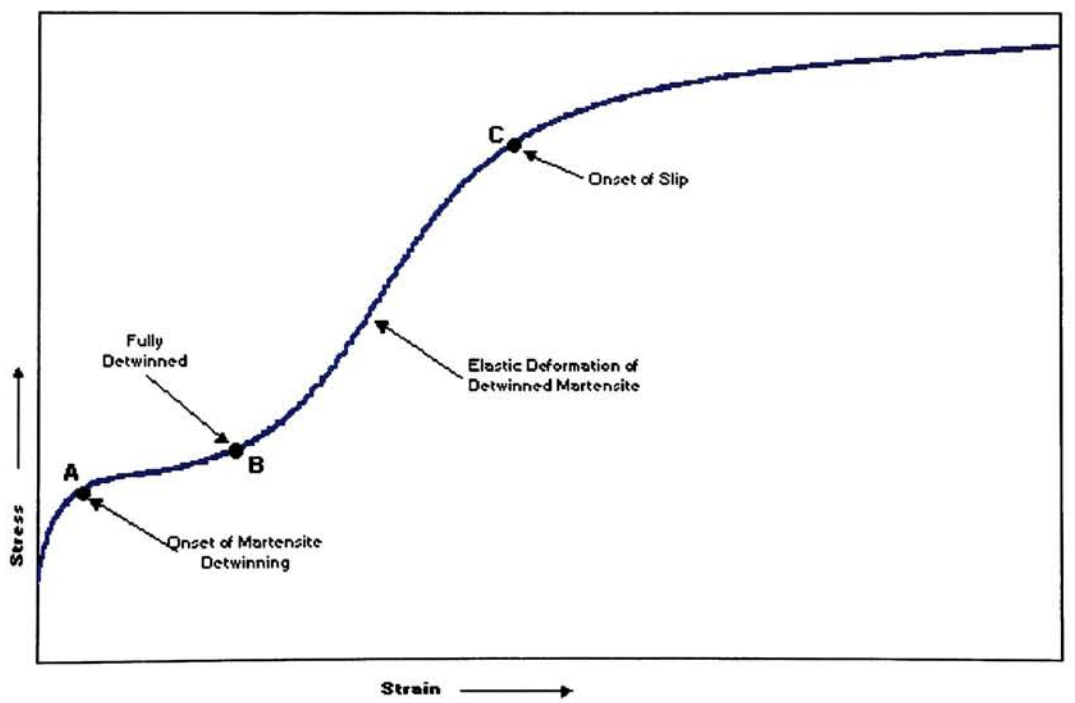

Figure 9 Stress-Strain Curve for NiTi[1]

At point A, the twinned martensite undergoes martensite variant reorientation[11,12] until the martensite is fully detwinned (point B). After the martensite has become fully detwinned, it exhibits a secondary elastic deformation. During this stage, it is the detwinned martensite that deforms elastically[1]. At point C, slip begins and the deformation is no longer completely reversible upon unloading or when heated above A_f. Point C falls at about eight percent for the material used in this study which is consistent with the generally accepted value for maximum recoverable strain in NiTi.

Other Characteristics of NiTi

NiTi also has several other important characteristics that are not explored in this research. One of these characteristics is called superelasticity (SE). Superelasticity occurs when a material recovers from large deformations upon the removal of the stress. Essentially SE is the same as shape memory effect, but no heating is required to recover the original shape. In NiTi SE occurs when the material is in its parent austenitic state. The parent state can be achieved by heating above the A_f, or it can occur at temperatures below room temperature depending on the atomic composition. SE occurs because of stress induced martensite which reverts back into the parent austenite phase when the stress is removed. Essentially, the stress acts the same as temperature does for SME, where a decrease in temperature is equivalent to an increase in stress.[1] As with SME, one preferred martensite variant will form as the material is deformed.

Another interesting characteristic of SMA is what is known as two-way memory effect. As one might guess from the name, a two-way SMA is capable of remembering two different shapes. The shapes that are remembered are the parent austenite shape, as in standard one-way memory, and the other is the deformed martensite shape. When the alloy is above A_f, it takes the shape of the parent austenite, then when it is cooled below M_f, it takes the shape of the deformed martensite. Special thermomechanical treatments are required to produce this effect. This training introduces microstresses that tend to bias the nucleation and growth of martensite, and these microstresses cause the material to transform from parent austenite directly into deformed martensite.[1]

The last characteristic that will be mentioned in this section is the intermediate phase that occurs in some compositions of NiTi, but it will not be discussed at great

lengths because this phase did not occur in the alloy studied. This intermediate phase is called the R-phase because it has a rhombohedral crystal structure. To determine if the R-phase occurs during the cooling of NiTi, a DSC cooling scan could be taken where the alloy is cooled from above A_f to below M_f. If two exothermic peaks appear on the scan, there is evidence that the R-phase has occurred. The R-phase produces a much smaller peak than the martensitic transformation, and it occurs at a higher temperature. The typical hysteresis of the R-phase is only a couple of degrees Celsius. As noted before, the material used in this research does not transition through the R-Phase because there is no additional peak evident on the DSC cooling curve. Also, the R-Phase is usually not evident in Titanium rich NiTi alloys.

Experimental Plan

Materials

The material used for this research was alloy BH from Memry Corporation in the form of 0.432mm x 11.379mm ribbon. According to Memry, the composition of the alloy was 54.5 wt % Ni and it was cold rolled. From the weight percentage, the atomic percentage of nickel was determined to be 49.4 at % Ni.

Specimen Preparation

Six samples were cut from the as received ribbon using a small shear. The samples were approximately 125mm long by 11mm wide. Since the ribbon received from Memry Corporation was in a cold-worked state, it was necessary to anneal all samples at 850°C for 30 minutes. Before the specimens were placed in the furnace, all grease and dirt was removed by wiping them with methanol. To minimize oxidation, the samples were placed between alumina plates and a steel weight was placed on top of the plates. Following the annealing treatment, the specimens were quenched in water at room temperature. A second heat treating process was needed to "teach" the specimens a shape and to give them the shape memory ability. At this step the samples were cleaned again with methanol and placed between the alumina plates. They were then placed in the furnace at 350°C for 30 minutes and allowed to air cool.

Once the specimens had air-cooled, they were prestrained using a Instron Universal testing machine while the strain was measured with an MTS extensometer. Figure 10 shows the configuration of the sample and extensometer in the testing machine. Prior to straining the specimens the width and thickness was measured and recorded. The

specimens were strained with a crosshead speed of 1.25 mm/min, and the strain was also released at 1.25 mm/min. Load and extension data were recorded using Testworks in English units and converted to SI units after the data was exported into an Excel spreadsheet. After each specimen received the proper strain amount, they were separated and labeled with MEM850XX, where the XX stands for the amount of prestrain the specimen received.

After the specimens had been prestrained, they were cut into sections for each experiment. Table 1 lists the required lengths for each experiment.

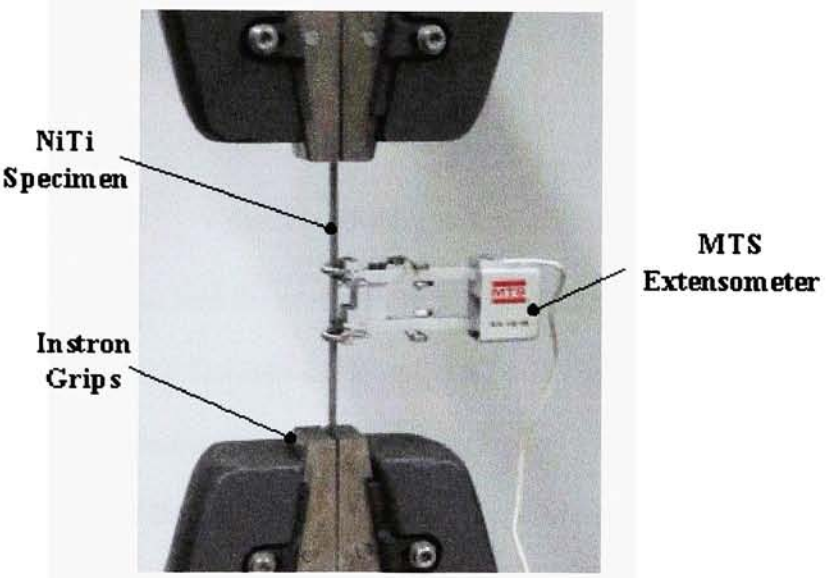

Figure 10 Tension Apparatus Setup

Table 1. Specimen Lengths

Experiment	Length of Specimen
Dynamic Mechanical Analysis	50 mm
X-Ray Diffraction	15 mm
Microhardness	13 mm
Optical Microscopy	13 mm
Differential Scanning Calorimetry	5 mm
Ends for Grips (Waste)	2 x 15mm

Samples for X-Ray Diffraction, hardness testing and optical microscopy had to be mechanically polished before analysis. To polish the samples, sample holders had to be fabricated. The holders consisted of a 32mm Bakelite disk with a 0.650mm deep groove milled in one of the flat surfaces (Figure 11). The other surface was use for sample identification.

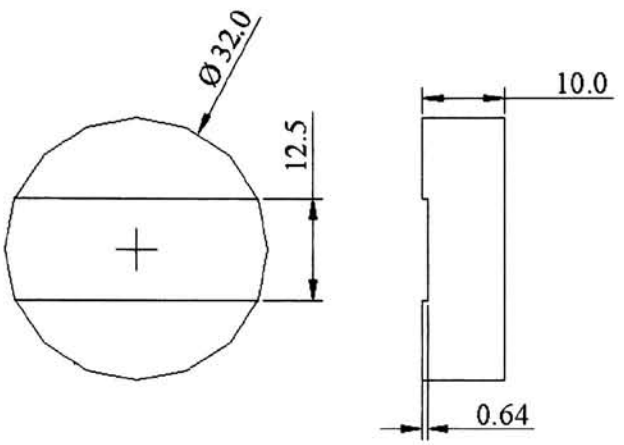

Figure 11 Polishing Disk Dimensions

Each specimen was glued into the groove with a drop of superglue. The mechanical polishing was done using a Rotopol-11, RotoForce1 and Multidoser all purchased from Struers. For microhardness testing and optical microscopy, the samples were left attached to the Bakelite disk, while the x-ray sample was removed with a drop of acetone and then mounted on a glass slide using double-sided clear tape. The DMA sample was wet sanded on #220 grit sandpaper to remove any oxide that resulted from the heat treatment process. An 8-10 mg sample was cut from each DSC 5mm piece using a shear and then they were placed into aluminum specimen pans.

Differential Scanning Calorimetry

Differential scanning calorimetry (DSC) is used to find thermochemical and thermophysical characteristics of a substance. The DSC measures heat flow into (endothermic) or out (exothermic) of a material as it is heated at a defined rate. If the material undergoes a phase transformation, there will be a change in the heat flow depending on the type of transformation. Since it is well known that SMA experience a phase change, DSC is an excellent choice for monitoring the heat flow of a specimen as it transforms into either austenite or martensite or even a different phase. Another reason that DSC is excellent for characterizing the transformation temperatures is that the sample remains unstressed throughout the entire experiment, and it has been shown that stress has a large effect on the transformation temperatures. [9,13] A typical chart of heat flow versus temperature can be found in Figure 12

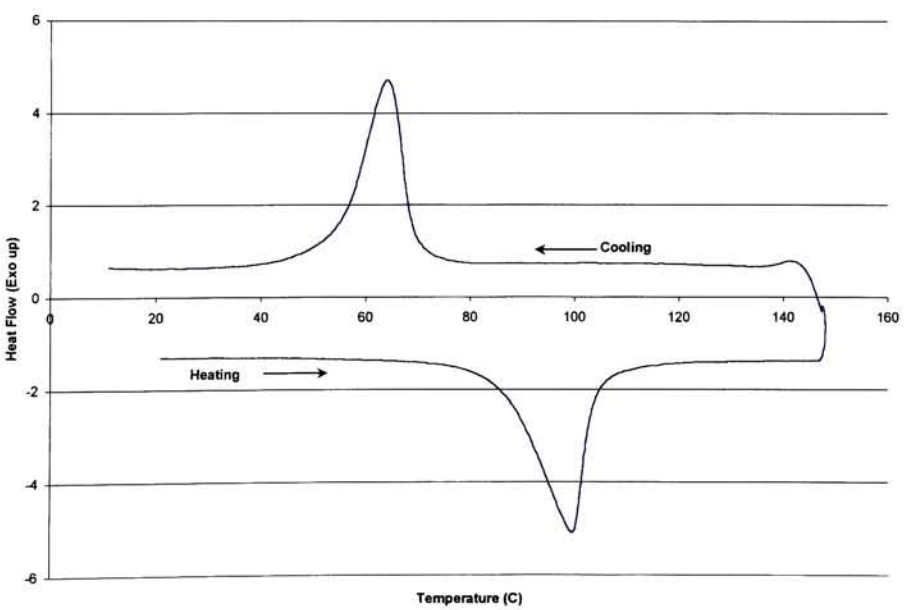

Figure 12 Typical DSC Scan of NiTi

From this scan it is important to notice that there is only one exothermic peak and one endothermic peak evident in the heating/cooling cycles. This proves that this alloy does not transform from austenite to the intermediate R-phase before transforming into martensite.

In this study, samples of 8-10 mg were cut from the prestrained specimens and analyzed in a TA Instruments DSC 2010 differential scanning calorimeter. After the specimens were cut, they were cleaned with methanol and sealed in aluminum specimen pans. Prior to starting the heating and cooling cycles, a specimen was placed inside the calorimeter as well as an empty specimen pan, which served as the reference material. For the first cycle, the initial transformation temperatures were estimated and the DSC was set to heat 30-50°C beyond those estimates and cool to 10°C at a rate of 10°C per minute. For the second and third cycles, the specimen was heated to 150° and cooled to 10°C at a rate of 10°C per minute. An example of the three heating/cooling cycles can be seen in Figure 13. All heating and cooling was done under a constant flow of nitrogen at 50 ml/min.

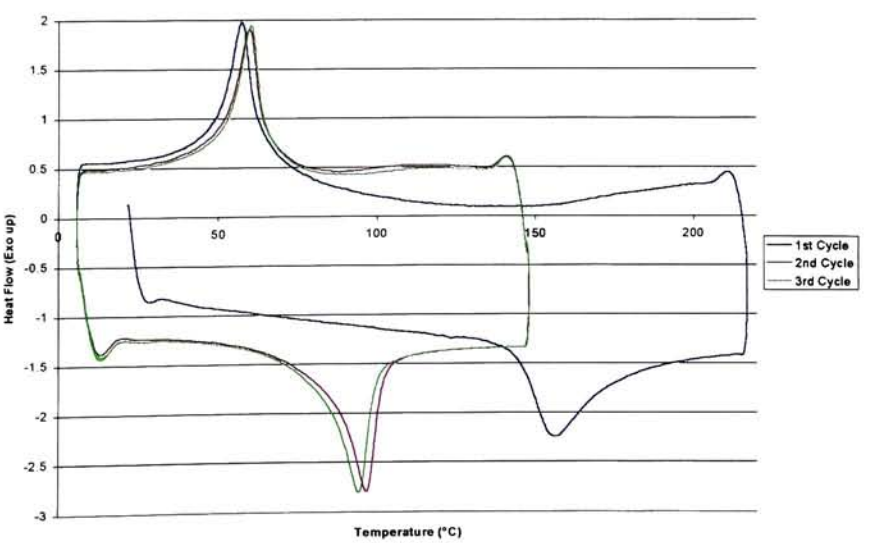

Figure 13 Three DSC Cycles

Dynamic Mechanical Analysis

Dynamic mechanical analysis (DMA) is a very useful tool for characterizing various materials. DMA is identified by various names such as, forced oscillatory measurements, dynamic mechanical thermal analysis (DMTA), dynamic thermomechanical analysis, and dynamic rheology. Lately, DMA has been used extensively on polymers to determine different properties such as glass transition temperatures, elasticity and resistance to creep. Glass transition temperatures could also be measured using differential scanning calorimetry (DSC), but in some materials the transition temperatures are too faint to be detected by DSC. DMA is much more sensitive so it is able to detect the slightest changes in material response.

The basic principle behind DMA is analyzing a material's response to an oscillating force. Based on a material's response to a sinusoidal stress, the stiffness (modulus) can be calculated from the sample recovery, and the tendency to flow (viscosity) is calculated from the phase lag. Transition temperatures can be found through drastic changes in the material's modulus. The stiffness describes the ability of the material to recover from a deformation, and the viscosity describes the ability of the material to lose energy in the form of heat (damping). DMA outputs a modulus which differs from the Young's modulus of elasticity. Young's Modulus, from Hooke's law, is defined as the ratio of stress to strain as shown in equation 14.[14]

$$E = \frac{\sigma}{\varepsilon} \qquad (14)$$

E can be determined by plotting several points in the linear region of stress-strain curve and finding the slope of the line through the points. As previously stated, DMA does not

measure Young's Modulus directly, it outputs a complex modulus denoted by E*. E* is defined as,

$$E^* = E' + iE'' \tag{15}$$

where E' is the elastic storage modulus which is a measure of the materials ability to store or return energy, and E" is the imaginary loss modulus which is the material's ability to lose energy. A good analogy of what E' and E" is best thought of as a ball bouncing as shown in Figure 14[15]. The height that is recovered after a bounce is E', the

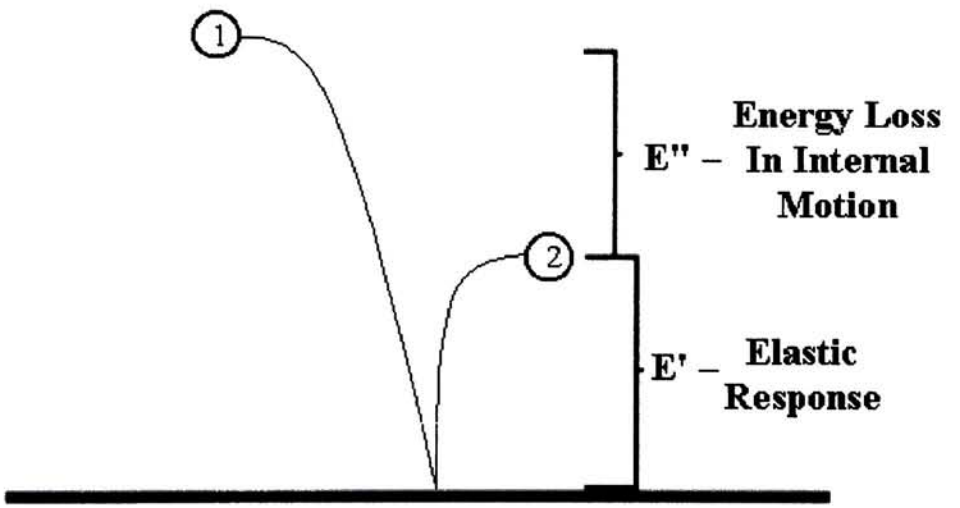

Figure 14 Elastic Response Analogy[15]

elastic response, and the difference between the original height and the second height represents E", the energy lost due to internal motion. An expression for E' is,

$$E' = \left(\frac{\sigma^0}{\varepsilon^0}\right)\cos\delta = \left(\frac{f_0}{bk}\right)\cos\delta \tag{16}$$

where f_0 is the force applied, b is the sample geometry term, k is the sample displacement at the peak and δ is the phase difference between the material and the applied stress. Since the modulus is dependent on stress that the sample sees, a different modulus will

result if a different sample is used and the forces are not adjusted to be the same. The imaginary (viscous) loss modulus is described by equation 17.

$$E'' = \left(\frac{\sigma^0}{\varepsilon^0}\right)\sin\delta = \left(\frac{f_0}{bk}\right)\sin\delta \qquad (17)$$

where b, k, and δ are the same as those used to calculate E'. Figure 15 gives a graphical representation of how k and δ are found from the response. Another important property that DMA measures is the tangent of the phase difference. This quantity is called damping and it represents how efficiently the material loses energy to internal friction and molecular rearrangements. Tan δ is defined as,

$$\tan\delta = \frac{E''}{E'} = \frac{\eta'}{\eta''} = \frac{\varepsilon''}{\varepsilon'} \qquad (18)$$

where η' is the energy loss portion of viscosity and η" is the storage portion, ε' is the in phase strain and ε" is the out of phase strain.

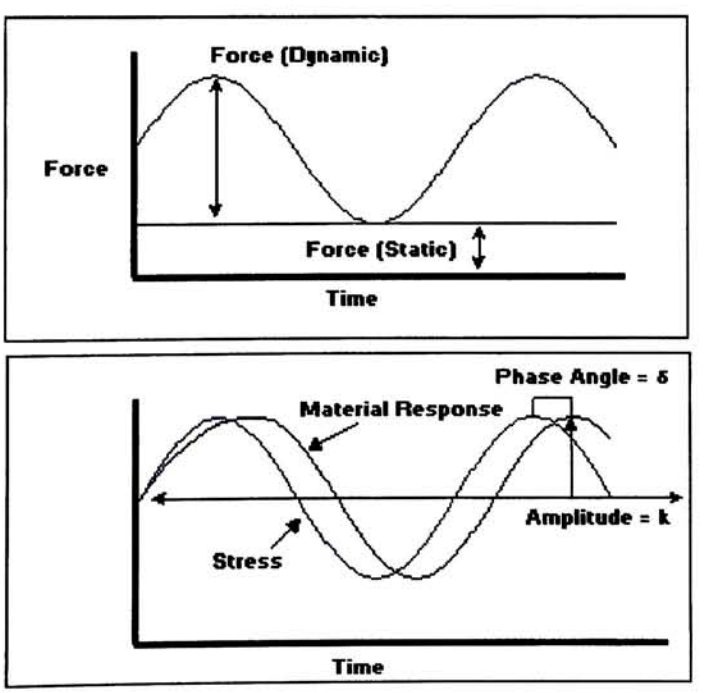

Figure 15 Dynamic Response of a Material

Since tan δ is the ratio of the loss to the storage modulus, it is independent of geometry and can also be used as a check for possible measurement errors in a test.[9]

To test a specimen dynamically, a Seiko Instruments DMS110 three-point bending machine was used.

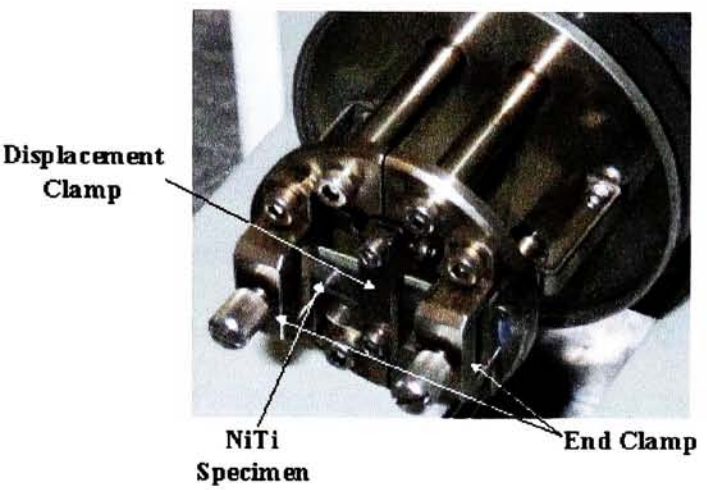

Figure 16 Three-point Bending Apparatus

Figure 16 gives a close-up view of the three-point bending fixture of the DMS110. The specimens were heated in 2 °C steps where the temperature was held constant for three minutes between steps. The temperature ranges used for heating varied between specimens because of the higher initial A_s and A_f temperatures. The heating rate was kept constant at 2 °C per step regardless of the temperature range used. The temperature ranges for the heating and cooling runs were estimated from the transition temperatures found from DSC curves. For the second and third trials, a general heating range from 70°C to 150°C was used since the transformation temperatures stabilized after the initial heating above A_f. After a heating run had completed, the specimen was then cooled from 130°C to 10°C at two-degree steps with a three minute hold time between

steps. There was no shift in the M_s and M_f temperatures during cooling so this range was used across all specimens. A constant flow of 300ml/min of Nitrogen was used during all heating and cooling cycles.

X-ray Diffraction

X-ray diffraction is an important characterization method for determining the structures of crystalline materials, and it is appropriately named because it uses diffracted x-rays to make these determinations. A diffracted x-ray is similar to reflected light, but there are some significant differences, for example, light reflects at any angle of incidence, while diffraction of x-rays takes place at certain angles only. Another difference is that the intensity of reflected light is almost the same as the incident light, but the intensity of diffracted x-rays is much less than the incident x-rays. The reason that there are only diffracted x-rays at certain angles is because there is constructive and destructive interference between diffracted x-rays. When a x-ray hits an atom, it is scattered in all directions, and when there are atoms arranged periodically, such as in a crystalline material, many of the scattered x-rays destructively interfere with each other, while others constructively interfere with one another. The constructive interference occurs because there are parallel beams that are integer multiples of x-ray wavelength out of phase with each other (essentially they are in phase), and the phase difference comes from the different distances the beams travel. It is the constructive interference that make x-ray diffraction possible.

To understand how x-ray diffraction works, consider a set of parallel planes spaced a distance d' apart, such as in a crystalline material (Figure 17). In the figure, a

beam with known wavelength (λ) is incident on the crystal at an angle θ. This angle is known as Bragg's angle and it is measured between the crystal planes and the beam. Considering beams 1 and 2, they strike atoms K and L and are scattered in all directions,

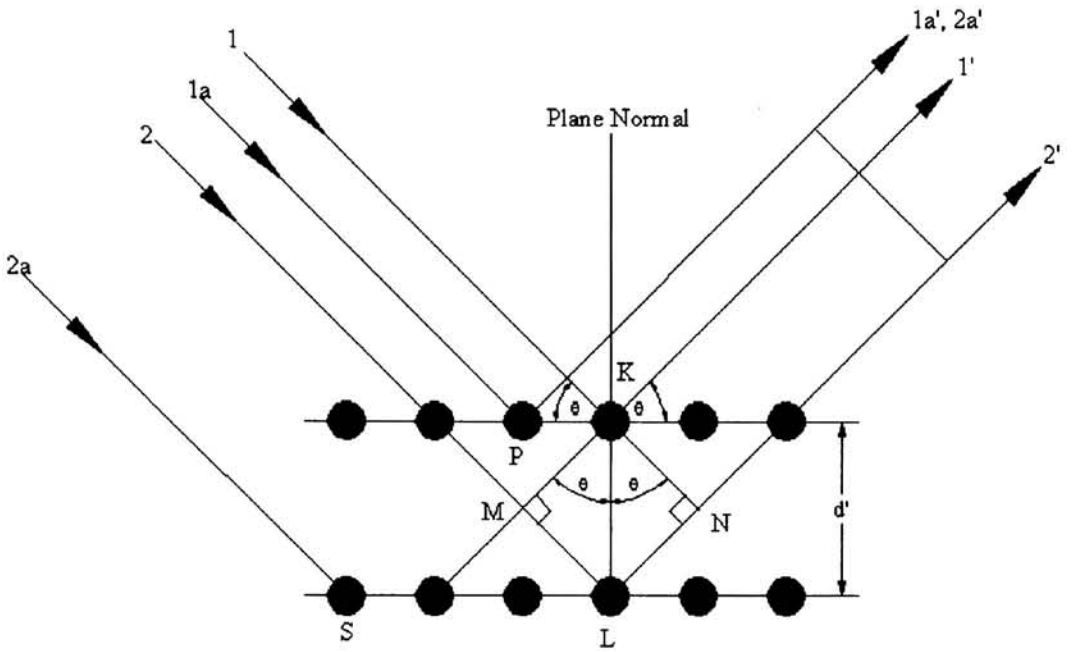

Figure 17 Diffraction of X-Rays by a crystal[16]

but only in the 1' and 2' directions will the scattered beams be in phase. The phase difference is related to the path difference, and it can be described by,

$$ML + LN = d'\sin\theta + d'\sin\theta$$

This is also the path difference for the rays scattered by S and P because there is no path difference between S and L or P and K. Since the rays 1' and 2' will be in phase, equation (19), which was first written by W.L. Bragg can be used.

$$n\lambda = 2d'\sin\theta \qquad \textbf{(19)}$$

This relation is known as Bragg's law. This expression is generally found in the form of Equation 20, where the substitution of d = d'/n is done for convenience.

$$\lambda = 2d\sin\theta \qquad \textbf{(20)}$$

From this expression we can see that the angle θ is a function of the spacing between planes as well as the wavelength of the x-rays. In the case of x-ray diffraction, the interplanar spacing d, is found by exposing a crystal to x-rays of known wavelength and measuring the angles at which diffraction occurs.

To measure the angles at which diffraction takes place, a diffractometer is used. A diffractometer consists of an x-ray source, a stage, and a counter. The x-ray source is a cathode ray tube which provides characteristic radiation, the stage is the area where the specimen is mounted, and the counter measures the intensity of the diffracted beams. The x-ray tube remains stationary at all times while the stage is rotated in place and the counter is rotated around the stage. Typically the angle between the incident beam and the diffracted beam is measured rather than θ. It is known that the angle between the incident and diffracted beam is 2θ.[16] The counter then measures the intensity of the diffracted beam. The final output of the diffractometer is a plot of diffracted beam intensity versus 2θ.

For this study, the crystallographic structure of the NiTi ribbon was determined through x-ray diffraction using a Rigaku DMAX-IIB diffractometer with Cu K_α radiation at 40kV and 35mA. 13mm specimens were cut from each strained sample and mechanically polished, and then mounted to a glass slide with double-sided tape. Scans began at 10 degrees and ended at 80 degrees with a scanning rate of 1.2 deg/min. The slit configuration defining the x-ray optics was set with a divergent slit of 1°, a scattering slit of 1°, a receiving slit of 0.15mm, and a nickel filter.

From the XRD scans, peaks were identified and the corresponding d-spacings were calculated. From these peaks, the lattice parameters for a B19' monoclinic unit cell

were calculated using linear regression as well as Excel's solver. To solve for these parameters, the equation for the plane spacings of a monoclinic cell had to be used.[16]

$$\frac{1}{d^2} = \frac{1}{\sin^2\beta}\left(\frac{h^2}{a^2} + \frac{k^2\sin^2\beta}{b^2} + \frac{l^2}{c^2} - \frac{2hl\cos\beta}{ac}\right) \quad (21)$$

In order to use Equation 21 with the known parameters from pdf 35-1281, it had to be rearranged replacing the angle β with γ, and the resulting formula was,

$$\frac{1}{d^2} = \frac{1}{\sin^2\gamma}\left(\frac{h^2}{a^2} + \frac{k^2}{b^2} + \frac{l^2\sin^2\beta}{c^2} - \frac{2hk\cos\gamma}{ab}\right) \quad (22)$$

Hardness Testing

The Knoop hardness test was developed in 1939, and it uses a precisely shaped diamond indenter and various loads to determine hardness characteristics of materials that cannot be tested by conventional techniques. The indenter, as shown in Figure 18, produces a rhombic-shaped indentation (Figure 19) where the ratio between long and short diagonals is approximately 7 to 1 while the depth of the indentation is approximately 1/30 of the length of the long diagonal. A Knoop indenter was chosen because it is less sensitive to measurement errors.

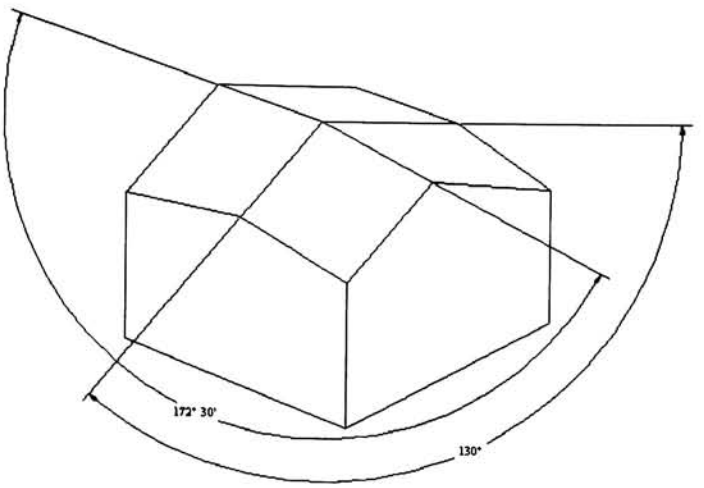

Figure 18 Knoop Indentor

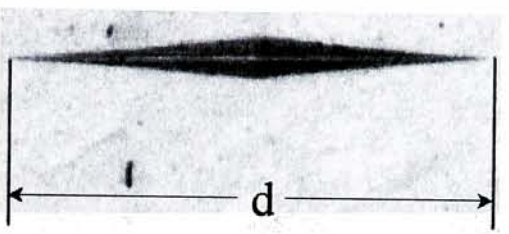

Figure 19 Knoop Indentation in NiTi Surface

The Knoop hardness number (KHN) is the ratio of the load applied to the unrecovered projected area.

$$KHN = \frac{P}{Cl^2} \tag{23}$$

In the previous equation, P is the load applied in kg, l is the length of the long diagonal in mm and C is the indenter constant relating the projected area of the indentation to the square of the length of the long diagonal. Since the long diagonal is typically measured in μm and the load applied is in grams, a more convenient equation for calculating the KHN can be written.

$$KHN = \frac{14229P_1}{d_1^2} \tag{24}$$

where P_1 is the load in gf and d_1 is the length of the long diagonal in μm.

Hardness testing is a very valuable tool because it relates the hardness number to other properties of a material. It is a measure of the resistance of the material to plastic deformation. In the hardness test, the indenter is pressed into the surface and the material deforms plastically leaving an indentation, which is then measured. As a result of the plastic deformation the material work-hardens.[17] Since there is work-hardening as well as plastic deformation occurring during a hardness test it is evident that the hardness number is related to the yield stress of the material as well as the strain hardening coefficient. Also, the hardness number is related to the modulus of elasticity of the material because there is some elastic spring back of the material when the indenter is withdrawn. This elastic spring back makes determining hardness values for some SMA very difficult. Depending on the temperature at which the test is conducted at, the SMA could recover some of the indentation if not all of it, which would give erroneous values. For this research, the NiTi was known to be in the martensitic phase during testing based on DSC scans.

The hardness testing for this research was done in accordance with ASTM standard E384.[18] All hardness testing was performed on a Mitutoyo MVK-H1 hardness testing machine at room temperature. A Knoop Indenter with a 100 gram load was used for all indentations. The duration of the indentation was 12 seconds. After the indentation was made, the indent was brought into focus at 40X magnification.

Prior to measuring the length of the long diagonal, the indentation was checked for symmetry. An indent was considered symmetric if there was less than a 20% difference between the two legs of the long diagonal. If the indent was not symmetric,

the specimen was adjusted to make sure that the surface was perpendicular to the indenter and another indent was made and checked. The long diagonal was measured by placing the inside edge of the ocular lines just into contact with the edges of the long diagonal. The hardness tester converted the length of the indent into the Knoop hardness number using equation 23. Three separate hardness values were taken for each indentation. Indentations were made until the KHN were within ±10, and at least 5 indentations were made per sample.

Optical Microscopy

Optical microscopy is a valuable tool that metallurgists use to identify surface characteristics of a material. In this research, brightfield images of the NiTi surface were taken. Brightfield images use normal lighting where the image is reflected vertically from the surface through the lenses. Images were then extracted using a video capture system with a gray scale camera. Prior to viewing the specimens under the microscope, the NiTi samples were mechanically polished to a 0.04 μm finish. No etching was performed.

Atomic Force Microscopy

Atomic Force Microscopy is an imaging technique developed in 1986. AFM uses an extremely small sharp tip that is affixed or integrated into a cantilever. The radius of the tip greatly effects the resolution of the scanned surface so for the best resolution, ideally a single atom tip should be used. The tip used in this research had a radius of less than 10nm. Depending on the mode that the AFM set to, either the tip is dragged across the surface of the test piece, or the tip taps the surface. The method used for this research was tapping mode where the tip lightly taps the surface. The tapping mode is advantageous because the tip does not remain in contact with the surface so there is less damage to the sample and the tip.

In tapping mode, the cantilever is oscillated at its natural frequency by a piezoelectric crystal and it is moved towards the surface until it begins to tap the surface. When the tip contacts the surface, the energy of the oscillating cantilever is dissipated and the amplitude of the cantilever is reduced. To keep a constant oscillation, the surface to tip distance is adjusted. The change in oscillation amplitude is what is used to identify and measure surface features. The amplitude is measured by laser beam deflection. A laser is focused on the backside of the cantilever and the beam reflects and strikes a photodetector. This method of measurement allows sub-angstrom measurements.[19,20]

AFM was performed using a Digital Instruments Dimension 3000 atomic force microscope in tapping mode. A scan size of 15μm was taken at a rate of 0.6 Hz in ambient conditions. Prior to scanning the NiTi strip was mechanically polished to a 0.04 μm finish and cleaned with alcohol. The areas of interest on the NiTi surface were surrounded by microhardness indentations to facilitate in locating these areas.

Data/Processing Method

Determination of Modulus of Elasticity

According to Hooke's law (5), the modulus of elasticity is the proportionality constant between stress and strain in the elastic region of deformation, therefore, an easy way to calculate the modulus is to find the slope of the linear elastic region. To do this one can perform a tensile test on a specimen and calculate the stresses and strains within the linear elastic range and fit a straight line to this region, where the slope of the line is the modulus of elasticity. Also, it has been found that if a material is loaded into the plastic region and then unloaded, the stress decreases in a linear fashion and it is parallel to the linear elastic region.[14] Since both regions are linear and the modulus of elasticity is the first derivative of the fitted line, an alternative for finding the modulus is to use numerical methods to find the first derivative of the data points.

One drawback to numerically differentiating experimental data is that the data contains noise that is characteristic of the equipment used during the experiment. Because of this noise, it is difficult to directly apply the standard formulas for forward, central, and backward difference. Alternatively, there have been several methods generated to numerically differentiate experimental data using FORTRAN programs.[21,22]. These methods also apply smoothing techniques to minimize errors. The FORTRAN program used for this research can be found in Appendix C.

The numerical differentiation method chosen is known as the Anderssen-Bloomfield-Cullum method[21]. To implement this method, the observed data must first be arranged into a function, (x_i, f_i), $i = 1 \ldots N$. Next the function is transformed so that it is zero at x_1 and x_N. After the transformation, the Fourier coefficients are calculated using

Goertzel's method combined with Reinsch's modifications[21]. Then the value of α that minimizes the function L(α) is calculated. The function L(α) is:

$$L(\alpha) = (N-1)\ln\left(\sum_{j=1}^{N-1} \bar{\gamma}_j^2 \left(1-\overline{w}_j\right)\right) - \sum_{j=1}^{N-1} \ln\left(1-\overline{w}_j\right)$$

where $\bar{\gamma}_j$ denotes the finite Fourier coefficients, and $\overline{w}_j$ the value of w_j with $\phi = \pi/(N-1)$. Finally the derivative values are found from the following equation:

$$f(t) = \sum_{j=1}^{\infty} \gamma_j w_j \phi_j^n \sin\left(\phi_j t + \frac{n\pi}{2}\right)$$

where,

$$w_j^{-1} = 1 + \alpha\phi_j^{2n} \sum_{k=0}^{m} \phi_j^{2k}$$

To find the first derivative of the elastic region stress and strain values for 0 to 0.1% strain were considered. For the unloading region, the strains from the maximum strain to 0.2% below that strain were considered. Also, the first three points of the unloading curve were neglected to remove any Hertzian effects. Theoretically the resulting derivative should be constant across all strains since the region is linear, but due to noise the value fluctuates so the average of range will be reported along with the maximum, minimum, and standard deviation of the derivatives.

Determination of Transformation Temps

Differential Scanning Calorimetry

Previously it was mentioned that there are definite temperatures at which the forward and reverse transformations occur. To characterize these temperatures, one could use a number of different techniques. The only drawback is that the results vary

slightly between every experiment, and both DSC and DMA, which were used in this study are no exception.

To characterize the transformation temperatures using DSC, a method similar to the ASTM standard, ASTM E1356-91, was used for determining the glass transition temperatures of polymers.[23] The first step taken was to take the raw data from DSC and separate heating cycles and the cooling cycles and plot the heat flow as a function of temperature. The austenite transformation temperatures are then determined from the heating cycle and the martensitic transformation temperatures are determined from the cooling cycles. The transformation temperatures are then found based on the location of the exothermic or endothermic peaks.

To determine the A_s transformation temperature, the baseline of the left side of the endothermic peak of the temperature vs. heat flow curve is extrapolated, and a line is drawn through the maximum gradient of left side of the peak. The intersection of the two lines is the transformation temperature.[2,13] This same method is then applied to the other side of the endothermic peak to determine A_f. The same steps are applied to the exothermic peak to determine the martensitic transformation temperatures. The only difference is that the right side of the exothermic peak corresponds to M_s and the left side to M_f. An example of this procedure can be found in Figure 20.

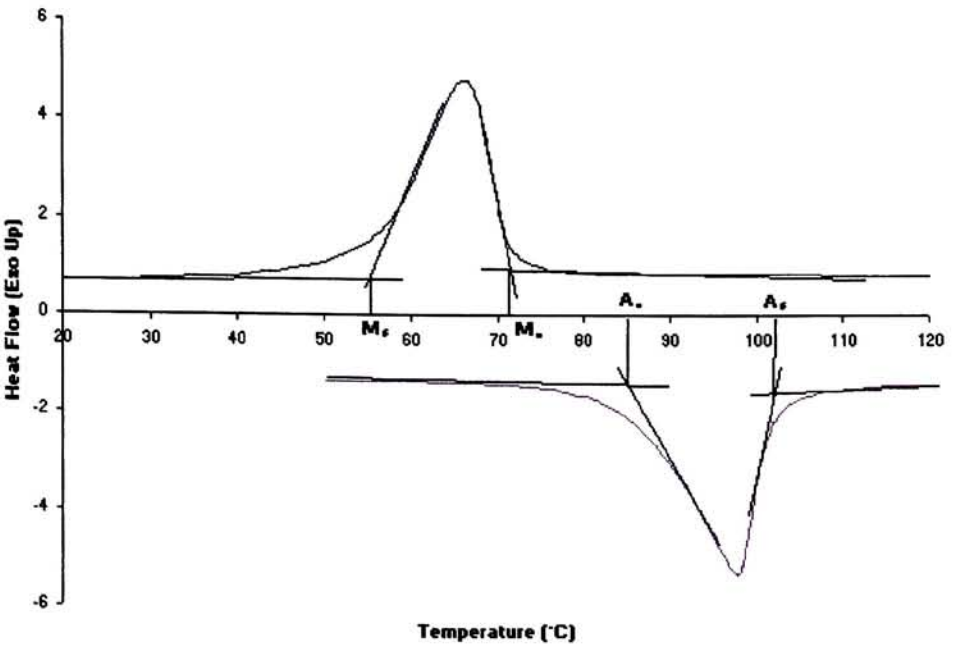

Figure 20 Determination of Transformation Temperatures from DSC

Since there were three separate heating and cooling cycles, the transformation temperature that was reported was the average of the three cycles for both martensitic transformations. Since it was found that the initial A_s and A_f temperatures were higher than the next two, the average of the second and third temperatures as well as the initial A_s and A_f temperatures were reported.

Dynamic Mechanical Analysis

DMA is a characterization technique like DSC that is generally used for characterizing polymers. Using DMA, the glass transition temperature of a polymer is found by a large decrease in stiffness as the temperature is increased. To find the exact temperatures, a method similar to that used to find the glass transition temperature of a polymer was used.[24,25] The major difference between a polymer and NiTi is that the stiffness increases for NiTi as the temperature is increased. First, the raw data was sorted

by frequency and then into heating and cooling cycles. Plots were then created of the stiffness as a function of temperature. Similar to DSC, the baseline is extrapolated and a line is drawn through the inflection point, and the intersection is the transformation temperature. The heating curves were generally smooth sigmoidal curves, which have only one inflection point, so both baselines intersected the same line. The cooling curves were different in that there was a dip in the stiffness before it stabilized into the baseline.

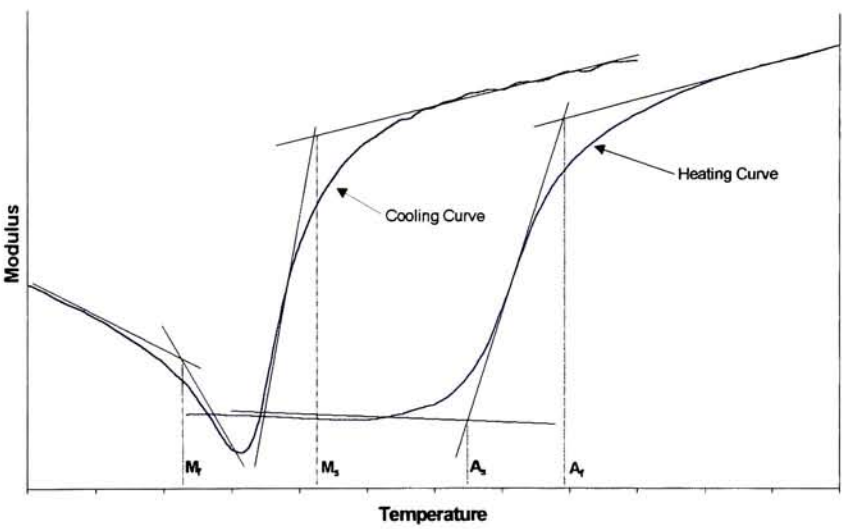

Figure 21 Determination of Transformation Temperatures from DMA

This dip increased the number of inflection points so the method applied to the cooling curves was slightly different. An example of this method can be found in Figure 21.

Again, similar to DSC, it was found that the initial A_s and A_f temperatures were found to be higher than the subsequent values so the average of the second and third temperatures were averaged and the initial A_s and A_f temperatures were recorded. The martensitic temperatures were all similar so the reported transformation temperature was

the average of the temperatures found from each frequency in each of the three cooling cycles.

Hardness

For each specimen, the Knoop hardness number was found through microhardness indentations. At least five indentations were made for each specimen, and more were made until there were five indentations within ± 10 KHN. For each separate indentation, the long diagonal length was measured three independent times. The hardness number for each indent was taken to be the average of the three measurements. The final hardness number for the sample was the average of the hardness number for each indentation.

Strain Hardening Exponent

Another important property that can be determined from tensile testing data is the strain hardening exponent. To find this value, the uniform plastic deformation region is fit with a power equation of the form,

$$\sigma_{true} = K \varepsilon_{true}^{\ n} \qquad (25)$$

This equation does not correctly describe the behavior of a ductile material once necking occurs. To find the onset of plastic deformation, the 0.2% yield stress was found using the slope of the secondary elastic deformation region. The first data point following the yield stress was normalized to be the zero point of the plastic region and the following stress and strain points were adjusted accordingly to the zero point. The data points were then plotted in Excel and a power curve was fitted using the trendline feature. To check the validity of the trendline feature, the slope and intercept of the log-log plot

were calculated using the least squares method. Taking the log of Equation 25, the following linear equation results,

$$\ln(\sigma_{true}) = \ln(K) + n\ln(\varepsilon_{true})$$
$$(y \quad = \quad b \quad + \quad mx \quad)$$

where the slope corresponds directly to the strain hardening coefficient and the intercept corresponds to ln (K).

Results/Discussion

Differential Scanning Calorimetry

Upon completion of all DSC experiments, the transformation temperatures were calculated using the procedure described above. The calculated transformation temperatures can be found in the following table.

Table 2 Transformation Temperatures from DSC in °C

MEM85000				
Run #	A_s	A_f	M_s	M_f
1	97.5	112.5	71.5	55
2	86.5	104	69.5	54
3	85.5	102	68	53.5

MEM85010				
Run #	A_s	A_f	M_s	M_f
1	129.5	*140*	69	45.5
2	80	105	67.5	47.5
3	78	102	66.5	47.5

MEM85003				
Run #	A_s	A_f	M_s	M_f
1	109	122	71	52
2	83	104	69.5	52
3	83	102	68.5	53

MEM85015				
Run #	A_s	A_f	M_s	M_f
1	140.5	155.5	64.5	50.5
2	89	103	66	51
3	86	101	66	51

MEM85005				
Run #	A_s	A_f	M_s	M_f
1	119	128	69	50.5
2	84	101.5	68	51.5
3	82.5	103.5	68	52

MEM85020				
Run #	A_s	A_f	M_s	M_f
1	144	172.5	63	49.5
2	85	102.5	66	52
3	83	100	66	53

After the transformation temperatures were recorded, it was noticed that each material had a much higher initial A_s and A_f temperature on the first heating cycle. Figure 22 shows this vast difference for the 20% strain sample. As one can see, the austenite transformation temperatures shift approximately 75 °C after the completion of the first cycle. Also, it is interesting to note that there is very little shift in the martensitic transformation temperatures, and this was consistent across all samples.

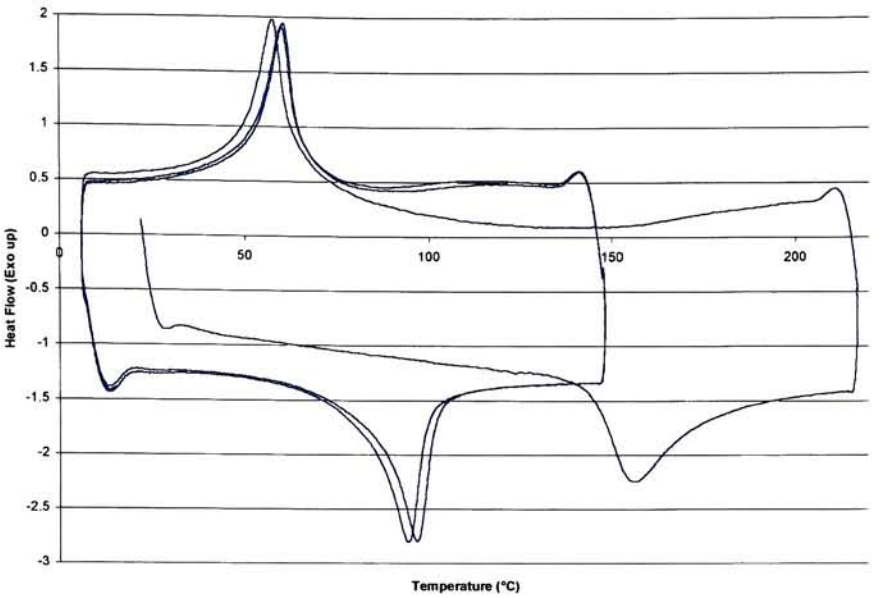

Figure 22 Example of Shift of A_s and A_f

The austenite transformation temperatures for the first heating cycle were found for each of the specimens and recorded in Table 3. These values for the initial A_s were plotted and there appeared to be a parabolic trend, so a second order trendline was fit to the data using Excel's trendline function. The fit of the curve to the data can be seen in Figure 23.

Table 3 Initial Austenitic Transformation Temperatures

Strain %	A_s (°C)	A_f (°C)
0	97.5	112.5
3	109.0	122.0
5	119.0	128.0
10	129.5	140.0
15	140.5	155.5
20	144.0	172.5

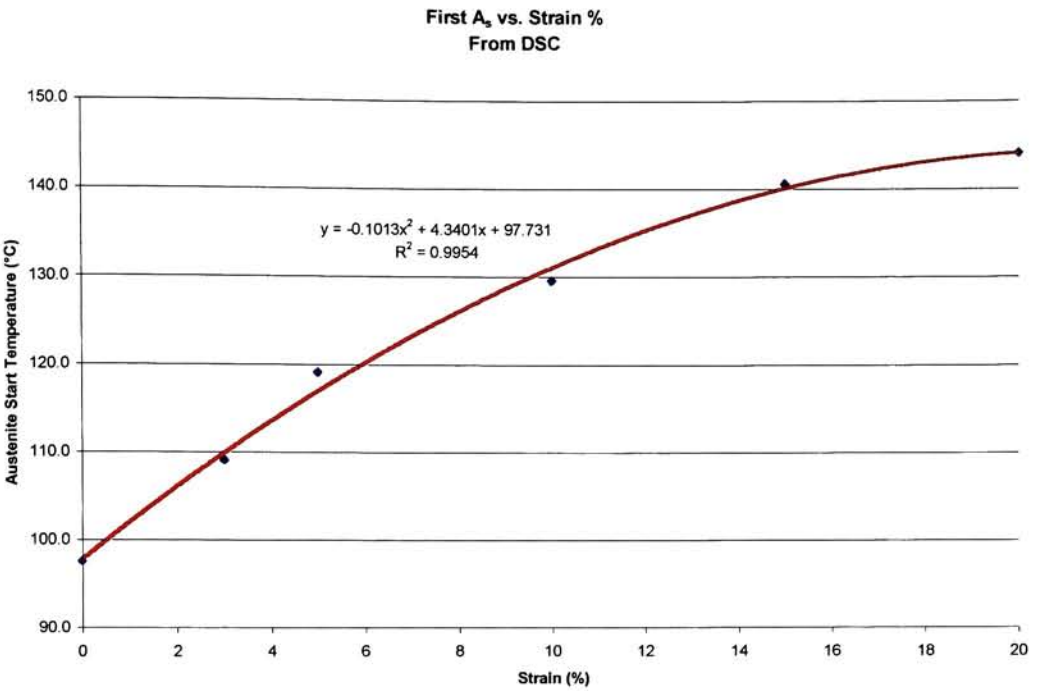

Figure 23 Trend of Initial A_s Temperatures

This shift in the austenite start transformation temperatures shows that the degree of detwinning of the martensite has a significant effect on the A_s temperature. With an increase in the amount of detwinned martensite, there is an increase in the amount of energy required to cause the martensite to austenite transformation, therefore, a higher temperature is needed.[26] The A_s and A_f are much lower and reproducible after the initial heating because the NiTi has completed one full shape memory cycle removing the deformation twins. Also, it was found that if the initial austenite transformation temperatures are not exceeded, no transformations take place as can be seen in Figure 24 by the absence of any heat flow peaks over three cycles.

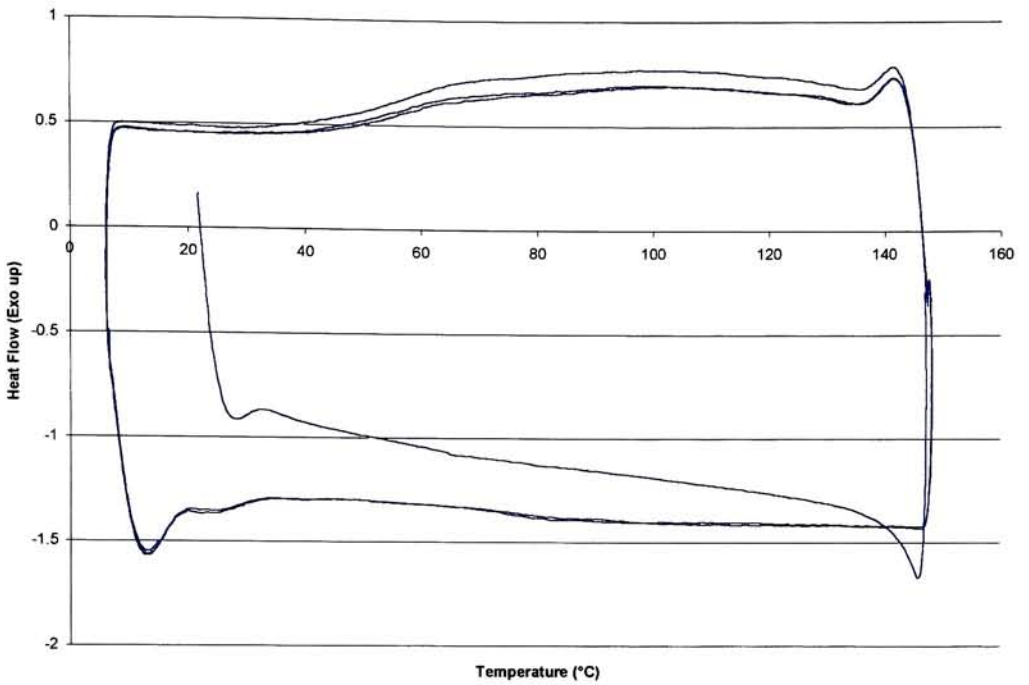

Figure 24 Absence of peaks when initial A_s and A_f not surpassed

Another observation from the DSC data was that the initial austenite transformation peaks became much flatter as the strain percentage was increased. This suggests that the sharper peaks result from a phase transformation that is extremely rapid, while the wider peaks are the result of a gradual phase transformation.[26]

The transformation temperature at the onset of martensite was plotted with respect to the prestrains and there appeared to be a linear decrease in the transformation as the prestrain was increased (Figure 25). This behavior was expected since it is known that introducing dislocations causes the M_s to decrease.[27] The dislocations were introduced through the plastic deformation caused by prestraining the samples.

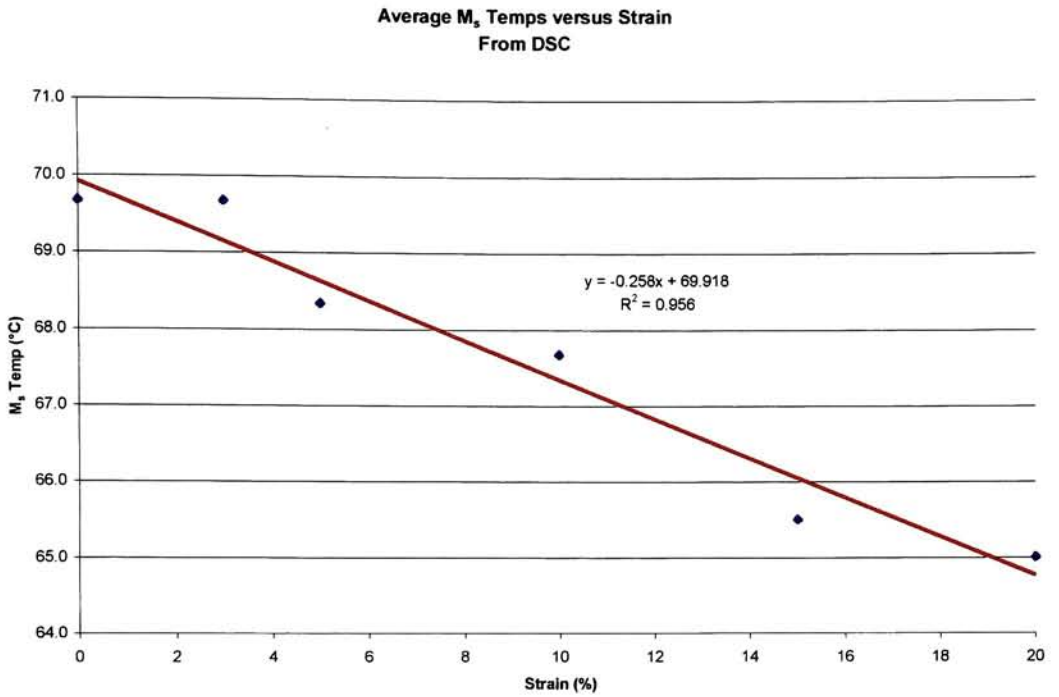

Figure 25 Average M_s temperatures as a function of prestrain

Another trend that was observed was a linear increase of the initial A_f temperature. An increase in A_f was expected since the initial A_s temperatures were found to increase with a parabolic trend, but it was found that the trend of the initial A_f temperatures was linearly increasing.

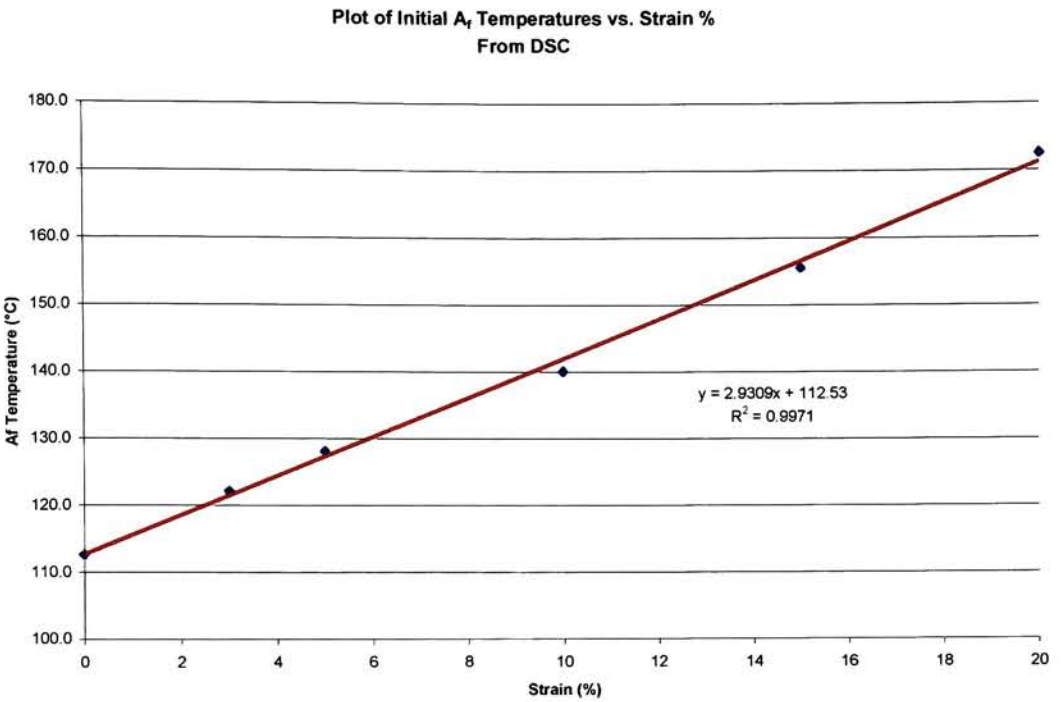

Figure 26 A_f Temperature as a function of prestrain

Dynamic Mechanical Analysis

Following the completion of all DMA experiments, the transformation temperatures were estimated using the procedure outlined in the Experimental Plan section. One of the first observations was that the elasticity values from DMA are approximately double those found from the tensile data. This difference has been attributed to an incorrect calibration of the DMA. DMA is generally used for polymers, which have much lower stiffness values and much higher loss components than most metals, especially NiTi. To properly calibrate the DMA, a metallic standard must be used.

Aside from the stiffness values being different by a factor of two, the stiffness increase from the martensite phase to the austenite phase was similar to the increase found by Carballo et al.[28] which was less than two times. It has been generally accepted that the stiffness increase that accompanies the phase change was four-fold in static conditions, but there has been few studies of the variation of Young's modulus under dynamic conditions with changing temperatures. Since the relative change in stiffness was similar to the expected values, the data was then analyzed for transition temperatures.

Following the estimation of transformation temperatures, the same relations that were developed from DSC were developed for DMA. The trend that upon the initial heating curve there was a higher A_s and A_f than the two subsequent curves is consistent with the DSC data. Figure 27 is a plot of the initial A_s temperature as a function of prestrain. The DSC trend is included for comparison.

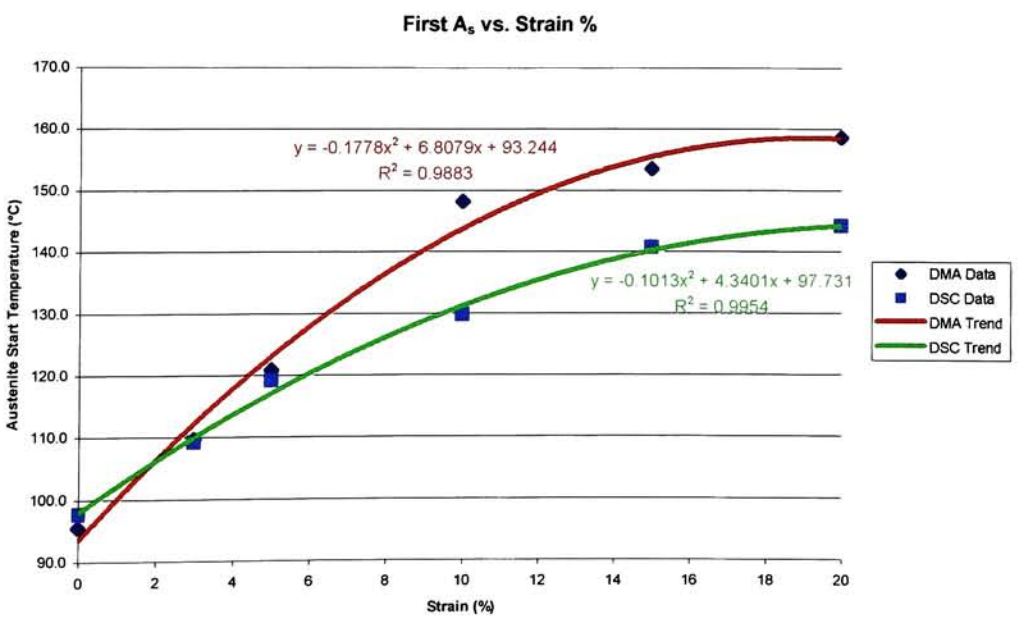

Figure 27 Initial A_s as a function of prestrain

As one can see from the figure, a parabolic relation exists from the DMA similar to the relation from DSC. The difference between the two can be attributed to the increased sensitivity of DMA.

The second relation that was studied was the M_s as a function of prestrain. From Figure 28 it is obvious that there is no linear trend as was found using DSC. Also it is interesting to note that the M_s temperatures of the higher strain samples are higher than the unstrained sample. This is opposite of what has been found in the literature. Numerous sources state that increasing the amount of cold work will decrease the M_s temperature just as found in DSC. The difference between the DSC data and the DMA data is most likely due to the differences between the experiments. In DSC, the specimen is not constrained, while in DMA, the specimen is held at a constant strain. By keeping the specimen at a constant strain, stresses are introduced, which causes a change in the transformation temperatures.

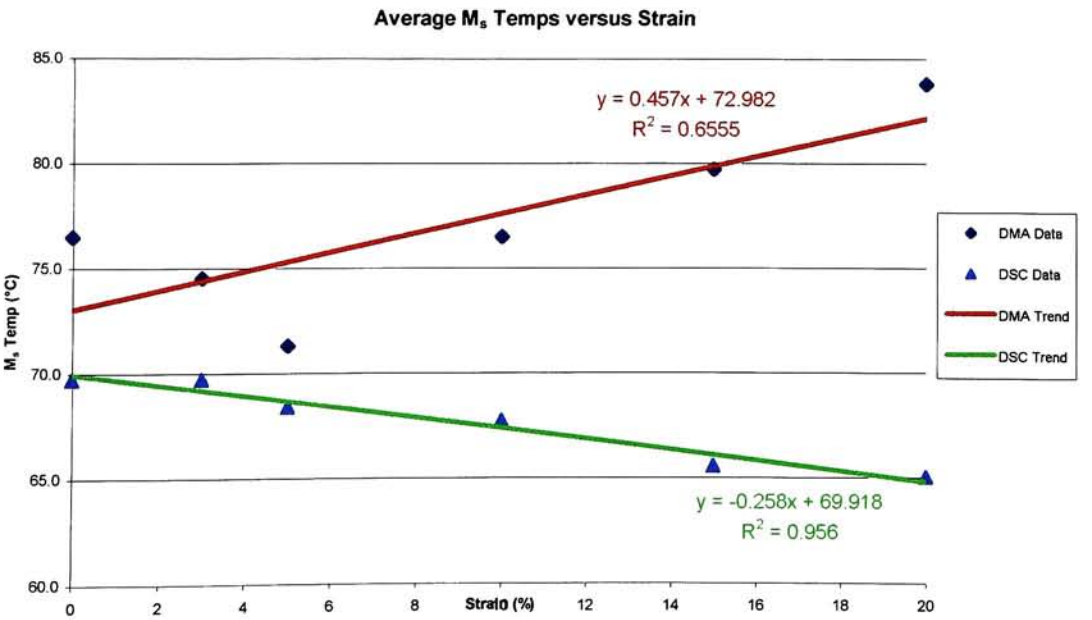

Figure 28 Average M_s temperature as a function of prestrain

The last relation studied was the initial A_f as a function of prestrain. Figure 29 shows the relation developed from DMA. The general trend is similar to the linear trend of initial A_f found from DSC.

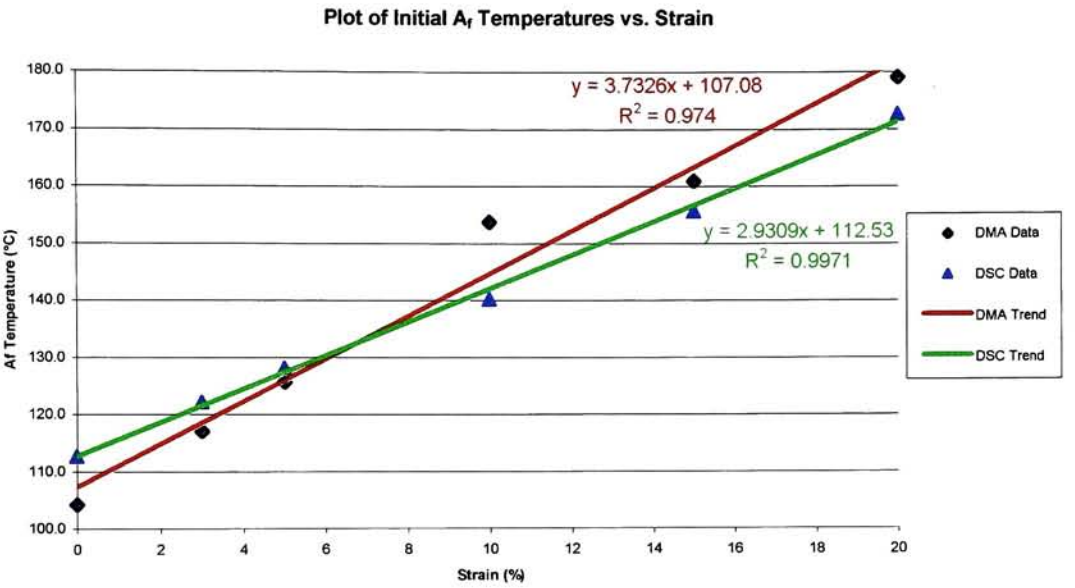

Figure 29 Initial A_f temperatures as a function of prestrain

Along with the expressions developed from the trends of transformation temperatures, it was interesting to note that there were some small dips in the stiffness as the material is heated and cooled (See Appendix G for examples). These dips were not observed in all specimens, but when they did occur, they occurred in each of the heating and cooling cycles. In the DMA study conducted by Carballo et al., they did not observe such phenomena. Since these dips occurred in both heating and cooling curves, they appear to be due to some type of secondary transition. This transition could possibly be the R-Phase that was briefly mentioned in the introduction, but it is very unlikely because the R-Phase transition usually only occurs when cooling from the parent state and it would have appeared in all the specimens. Also, since there are no additional peaks

observed in the DSC cooling curves, the R-Phase did not occur during those experiments. A different explanation of the dips could be the extreme sensitivity of DMA. The dips could be due to transition of a thin oxide layer that was not adequately removed by wet sanding. These dips made it very difficult to estimate the transformation temperatures because they added more inflection points to the curve, which are key in determining the temperatures.

Another problem that arose from determining the transformation temperatures from the DMA curves is that there is very little repeatability between cycles beyond the first cycle. In DSC, the second and third cycles were virtually right on top of one another, while the heating cooling curves were quite different. From this study it appears that the method used here to estimate the transition temperatures may not be the most accurate. Since DSC is more consistent than DMA, it gives better estimates of the transformation temperatures.

Hardness Testing

Hardness testing was performed at room temperature, therefore, all specimens were in the martensitic phase at the time of testing, based on the transformation temperatures found from DSC and DMA. After all the hardness data had been taken, the recorded values were entered into Excel for analysis. Since three numbers were taken for each indentation, those numbers were averaged to give the hardness number for that indentation, then the average of the indentation numbers was taken to be the average for the sample. The final hardness values for each specimen are listed in Table 4, and all hardness values observed can be found in Appendix A.

Table 4 Final KHN Values

Prestrain %	Knoop Hardness Number
0	287.1
3	340.1
5	347.0
10	387.4
15	413.3
20	476.7

As expected, the hardness values increase with the strain percentage. This was expected since it is known that in general hardness increases with the amount of cold work to a material.[8] When the KHN are plotted versus the prestrain percent, Figure 30 results. The increase in KHN as the prestrain was increased appeared to have a sigmoidal trend so a cubic curve was fit using Excel's trendline function. The indicated R-squared value is 0.9955, which indicates the data follows a cubic trend.

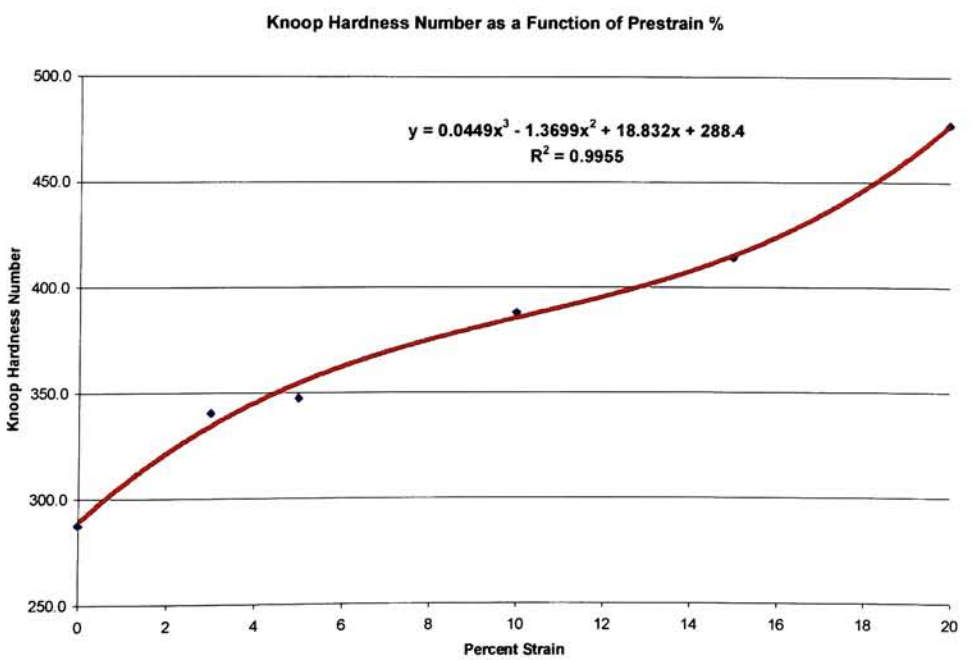

Figure 30 KHN as a function of Prestrain

As a side note, it is interesting to note that the martensitic phase has a significantly smaller hardness number than the high-temperature parent austenite phase. This is opposite of what has been observed in carbon steels.[2]

Mechanical Testing

During the prestraining of each of the specimens, load and extension data were taken. This data was then converted into engineering stress and strain values as well as true stress and strain values using the equations developed previously. The true stress and strain values were used to construct flow stress curves for each of the specimens. To illustrate the difference between the engineering stress-strain and the true stress-strain curves, the two were plotted on the same chart. These charts can be found in Appendix B.

From the true stress-strain data, the maximum true stress for each specimen was recorded and plotted against the respective true strain amounts which resulted in the following figure.

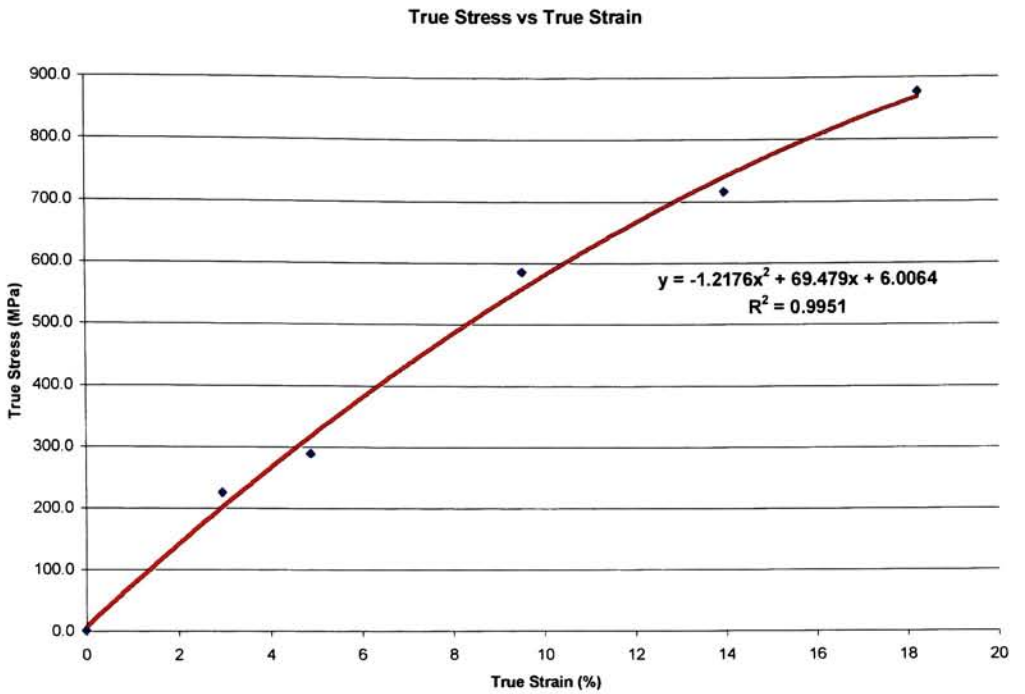

Figure 31 Max True Stress vs True Strain

After plotting the data, a best fit curve as applied to the data using Excel's trendline feature. Looking at the data there appeared to be some curvature so a second order polynomial was fit. As one can see from Figure 31, the data does follow a parabolic trend since the R^2 value is very close to 1. From the formula of this best fit curve, it is possible to calculate the maximum flow stress for any subsequent sample that is prestrained a different amount.

Another relationship that was investigated was true stress versus Knoop hardness (Figure 32). After looking at the data, it appeared that the data followed a sigmoidal curve so a third order polynomial was fit to the data using Excel's trendline feature.

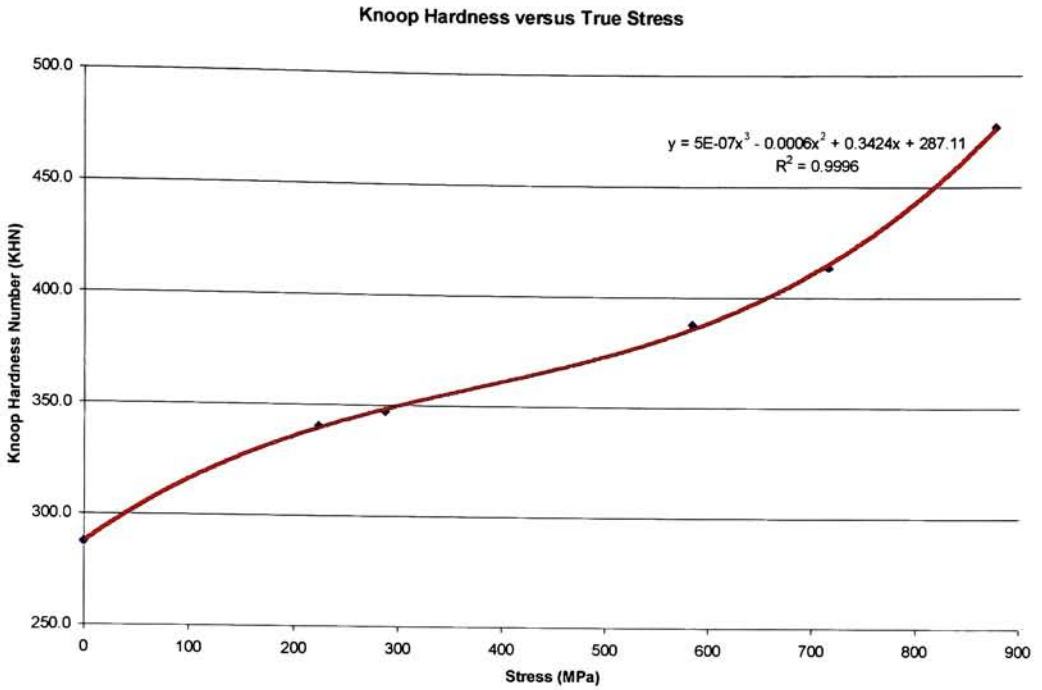

Figure 32 Knoop Hardness Number Vs True Stress

The cubic equation can be used to predict the Knoop hardness number from a known true stress value.

To find the elasticity, linear portions of the loading and unload engineering stress-strain curves were numerically differentiated using the regularization method. The results from this study can be found in Table 5.

Table 5 Modulus of Elasticity Values Found From Tensile Testing

Modulus of Elasticity (Pa)								
	Loading				Unloading			
Strain %	Max	Min	Average	Std Dev	Max	Min	Average	Std Dev
3	6.08E+10	4.37E+10	**5.10E+10**	5.88E+09	4.88E+10	3.47E+10	**4.14E+10**	4.56E+09
5	5.27E+10	2.95E+10	**4.45E+10**	8.73E+09	5.41E+10	3.33E+10	**4.34E+10**	5.22E+09
10	5.63E+10	1.22E+10	**4.65E+10**	1.53E+10	4.49E+10	3.62E+10	**4.33E+10**	2.01E+09
15	4.83E+10	3.64E+10	**4.24E+10**	5.95E+09	3.91E+10	3.26E+10	**3.78E+10**	1.91E+09
20	4.19E+10	3.85E+10	**4.06E+10**	1.37E+09	3.55E+10	3.22E+10	**3.37E+10**	1.17E+09

The range of values expected for the modulus of elasticity was 28-41 GPa.[3] As one can see from the above table, these values lie on the high side of that range as well as above the range, especially the 3-percent sample. This large difference is due to the large amount of noise in the elongation-load data that was recorded. Since approximately the same number of data points were collected for each different sample, the samples with less strain have significantly more data points for each percent elongation. Also, another source of noise in the data during the unloading portion of the test is the fact that the Instron Testing machine is screw driven. Since the displacement rate is controlled rather than the applied force, a much less smooth curve results.

Another important property of a ductile material that can be found from a tensile test is the strain hardening exponent. To find this number, a 0.2% offset yield stress was found as the onset of plastic deformation which occurs following the elastic deformation of the detwinned martensite, and a power curve of the form,

$$\sigma = K\varepsilon^n$$

was fit to the 15% and the 20% samples since it was only these two samples that had a significant amount of data in the uniform plastic region.

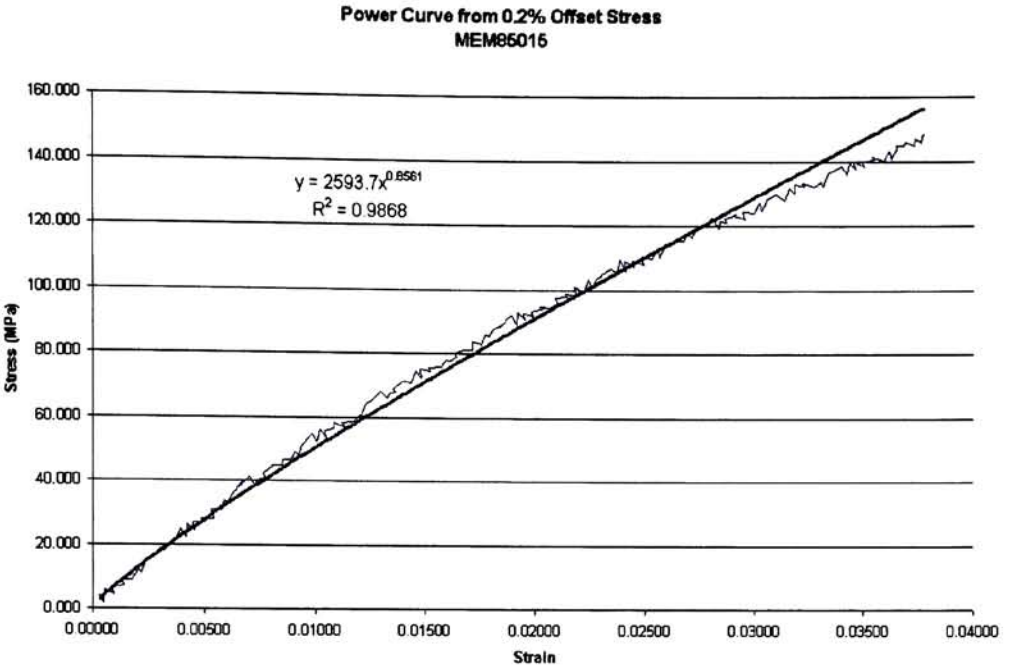

Figure 33 Power curve fit to plastic deformation region of 15% sample

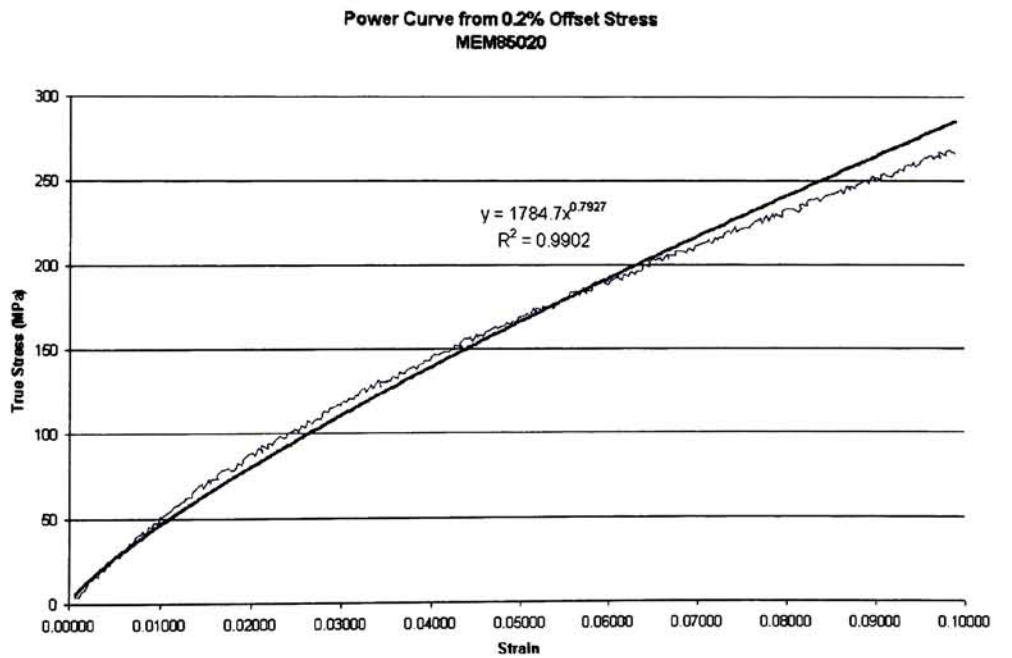

Figure 34 Power curve fit to plastic region of 20% sample

From these curve fits, the values of the strain hardening exponent and coefficient were found from the equation of the fitted curve. Some values for the strain hardening exponent and coefficient for some typical materials as well as the calculated values for NiTi are listed in Table 6. As one can see, the strain hardening exponent for NiTi is much higher than the other materials which shows that NiTi strain hardens at a rapid rate. This accounts for the difficulty in machining as well as rapid tool wear when working with NiTi.[10]

Table 6 Strain Hardening Exponents for various materials[4]

Material	n	K (psi)	K (pa)
Titanium	0.05	175000	1.21E+09
Annealed alloy steel	0.15	93000	6.41E+08
Quenched and tempered medium carbon steel	0.10	228000	1.57E+09
Molybdenum	0.13	105000	7.24E+08
Copper	0.54	46000	3.17E+08
Cu-30% Zn	0.50	130000	8.96E+08
Austenitic Stainless Steel	0.52	220000	1.52E+09
NiTi Prestrained 15%	*0.86*	*376000*	*2.59E+09*
NiTi Prestrained 20%	*0.79*	*259000*	*1.78E+09*

Another interesting occurrence that was observed during the tensile testing of the NiTi ribbon was that the material had vastly different amounts of springback after unloading. Table 7 gives the values of springback when the specimens were unloaded. For strains in the plastic region the newly created dislocations act as pinning centers for martensite twin boundaries. As the external stress is removed, the dislocations move to a new equilibrium position and they take the twin boundary with them, which results in much more unloading strain than a conventional alloy.[1]

Table 7 Springback values upon unloading

Total Loaded Strain	Total Unloaded Strain	Springback
3	2.4	0.6
5	4.2	0.8
10	8.1	1.9
15	11.1	3.9
20	16.3	3.7

X-Ray Diffraction

X-ray diffraction was performed at room temperature on polished NiTi samples that were affixed to glass slides. The NiTi was in the martensitic phase based on the determined transformation temperatures from DSC. Following the initial scan of an unstrained sample, the pattern was matched to pdf file, 35-1281. Once it was verified that the specimens had a monoclinic structure, the peaks were matched to the indices in pdf 35-1281. New lattice parameters were calculated based on the d-spacings and indices of the unstrained sample using the monoclinic plane spacing equation (22). The lattice parameters were calculated using a linear regression technique, were also calculated using nonlinear regression techniques for verification. The values calculated as well the published values can be found in Table 8.

Table 8 Monoclinic Lattice Parameters

Source	a	b	c	γ
PDF 35-1281	2.885	4.622	4.120	96.8°
Linear Regression	2.884	4.637	4.101	97.7°
Nonlinear Regression	2.879	4.614	4.097	98.0°

From these parameters, the volume of the monoclinic cell can be calculated. The volume of a monoclinic cell was calculated using the equation,

$$Volume = abc \sin \gamma$$

By calculating the volume of the monoclinic crystals in each of the specimens, the important assumption that the volume remains constant during plastic deformation can be proven. Recall that this assumption was made in order to calculate the true stress-strain curves. From the calculated volume changes, there was very little volume change associated with prestrain, where the largest change was 1.17% and the smallest was 0.05%, see Appendix D for the complete listing of lattice parameters and unit cell volume changes. Since there is such a small change in the volume of the crystals, this proves the assumption that the volume remains constant during uniform plastic deformation. After the lattice parameters were calculated for the unstrained sample, the corresponding d-spacings and 2-theta values were calculated using the indices from the pdf file and the newly calculated parameters. This new listing was then treated as the base pattern for all of the patterns produced by the prestrained samples. After the patterns were matched to the calculated spacings, the lattice parameters as well as the volume of the crystal were calculated for each specimen. The volumes were then compared to the unstrained volume to get the percent change.

The error in the volume change calculation comes from the effect the prestraining has on the plane spacings. When a grain is subjected to a uniform tensile strain perpendicular to the reflecting planes, the spacing between those planes increases uniformly, and it causes the intensity peak to shift to lower angles. This shift of the peak

made it difficult to identify the corresponding peaks, which caused a loss in accuracy in calculating the lattice parameters.

Optical Microscopy

Specimens analyzed under the optical microscope were mechanically polished to a surface finish of 0.05μm. At first glance, there did not appear to be any difference in surface appearance between samples, but as the magnification was increased, a slight difference was noticeable. The difference was the appearance of "islands" of repeating thin black stripes and wider white stripes (Figure 35 and Figure 36). These islands appear to be grains since there appears to be a definite boundary around them. Another important trait of these grains is that the size and number of them increase with the amount of prestrain applied to the sample. In the sample with no prestrain, there were very few grains with the stripes and the grains that were evident were very small and hard to see at 1000X magnification. On the high prestrain samples, these grains are visible at 50X magnification. Also, it is interesting to note that all the stripes are perpendicular to the direction of strain.

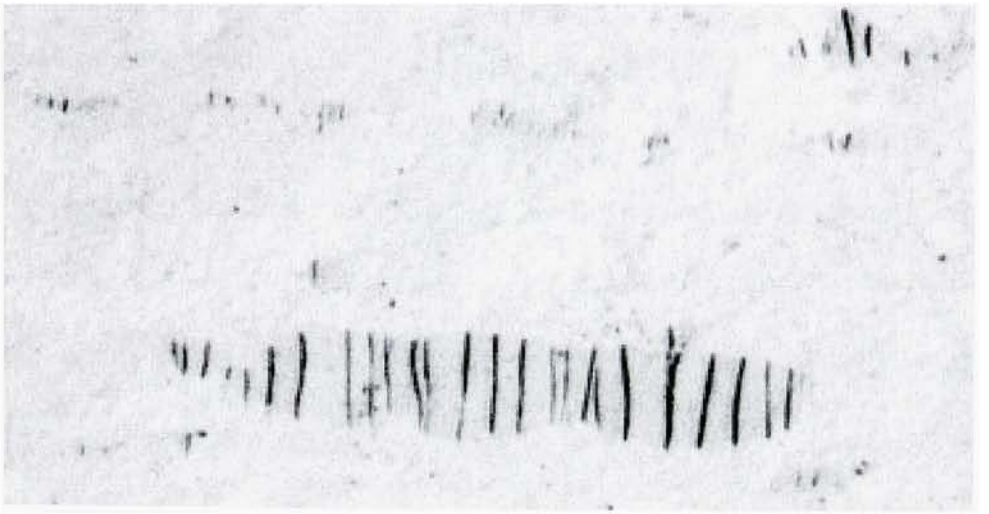

Figure 35 Brightfield Image of Striped Grain at 500X

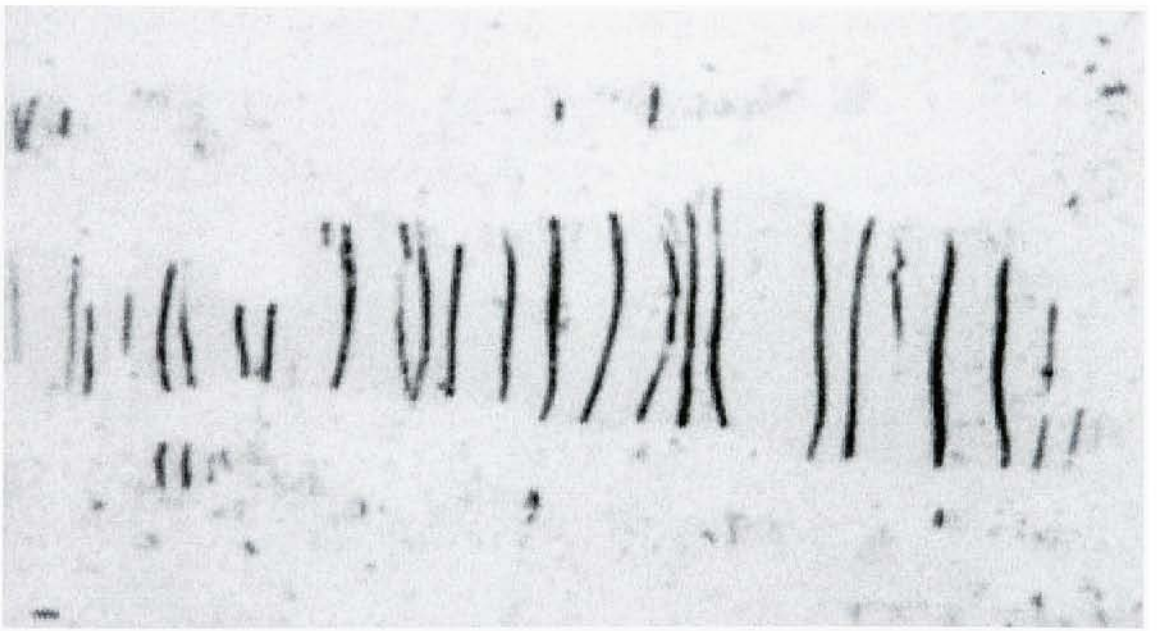

Figure 36 Brightfield Image of Striped Grain at 1000X

The entire surface of all the samples were scanned, and in every sample, the stripes within the grains were perpendicular to the direction of strain. Since the light source was normal to the specimen surface, it was clear that the dark stripes were very small crevices. When the light was shifted from normal, the white stripes appeared to cast a shadow, which indicated that they were protruding from the surface. After a

thorough search of the literature containing the microstructures of NiTi, no similar characteristics were found for equiatomic NiTi, or the Ni_2Ti precipitate that may be present. Based on the phase diagram and the heat treatment, less than 4 percent of Ni_2Ti should be present.[10] Since there appeared to be a difference in the heights between the differently colored areas, one of the grains was analyzed using Atomic Force Microscopy, which is capable of generating a 3-dimensional image of the surface.

Atomic Force Microscopy

Atomic Force Microscopy was used to analyze the topography of the NiTi surface following analysis under the optical microscope. From the AFM scan, it was found that the surface roughness was approximately 50 nm, or 0.05 μm as expected from the final polishing step.

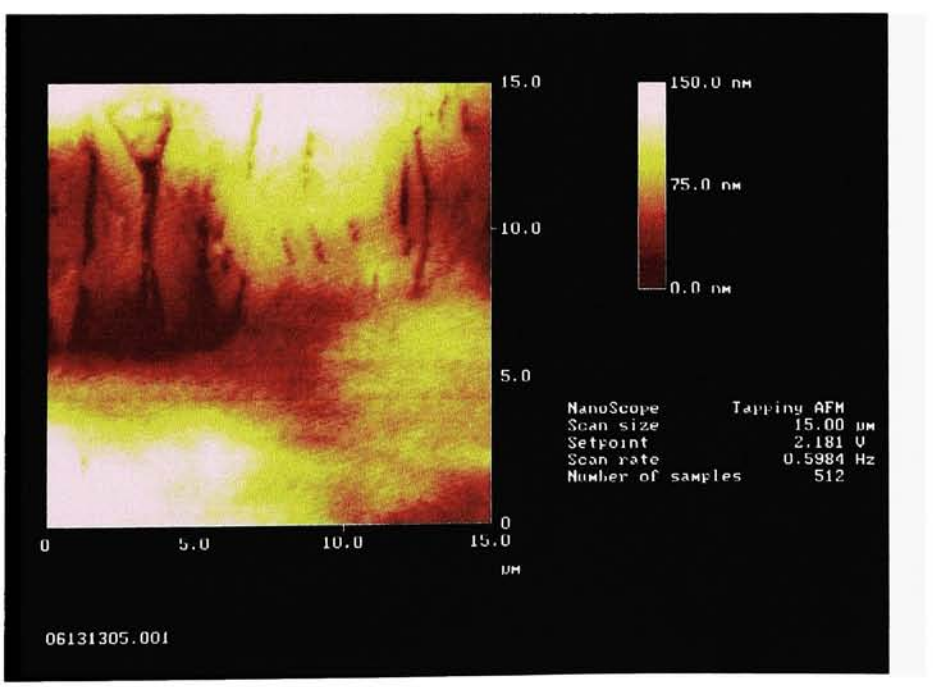

Figure 37 2-Dimensional AFM Image

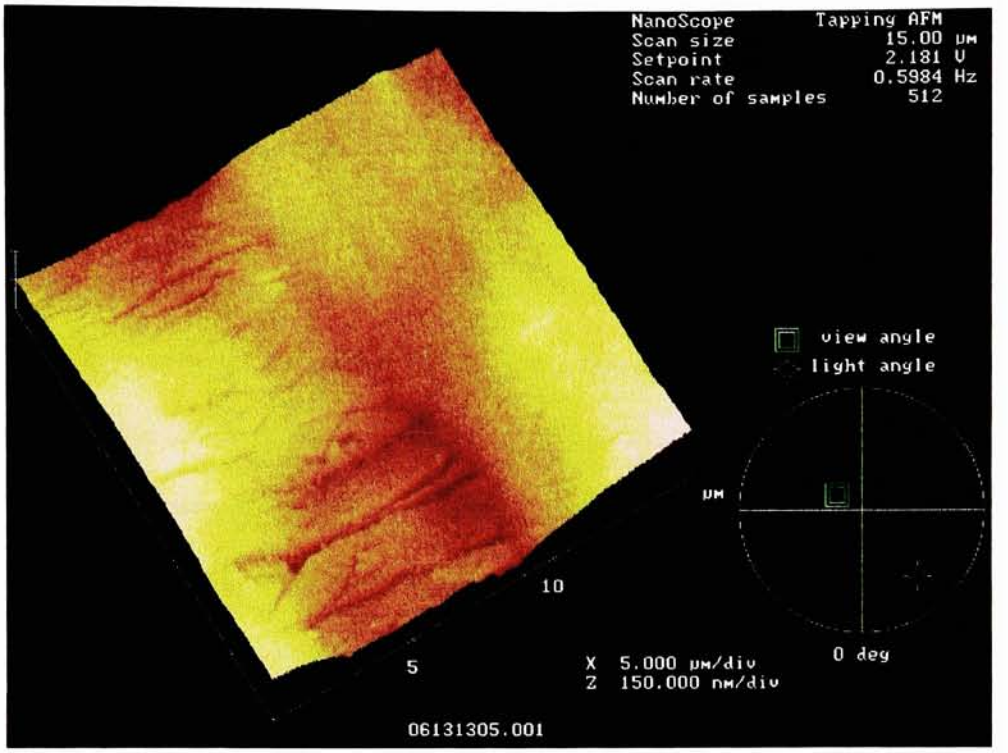

Figure 38 3-Dimensional AFM Image

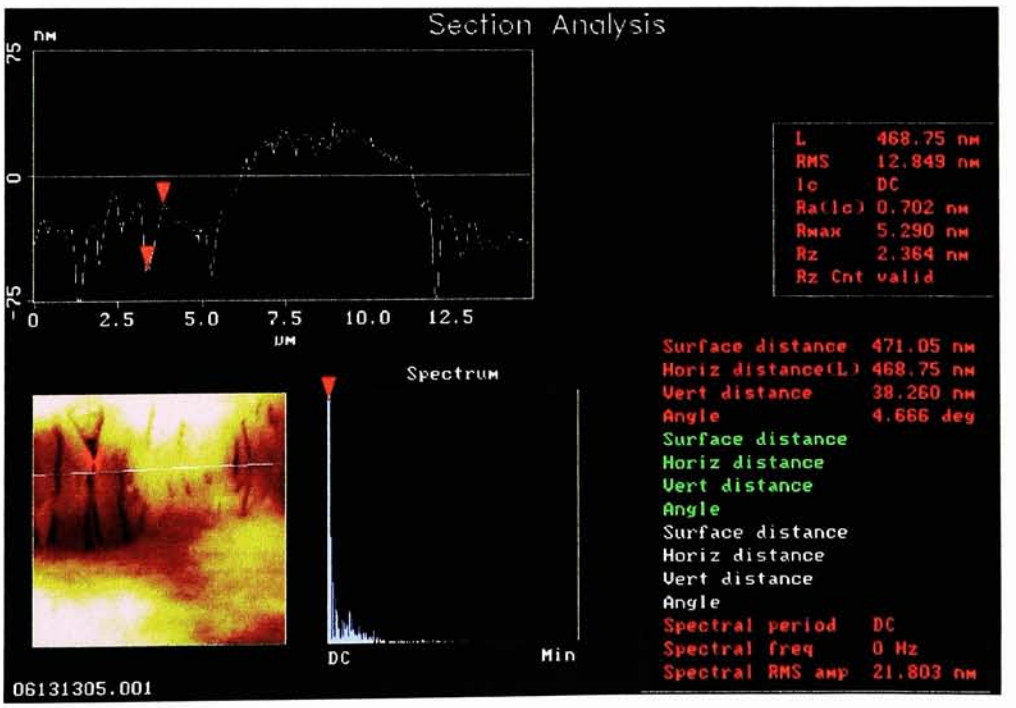

Figure 39 Section View of AFM Image

From Figure 39 it can be seen that the depth of the measured crevice is 38.26 nm. The measured width was found to be approximately 600 nm. The width and depth of several crevices were investigated, and it was found that the depth was around 40 nm and the widths ranged from 600-700 nm.

Based on the images seen through optical and atomic force microscopy as well as an extensive literature search, it appears that these grains are those that are oriented in such a way that the accommodated martensite produced the shapes seen. This conclusion comes from the fact that all samples including the zero prestrain sample exhibited these grains on the surface. Since the amount and size of these grains increase with prestrain amount and that it is known that variants of martensite reorient to ones that best accommodate the applied stress, it appears that the variant which allows the best stress accommodation are the ones that produce the observed stripes. Again, this hypothesis is only a best guess because the necessary equipment to study this phenomenon was not available.

Verification of Developed Correlations

To verify the correlations developed by this study, a sample was prepared separately from the original six and was prepared with the same heat treatments and polishing methods as the original specimens. The only difference is that the sample was given a prestrain of 17%. From Figure 23, the following relation was developed for predicting the initial A_s transformation temperature from DSC.

$$y = -0.1013x^2 + 4.3401x + 97.731$$

From this equation it was calculated that that the initial A_s would be approximately 141.7°C. A DSC scan was run using the same procedure as the previous samples and an initial A_s of 142°C was found. Figure 40 is Figure 23 repeated with the A_s value for the 17% sample included (green dot).

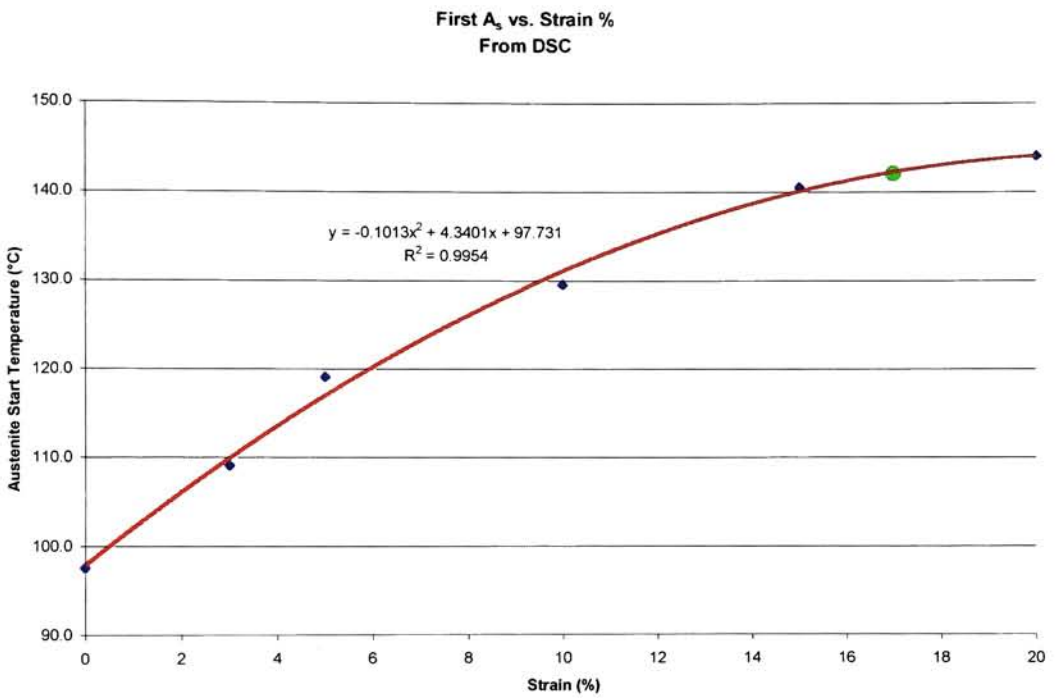

Figure 40 Initial A_s as a function of prestrain from DSC

A similar expression for the initial A_s was developed using DMA and it is,

$$y = -0.1778x^2 + 6.8079x + 93.244$$

From this expression, it was predicted that the initial A_s should be 157.5°C. After completing the first heating DMA cycle, it was found that there was an unusual dip in stiffness modulus right around the expected A_s temperature (Figure 41). The cause of this large dip is unknown, but since it is was not repeated in any of the subsequent cycles

and it was not seen in any of the other samples, possibly it could have been caused by misalignment.

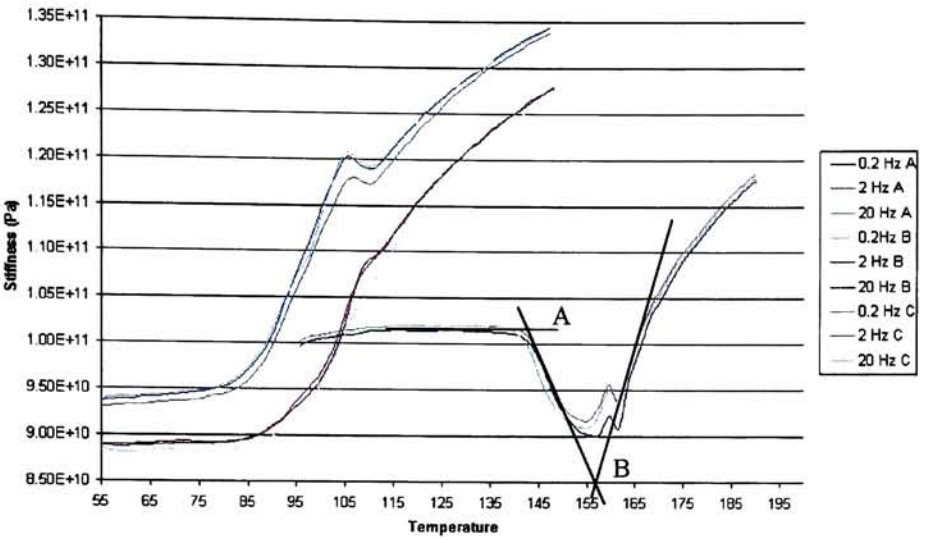

Figure 41 DMA Heating Curves for 17% Sample

When the transformation temperature was found as in the previous samples, shown as point A, a value of 142.3°C was found. If the high initial stiffness is ignored and the decrease is considered the baseline, the A_s was found to be 156.7°C, which is almost exactly the predicted value. Figure 27 is repeated in Figure 42 with the addition of the two observed points, where the green dot represents method A from Figure 41, and light blue dot represents method B.

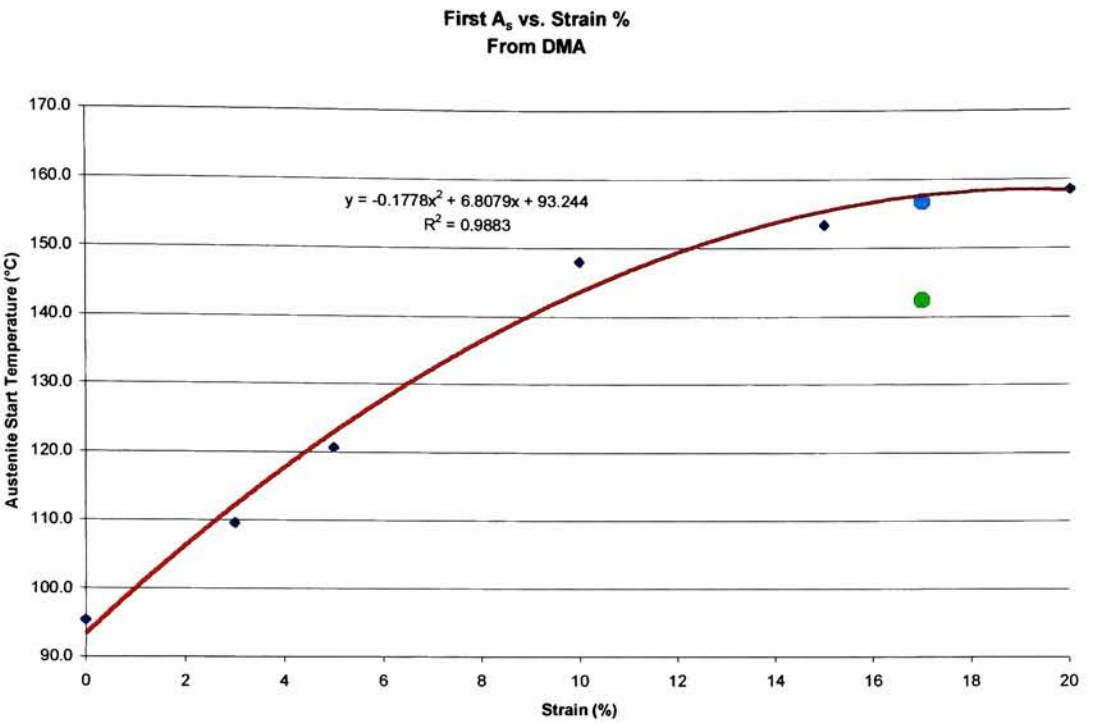

Figure 42 Initial A_s from DMA

Another relation that was developed from DSC data was a linear decrease in M_s temperature. The expression that describes the decrease is,

$$y = -0.258x + 69.918$$

From this expression the prediction of M_s for a 17% prestrain was 65.5°C. The actual value that was found from the cooling curves was 65.2°C, which again is very close to the predicted value. In Figure 43, Figure 25 is repeated where the average M_s temperature for the 17% sample is included as the green dot.

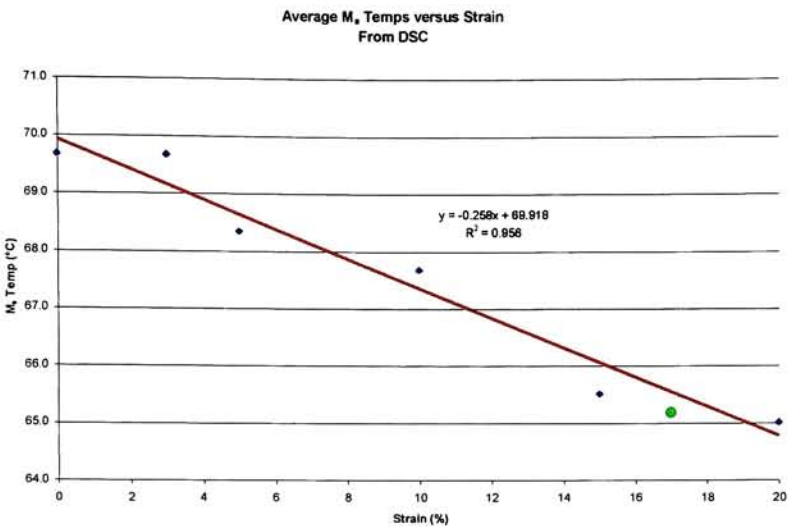

Figure 43 Average Ms from DSC

The relation of the linearly decreasing M_s was not found to exist from the DSC data. Figure 44 shows the trend of M_s from DMA and it is obvious that a linear decreasing trend does not exist. This difference was probably due to the difficulty in estimating the transformation temperatures from the DMA stiffness curves.

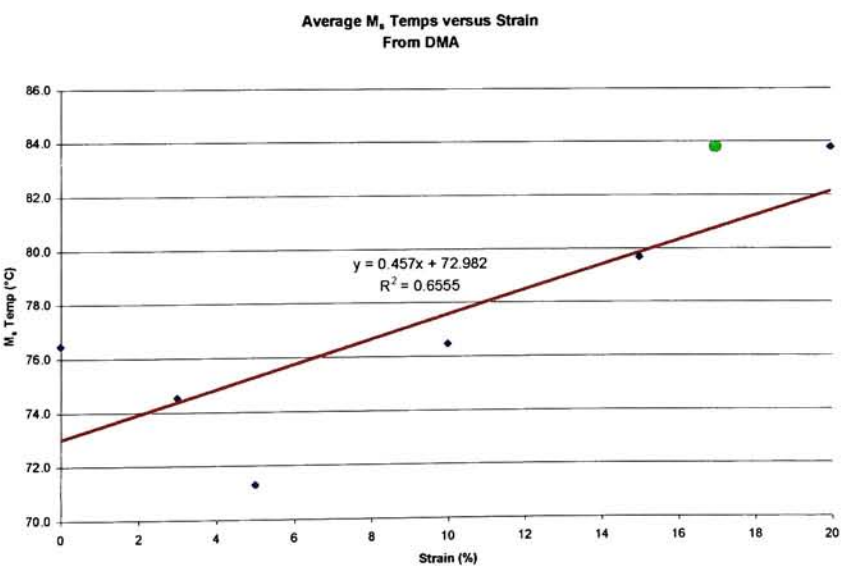

Figure 44 Average M_s temperatures from DMA

The third relationship that was developed from transformation temperatures studied through DSC and DMA is the Initial A_f temperature. From DSC, it was found that there was a linear increase in the A_f temperature that is described by,

$$y = 2.9309x + 112.53$$

From this expression it was predicted that the A_f should be approximately 162.4°C, and it was found from the DSC initial heating curve that the A_f temperature was 154.0°C. Figure 26 is repeated as Figure 45 with the addition of the point for the 17% prestrained sample. As one can see, the point does not fall along the expected trend.

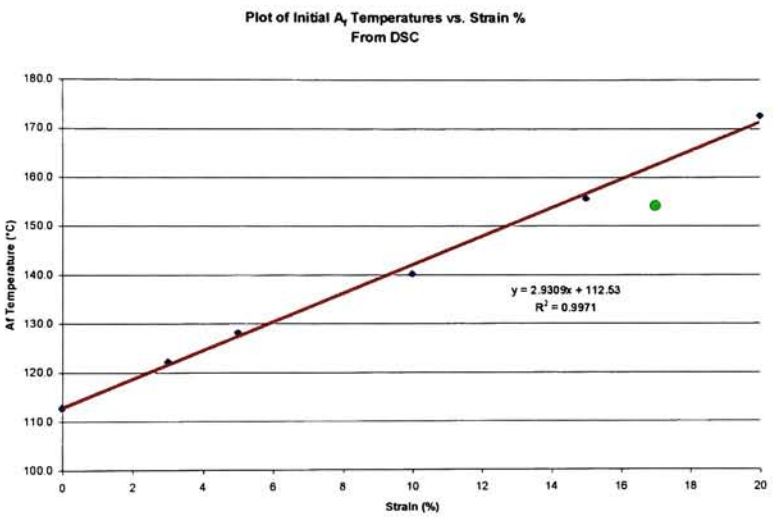

Figure 45 Initial A_f Temperature from DSC

A similar trend was observed in the initial A_f estimate from the DMA heating curves. The expression describing the trend is,

$$y = 3.7326x + 107.08$$

Using this expression, it was estimated that the first A_f should be 170.5°C, and it was found from the experiment that the A_f temperature was 169.2°C. Figure 46 is Figure 29 repeated with the addition of the data point from the 17% prestrained sample.

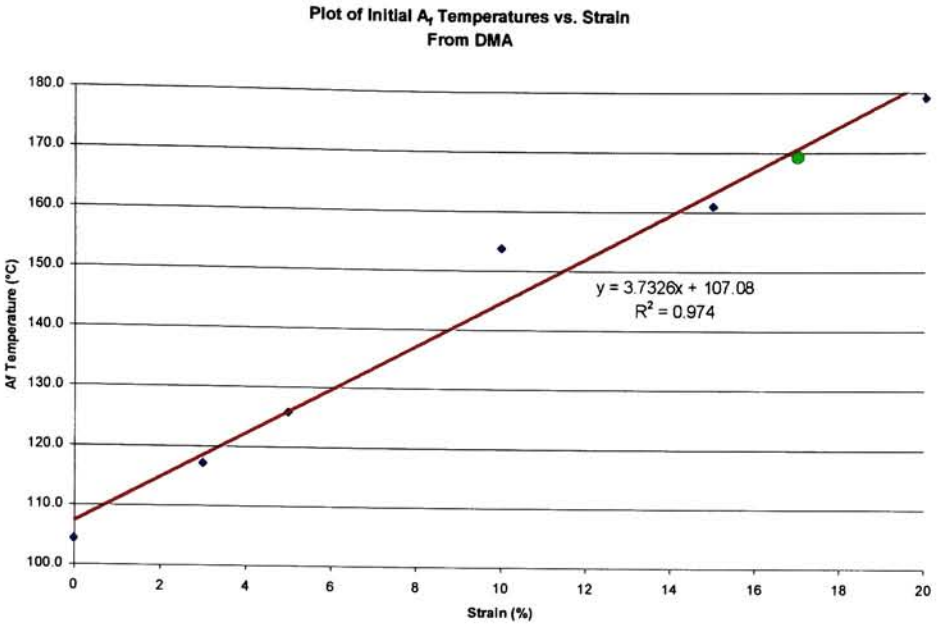

Figure 46 Initial A_f Temperature from DMA

A complete listing of the transformation temperatures found through DSC and DMA can be found in Table 9 and Table 10 respectively.

Table 9 Transformation temperatures for 17% sample from DSC

Run #	A_s	A_f	M_s	M_f
1	142	154	64.5	49.5
2	83.5	102.5	65.5	50.5
3	85	101	65.5	50.5

Table 10 Transformation temperatures for 17% sample from DMA

	A_s			A_f			M_s			M_f		
	0.2	2	20	0.2	2	20	0.2	2	20	0.2	2	20
Run #												
1	143.0	143.0	141.0	169.0	170.5	168.0	90.5	90.5	91.0	36.5	37.0	39.0
2	94.5	94.5	97.0	116.5	127.0	126.5	90.5	89.0	93.0	42.0	41.0	40.5
3	85.0	85.5	83.0	128.0	125.5	128.0	94.0	94.0	93.0	47.0	41.0	41.0

Not only were the relations generated for predicting transformation temperatures tested, the hardness relations as well as the calculated mechanical properties were tested. From the data taken while the specimen was being strained, the modulus of elasticity can be calculated by using the same methods described previously. After finding the slope of the linear portions of the loading and unloading curves, the values were tabulated in Table 11.

Table 11 Modulus of Elasticity determined from tensile data for 17% sample

Modulus of Elasticity (Pa)							
Loading				Unloading			
Max	Min	Average	Std Dev	Max	Min	Average	Std Dev
3.98E+10	3.02E+10	3.50E+10	4.81E+09	3.68E+10	3.31E+10	3.43E+10	1.43E+09

From the tensile data, the flow curve was generated showing the true stress and strain. A power curve was fit to the uniform plastic deformation region with the same procedure used to fit a power curve to the 15% and 20%. The exponent and coefficient calculated by Excel's trendline feature are shown in Table 12. The curve fit is shown in Figure 47.

Table 12 Strain hardening exponent

n	K (psi)	K (Pa)
0.83	339000	2.34E+09

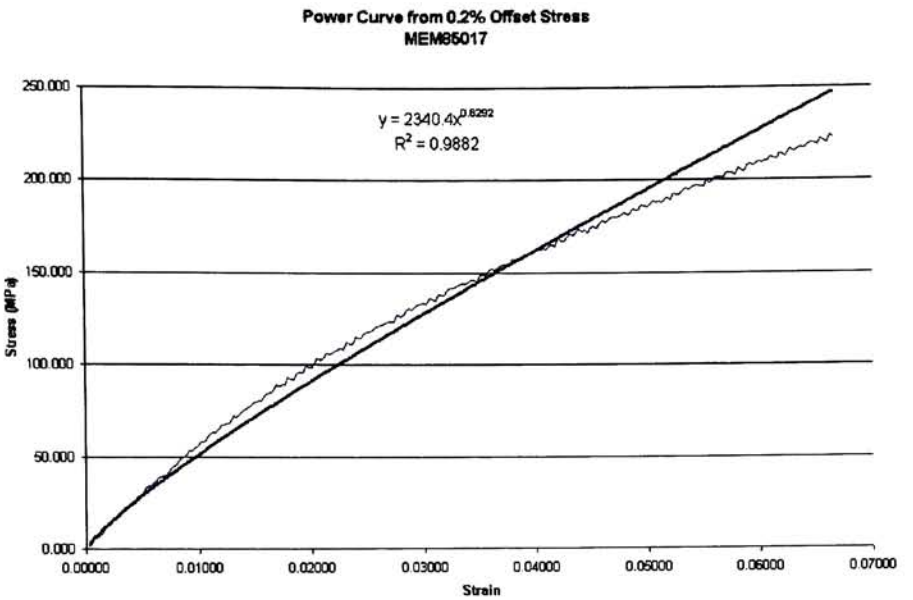

Figure 47 Power curve for 17% sample

Also from the true data, the max flow stress value was found to be 772.8 MPa. Previously the following expression was developed to predict this value,

$$\sigma = -1.2176\varepsilon^2 + 69.479\varepsilon + 6.0064$$

From this expression a max flow stress of 835.3 MPa was calculated. Figure 31 is repeated with the addition of the 17% stress value included as the green dot.

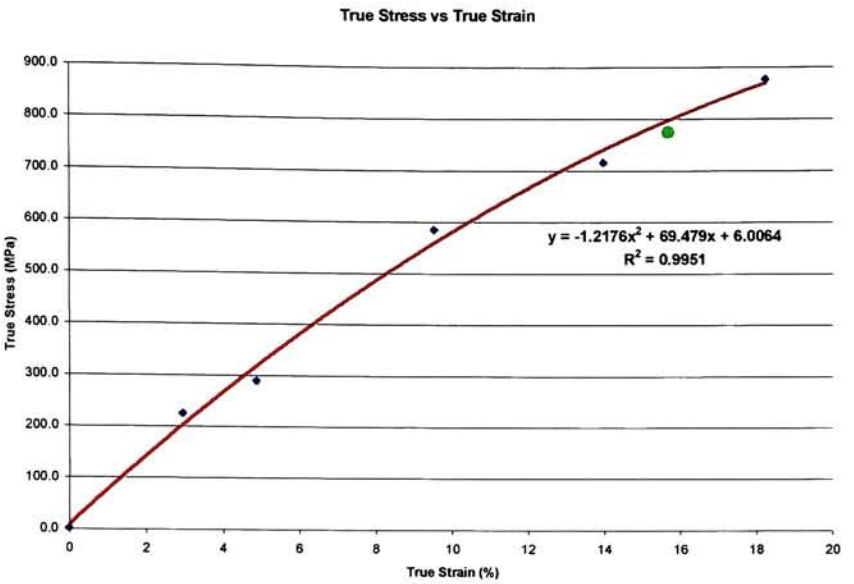

Figure 48 Maximum true stress values

As one can see from the figure, the true stress value lies reasonably close to the predicted value.

The last two relations that were verified involved the Knoop hardness number. The first relation was between KHN and strain percent. The expression that was developed is,

$$KHN = 0.0449\varepsilon^3 - 1.3699\varepsilon^2 + 18.832\varepsilon + 288.4$$

From this expression the predicted value of KHN was 433.2. After performing microhardness testing with the same load and same duration as previously used, the final KHN for the 17% sample was found to be 425.1. Figure 30 is repeated as Figure 49 with the addition of the 17% sample KHN data point added. All hardness values that were taken for the 17% sample are shown in Table 13.

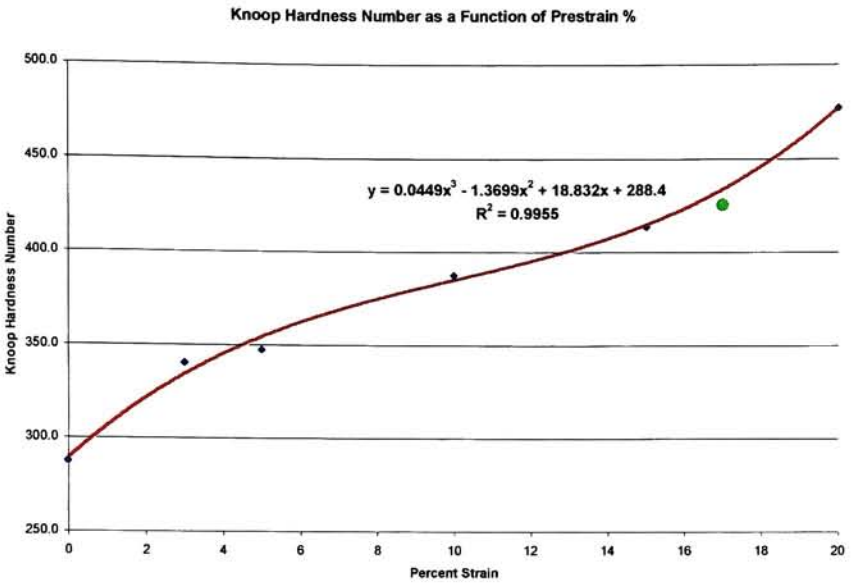

Figure 49 KHN as a function of prestrain

Table 13 Knoop hardness values for 17% Sample

Indentation	KHN #1	KHN #2	KHN #3	Average
1	405.0	407.0	403.5	405.2
2	393.3	400.3	394.9	396.2
3	430.6	426.7	431.0	429.4
4	406.4	403.7	406.1	405.4
5	436.9	432.4	436.4	435.2
6	433.0	433.5	437.0	434.5
7	423.0	427.8	427.4	426.1
8	421.8	428.6	429.6	426.7
9	459.8	463.9	460.8	461.5
10	432.0	432.0	429.2	431.1
				425.1

From the KHN versus true stress data, the following cubic polynomial was found to predict the Knoop hardness when the true stress is known.

$$KHN = 5E-07\sigma^3 - 0.0006\sigma^2 + 0.3424\sigma + 287.11$$

At 17% strain, the true stress was 772.8 Mpa, and the hardness was predicted to be 424.1. As one could see from Table 13, the KHN for the 17% sample was found to be

425.1, and Figure 32 is repeated below with the addition of the KHN value found from the 17% sample

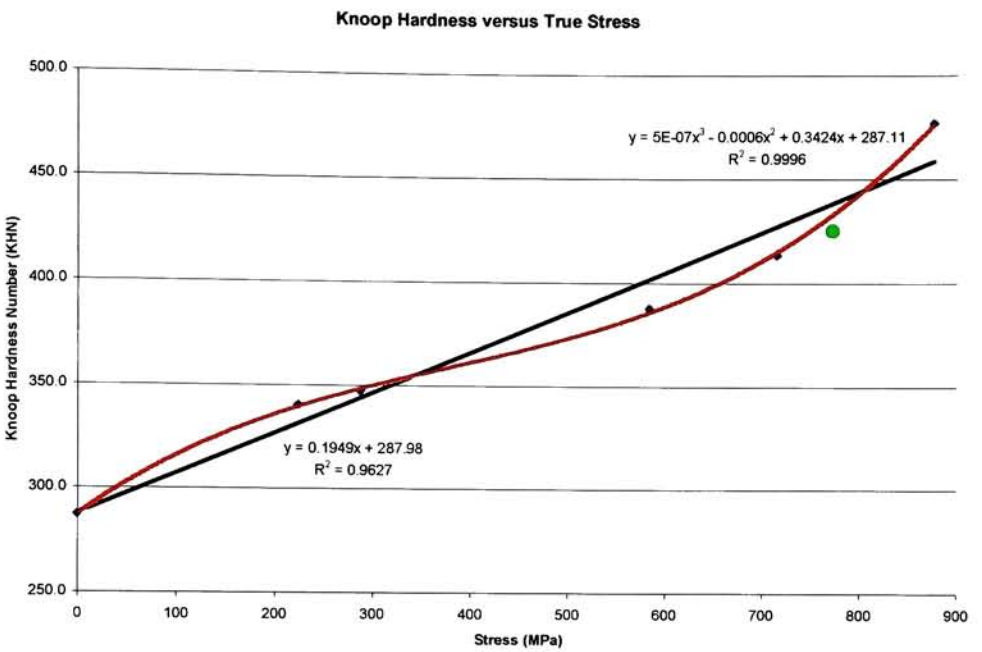

Figure 50 KHN as a function of true stress

Conclusions

In this study it was shown that the amount of prestrain applied to a NiTi specimen changed many of the material's properties. Transformation temperatures, mechanical properties, crystal properties and optical microscopy characteristics were the four areas investigated.

Transformation Temperatures:

Transformation temperatures were determined using DSC, and it was found that with increasing prestrain,

- Initial A_s increased parabolically
- Initial A_f increased linearly
- M_s decreased linearly

Transformation temperatures were also determined using DMA, and it was found that with increasing prestrain,

- Initial A_s increased parabolically
- Initial A_f increased linearly
- M_s had no trend

Mechanical Properties:

Knoop hardness tests were conducted using a Mitutoyo hardness tester, and stress-strain data was collected from deformation tests using an Instron UTS. With increasing prestrain:

- KHN increased linearly
- Flow Stress at each strain point followed a parabolic trend
- KHN increased cubically with increased stress
- Strain Hardening coefficient was found to be higher than most materials

Crystal Properties:

Using X-Ray diffraction techniques, the crystal properties were determined. A monoclinic crystal structure was observed with lattice parameters a = 2.884, b = 4.637, c = 4.101, $\gamma = 97.7°$. It was also observed that there was no change in the unit cell volume as the material was plastically strained, which verifies the constant volume during uniform plastic deformation assumption made during mechanical analysis.

Optical Microscopy Characterization

Using an optical microscope, large grains were observed, which had stripes normal to the prestrain direction. The occurrence and size of these grains

increased with the amount of prestrain. Surface scans using atomic force microscopy showed that these stripes were all approximately the same depth and regularly spaced. These grains appeared to be self-accommodated martensite regions but could not be fully characterized with these experiments.

Appendicies

Appendix A

Microhardness of MEM85000
0% Final Strain
LOAD = 100 gm
T = 12 sec

Indentation	KHN #1	KHN #2	KHN #3	Average
1	298.1	301.5	297.3	299.0
2	287.1	292.2	289.9	289.7
3	293.2	293.5	290.3	292.3
4	280.8	278.5	277.3	278.9
5	283.1	284.8	282.6	283.5
6	284.5	284.3	282.2	283.7
7	282.3	285.6	281.0	283.0
				287.1

Microhardness of MEM85003
3% Final Strain
LOAD = 100 gm
T = 12 sec

Indentation	KHN #1	KHN #2	KHN #3	Average
1	343.1	344.2	342.7	343.3
2	338.4	338.8	341.4	339.5
3	338.4	336.5	337.9	337.6
4	338.8	337.0	338.8	338.2
5	343.0	338.0	344.0	341.7
				340.1

Microhardness of MEM85005
5% Final Strain
LOAD = 100 gm
T = 12 sec

Indentation	KHN #1	KHN #2	KHN #3	Average
1	358.2	357.7	356.9	357.6
2	354.5	360.9	357.0	357.5
3	369.0	369.6	360.1	366.2
4	334.5	328.3	328.8	330.5
5	348.1	342.6	343.6	344.8
6	339.9	339.7	341.2	340.3
7	331.8	335.4	328.8	332.0
				347.0

Microhardness of MEM85010
10% Final Strain
LOAD = 100 gm
T = 12 sec

Indentation	KHN #1	KHN #2	KHN #3	Average
1	397.0	397.6	399.6	398.1
2	430.3	429.5	431.2	430.3
3	414.9	415.5	417.6	416.0
4	404.0	404.4	406.7	405.0
5	410.5	410.8	413.7	411.7
6	419.7	416.1	419.9	418.6
7	445.6	447.7	448.3	447.2
8	369.6	372.0	369.7	370.4
9	345.8	344.4	343.2	344.5
10	342.2	341.9	338.2	340.8
11	385.4	387.4	388.0	386.9
12	360.9	364.5	363.6	363.0
13	361.8	362.9	360.4	361.7
14	329.6	328.6	330.2	329.5
				387.4

Microhardness of MEM85015
15% Final Strain
LOAD = 100 gm
T = 12 sec

Indentation	KHN #1	KHN #2	KHN #3	
1	407.3	410.4	415.3	411.0
2	400.9	399.7	400.3	400.3
3	404.2	407.4	407.1	406.2
4	405.4	408.3	408.2	407.3
5	415.7	412.4	418.0	415.4
6	431.9	430.6	432.8	431.8
7	421.8	422.8	419.8	421.5
				413.3

Microhardness of MEM85020
20% Final Strain
LOAD = 100 gm
T = 12 sec

Indentation	KHN #1	KHN #2	KHN #3	Average
1	504.8	502.3	502.6	503.2
2	506.0	500.6	509.9	505.5
3	480.3	475.6	475.4	477.1
4	458.7	457.7	450.3	455.6
5	473.0	474.3	472.4	473.2
6	452.8	453.8	453.4	453.3
7	468.2	469.5	469.6	469.1
				476.7

Appendix B

True Stress – Strain Plots for each Specimen

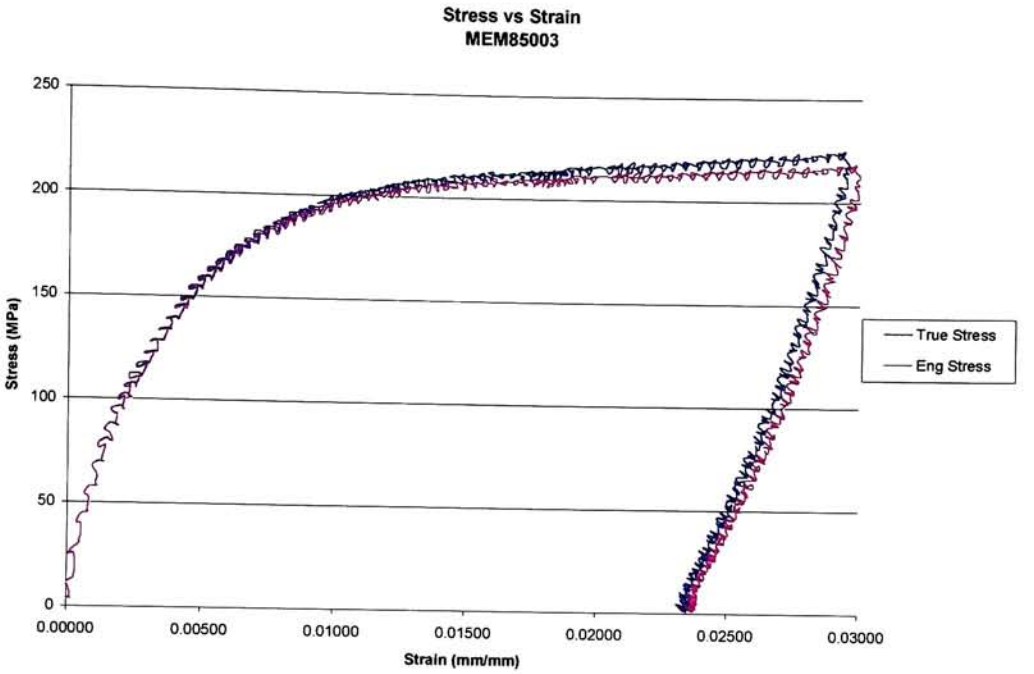

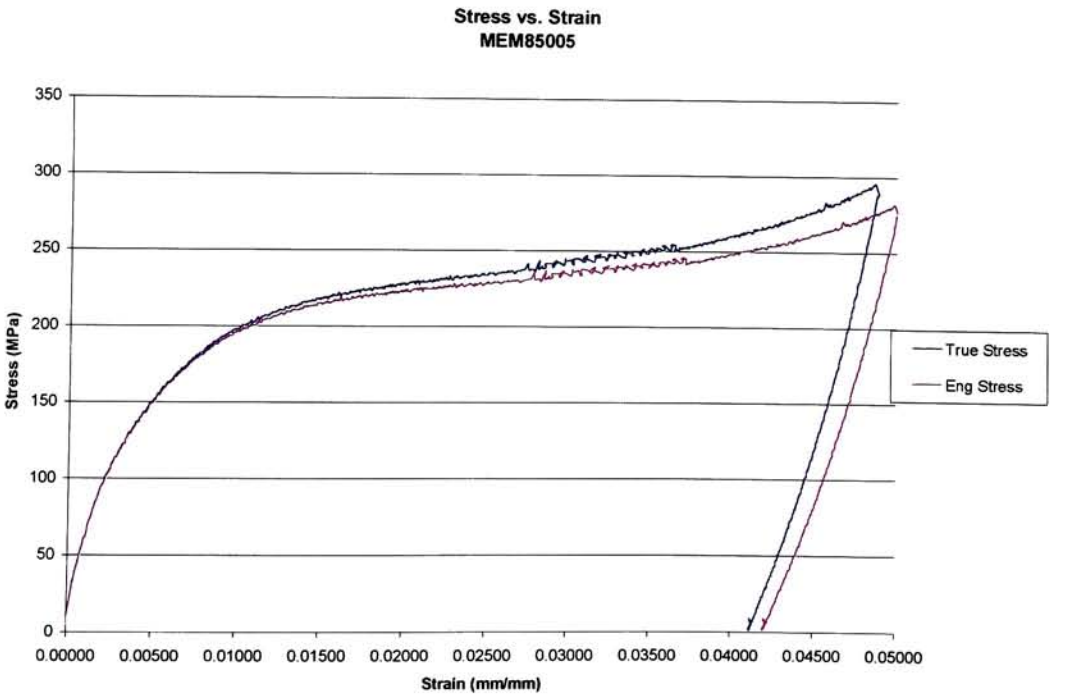

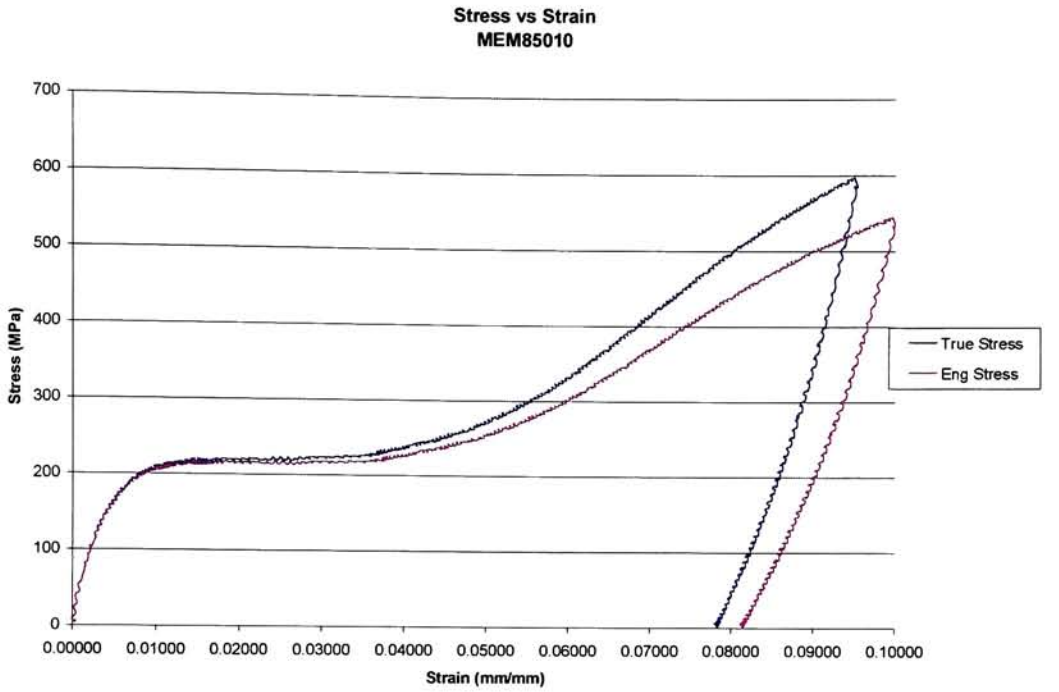
Stress vs Strain
MEM85010
700
600
500
400
300
200
100
0
Stress (MPa)
0.00000
0.01000
0.02000
0.03000
0.04000
0.05000
0.06000
0.07000
0.08000
0.09000
0.10000
Strain (mm/mm)
True Stress
Eng Stress

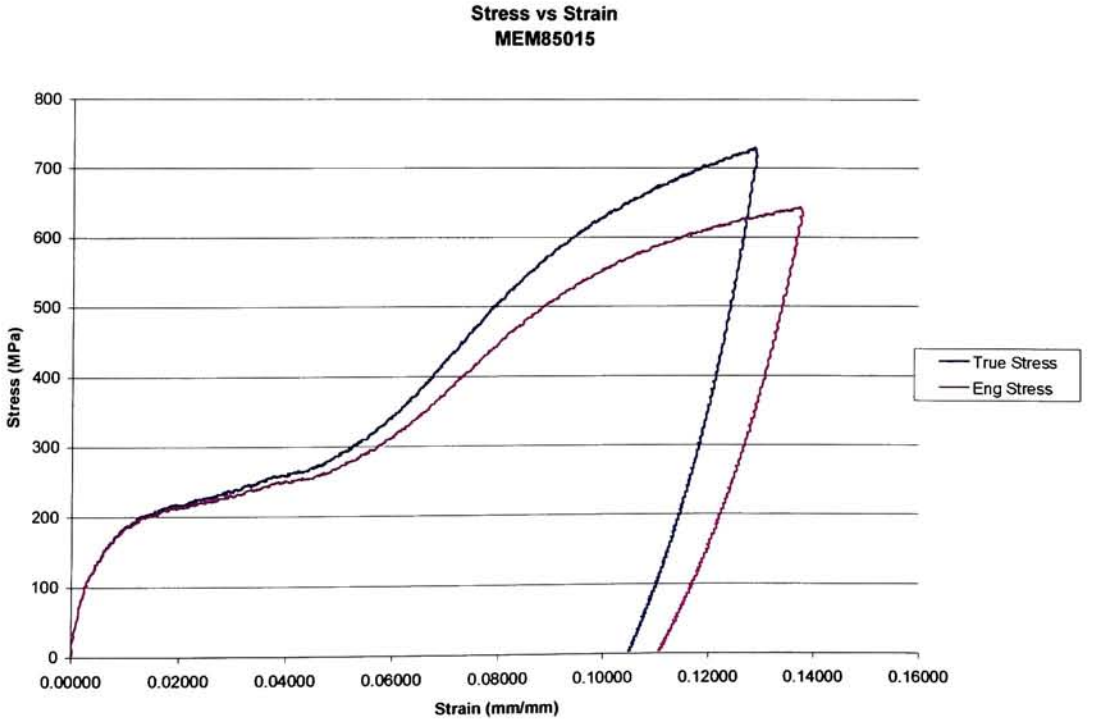
Stress vs Strain
MEM85015
800
700
600
500
400
300
200
100
0
Stress (MPa)
0.00000
0.02000
0.04000
0.06000
0.08000
0.10000
0.12000
0.14000
0.16000
Strain (mm/mm)
True Stress
Eng Stress

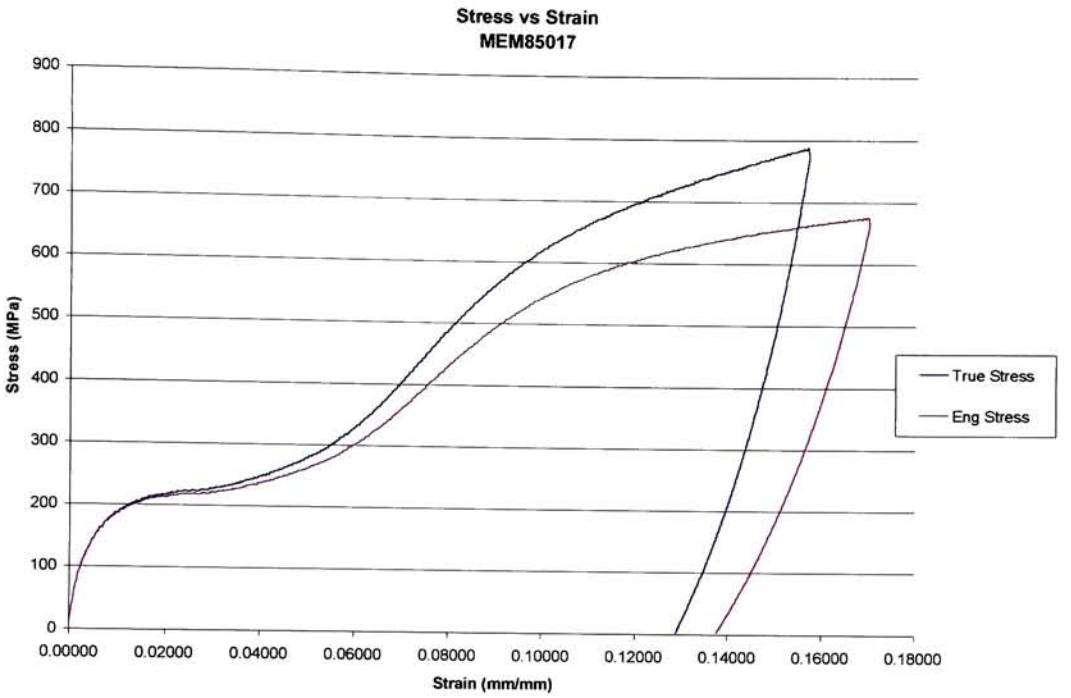
Stress vs Strain
MEM85017
900
800
700
600
500
400
300
200
100
0
Stress (MPa)
0.00000
0.02000
0.04000
0.06000
0.08000
0.10000
0.12000
0.14000
0.16000
0.18000
Strain (mm/mm)
True Stress
Eng Stress

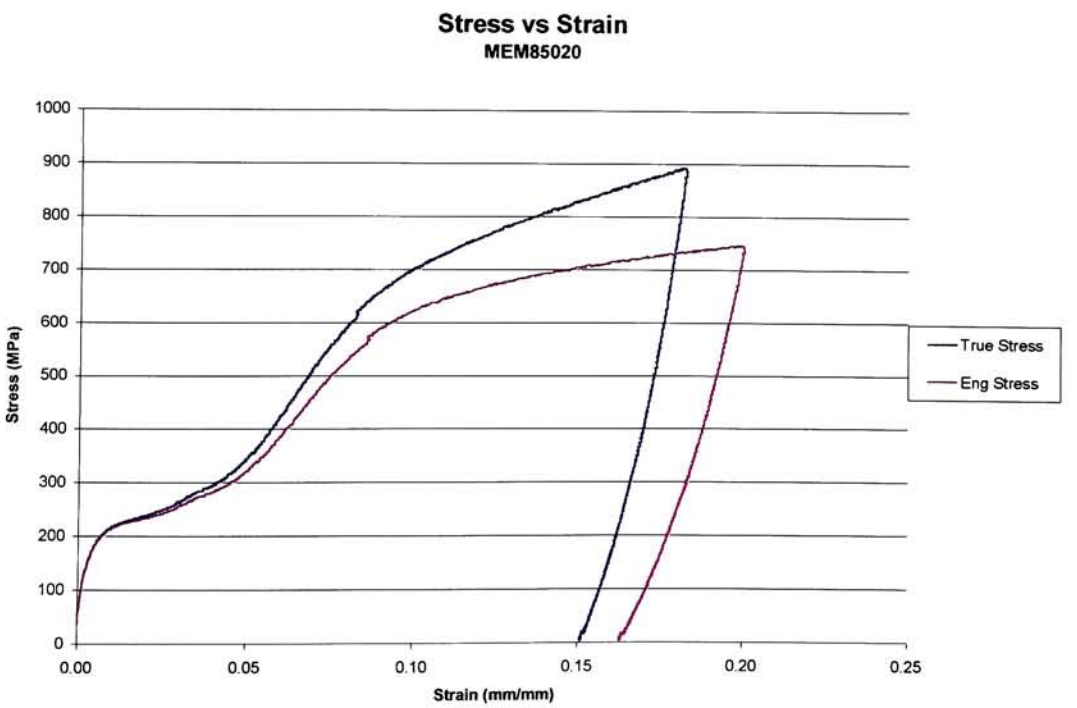
Stress vs Strain
MEM85020
1000
900
800
700
600
500
400
300
200
100
0
Stress (MPa)
0.00
0.05
0.10
0.15
0.20
0.25
Strain (mm/mm)
True Stress
Eng Stress

Appendix C

Fortran Program for numerically calculating the first derivative of a data set.

```
program MAIN
        implicit real*8(A-H,O-Z), integer*4(I-N)
        parameter (maxn = 1000)
        real*8 x(maxn), f(maxn), fe(maxn), ga(maxn), g(maxn), w(maxn)
        real*8 sw(maxn)
      character*20 infile

        pi = 4*atan(1.0)

      write(6,*) 'Enter input filename w/o extension (.in)'
      read (5,1) infile
1     format(A20)
      open (unit = 15, file=infile//'.in', status='old')

      n = 0
        do while (.true.)
        read(15, *, end=10) x(n+1), f(n+1)
        n = n + 1
        enddo

10      close(unit=15)
      nd = 1
        md = 4

        call DFABC(maxn, n, x, f, nd, md, fe, ga, g, w, sw)

      open(unit=16, file=infile//'.out', status='new')
        do 20 i = 1, n
          write(16,15) i, x(i), f(i), fe(i)
15      format(' ', I4, 3E14.5)
20      enddo
      close(unit=16)

        stop
        end

        subroutine DFABC(maxn, n, x, f, nd, md, fe, ga, g, w, sw)
        implicit real*8(A-H,O-Z), integer*4(I-N)
        real*8 x(maxn), f(maxn), fe(maxn), ga(maxn), g(maxn), w(maxn)
        real*8 sw(maxn)

        g(1) = 0
        g(n) = 0
        pi = 4.0*atan(1.0)
        xno = x(n) - x(1)
        fno = f(n) - f(1)
        am = fno/xno
        ac = f(1)

        do 100 i = 2, n-1
          g(i) = f(i) - am*(x(i)-x(1))-ac
```

```
100     enddo

        call DFT(maxn, n, g, ga)
        call SWI(maxn, n, nd, md, sw)

        call OPTALP(maxn, n, ga, sw, oalp)
        call WJ(maxn, n, oalp, sw, w)

        do 110 i = 1, n
          fe(i) = 0
110     enddo

        do 120 j = 2, n-1
          jm1 = j-1
          fj = pi*jm1
          s1 = ga(j)*w(jm1)*(fj**nd)
          f9 = nd*pi/2
          do 130 i = 1, n
            t = (x(i)-x(1))/xno
            c1 = sin(fj*t+f9)
            fe(i) = fe(i) + s1*c1
130       enddo
120     enddo
        c1 = xno**nd
        do 150 i = 1, n
          if (nd .eq. 1) fe(i) = fe(i)+fno
          fe(i) = fe(i)/c1
150     enddo
        return
        end

        subroutine DFT(maxn, n, g, ga)
        implicit real*8(A-H,O-Z), integer*4(I-N)
        real*8 ga(maxn), g(maxn)
        ga(1) = 0
        ga(n) = 0
        sc = 2.0/float(n-1)
        pi = 4*atan(1.0)

        do 1000 i = 2, n-1
          th = (i-1)/float(n-1)
          t1 = 0.5 -th


        if (abs(t1) .gt. 0.225) go to 1001

        th = pi*th
        x = cos(th)
        x2 = 2*x
        u1 = 0
        u2 = g(n-1)
        do 1005 ir = 2, n-2
          ir1 = n - ir
          u = x2 * u2 - u1 + g(ir1)
          u1 = u2
          u2 = u
1005    enddo
```

```
        ga(i) = u*sin(th)*sc
        go to 1000

1001    if (t1 .lt. 0.0) go to 1010

        th = pi*th
        s1 = sin(th/2)
        x1 = -4*s1*s1
        d1 = g(n-1)
        u1 = d1
        do 1006 ir = 2, n-2
          ir1 = n - ir
          d1 = x1 * u1 +d1 + g(ir1)
          u1 = d1 + u1
1006    enddo
        ga(i) = u1*sin(th)*sc
        go to 1000

1010    th = pi*th
        s1 = cos(th/2)
        x1 = 4*s1*s1
        d1 = g(n-1)
        u1 = d1
        do 1011 ir = 2, n-2
          ir1 = n - ir
          d1 = x1 * u1 - d1 + g(ir1)
          u1 = d1 - u1
1011    enddo
        ga(i) = u1 * sin(th) * sc

1000    enddo

        return
        end

        subroutine SWI(maxn, n, nd, md, sw)
        implicit real*8(A-H,O-Z), integer*4(I-N)
        real*8 sw(maxn)

        pi = 4*atan(1.0)
        md1 = md + 1
        do 2000 i = 1, n-1
          fi = pi * i/float(n-1)
          fi2 = fi * fi
          fin = fi2 ** nd
          s = 0
          do 2001 k = 1, md1
            s = s + fi2**(k-1)
2001      enddo
          sw(i) = fin * s
2000    enddo

        return
        end

        subroutine WJ(maxn, n, alp, sw, w)
        implicit real*8(A-H,O-Z), integer*4(I-N)
```

```
      real*8 w(maxn)
      real*8 sw(maxn)

      do 8000 i = 1, n-1
        w(i) = 1.0/(1.0 + alp*sw(i))
8000  enddo

      return
      end

      real*8 function FIALP(maxn, n, ga, sw, alp)
      implicit real*8(A-H,O-Z), integer*4(I-N)
      real*8 ga(maxn)
      real*8 sw(maxn)

      if (alp .le. 0) alp = 0

      s1 = 0
      s2 = 0
      do 6000 i = 1, n-1
        d1 = sw(i) / (1.0 + alp*sw(i))
        ip1 = i + 1
        ga9 = ga(ip1)
        s1 = s1 + ga9 * ga9 * d1
        s2 = s2 + dlog(d1)
6000  enddo
      fialp = (n-1) * dlog(s1) - s2
      return
      end

      subroutine OPTALP(maxn, n, ga, sw, oalp)
      implicit real*8(A-H,O-Z), integer*4(I-N)
      real*8 ga(maxn)
      real*8 sw(maxn)

      b = 1.0e-10
      st = 1.0e-8
      a1 = 1.5
      a2 = -0.25
      big = 1.0e8
      p = fialp(maxn, n, ga, sw, b)

5002  s1 = p
      s0 = -big
      x1 = 0.0
      bmin = b

5003  x2 = x1 + st
      b = bmin + x2
      b9 = bmin + x1
      if (b .eq. bmin + x1) go to 5099
      p = fialp(maxn, n, ga, sw, b)
      if (p .lt. s1) go to 5010
      if (s0 .ge. s1) go to 5011
      s0 = p
      x0 = x2
      st = a2 * st
```

```
        go to 5003

5010    x0 = x1
        s0 = s1
        x1 = x2
        s1 = p
        st = a1 * st
        go to 5003

5011    x0 = x0 - x1
        s0 = (s0 - s1) * st
        p = (p-s1)*x0
        if (p .eq. s0) go to 5018
        st = 0.5 * (p*x0 - s0 * st)/(p-s0)
        x2 = x1 + st
        b = bmin + x2
        if (b .eq. bmin+x1) go to 5020
        p = fialp(maxn, n, ga, sw, b)
        if (p .lt. s1) go to 5019

5018    b = bmin + x1
        p = s1
        go to 5020

5019    x1 = x2

5020    st = a2 * st
        go to 5002

5099    oalp = b

        return
        end
```

Appendix D

Lattice Parameters from X-ray Diffraction.

MEM85000

Linear Regression					
a	**b**	**c**	**γ (deg)**	**Volume**	
2.863	4.638	4.109	98.1	54.0056	
Nonlinear Regression					
a	**b**	**c**	**γ (deg)**	**Volume**	
2.879	4.614	4.097	98.0	53.9058	

MEM85003

Linear Regression					
a	**b**	**c**	**γ (deg)**	**Volume**	**% ΔV/V**
2.855	4.635	4.084	98.0	53.5096	-0.92
Nonlinear Regression					
a	**b**	**c**	**γ (deg)**	**Volume**	**% ΔV/V**
2.872	4.600	4.076	97.6	53.3646	-1.00

MEM85005

Linear Regression					
a	**b**	**c**	**γ (deg)**	**Volume**	**% ΔV/V**
2.874	4.635	4.097	97.9	54.0720	0.12
Nonlinear Regression					
a	**b**	**c**	**γ (deg)**	**Volume**	**% ΔV/V**
2.872	4.633	4.088	98.0	53.8690	-0.07

MEM85010

Linear Regression					
a	**b**	**c**	**γ (deg)**	**Volume**	**% ΔV/V**
2.846	4.617	4.118	97.1	53.7044	-0.56
Nonlinear Regression					
a	**b**	**c**	**γ (deg)**	**Volume**	**% ΔV/V**
2.841	4.607	4.104	97.3	53.2741	-1.17

MEM85015

Linear Regression					
a	**b**	**c**	**γ (deg)**	**Volume**	**% ΔV/V**
2.868	4.634	4.104	97.7	54.0439	0.07
Nonlinear Regression					
a	**b**	**c**	**γ (deg)**	**Volume**	**% ΔV/V**
2.869	4.630	4.095	97.5	53.9317	0.05

MEM85020

Linear Regression					
a	**b**	**c**	**γ (deg)**	**Volume**	**% ΔV/V**
2.866	4.600	4.102	97.0	53.6775	-0.61
Nonlinear Regression					
a	**b**	**c**	**γ (deg)**	**Volume**	**% ΔV/V**
2.849	4.678	4.079	96.9	53.9793	0.14

Appendix E

Transformation Temperatures estimated from DMA

MEM85000

DMA	A_s			A_f			M_s			M_f		
Freq (Hz)	0.2	2	20	0.2	2	20	0.2	2	20	0.2	2	20
Run #												
1	97.5	92.5	96.0	105.5	101.5	105.5	73.0	73.0	73.0	51.5	51.5	50.5
2	94.5	95.5	92.5	101.5	105.0	101.0	77.0	77.5	78.5	53.5	53.0	56.0
3	93.5	91.5	91.5	99.5	98.5	98.0	79.0	78.0	79.0	58.0	57.0	57.0

MEM85003

DMA	A_s			A_f			M_s			M_f		
Freq (Hz)	0.2	2	20	0.2	2	20	0.2	2	20	0.2	2	20
Run #												
1	109.5	109.5	109.5	118.5	116.5	116.0	75.0	75.5	77.5	51.5	51.0	51.5
2	93.5	89.5	92.5	99.5	100.5	100.5	73.5	71.5	71.0	51.5	51.5	52.5
3	93.0	92.5	89.5	103.0	103.0	102.5	76.5	75.5	74.5	50.5	48.5	50.0

MEM85005

DMA	A_s			A_f			M_s			M_f		
Freq (Hz)	0.2	2	20	0.2	2	20	0.2	2	20	0.2	2	20
Run #												
1	119.0	121.5	121.5	126.0	125.5	125.5	71.5	72.0	70.5	50.5	49.5	45.0
2	94.0	93.5	93.5	104.0	102.5	101.5	71.5	73.0	70.5	46.5	44.5	42.5
3	92.5	91.5	91.5	103.5	102.0	101.5	70.0	71.5	71.0	48.5	48.5	49.0

MEM85010

DMA	A_s			A_f			M_s			M_f		
Freq (Hz)	0.2	2	20	0.2	2	20	0.2	2	20	0.2	2	20
Run #												
1	148.5	148.0	147.5	156.0	152.0	153.0	75.0	75.0	75.5	38.5	41.5	41.5
2	98.5	96.5	98.5	112.0	110.5	109.0	76.5	78.5	77.5	45.5	37.0	37.5
3	94.0	93.5	93.5	111.0	111.0	110.5	75.5	77.5	77.0	44.5	40.5	41.5

MEM85015

DMA	A_s			A_f			M_s			M_f		
Freq (Hz)	0.2	2	20	0.2	2	20	0.2	2	20	0.2	2	20
Run #												
1	154.5	153.0	152.5	162.0	160.0	160.5	81.5	83.0	81.5	53.5	50.0	51.0
2	103.5	100.0	100.0	118.0	120.0	118.5	77.5	78.0	78.5	47.5	45.0	43.0
3	96.0	95.0	94.5	110.5	112.5	114.0	78.5	80.0	78.5	47.5	44.0	44.0

MEM85020

DMA	A_s			A_f			M_s			M_f		
Freq (Hz)	0.2	2	20	0.2	2	20	0.2	2	20	0.2	2	20
Run #												
1	159.5	159.0	157.0	179.0	179.0	179.0	79.0	82.0	80.5	44.0	41.0	61.0
2	94.0	92.5	95.5	124.0	123.0	114.0	84.0	86.0	85.5	43.0	49.0	49.0
3	87.5	86.0	85.5	114.0	114.0	113.0	83.0	88.0	86.0	46.5	48.0	49.0

Appendix F

DSC Curves

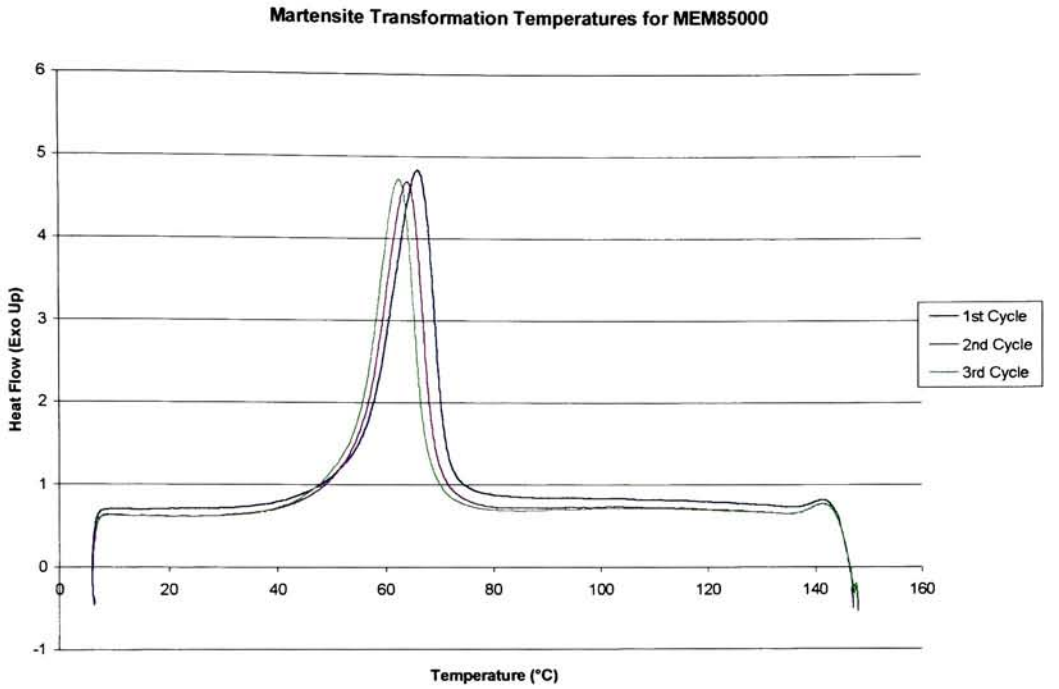

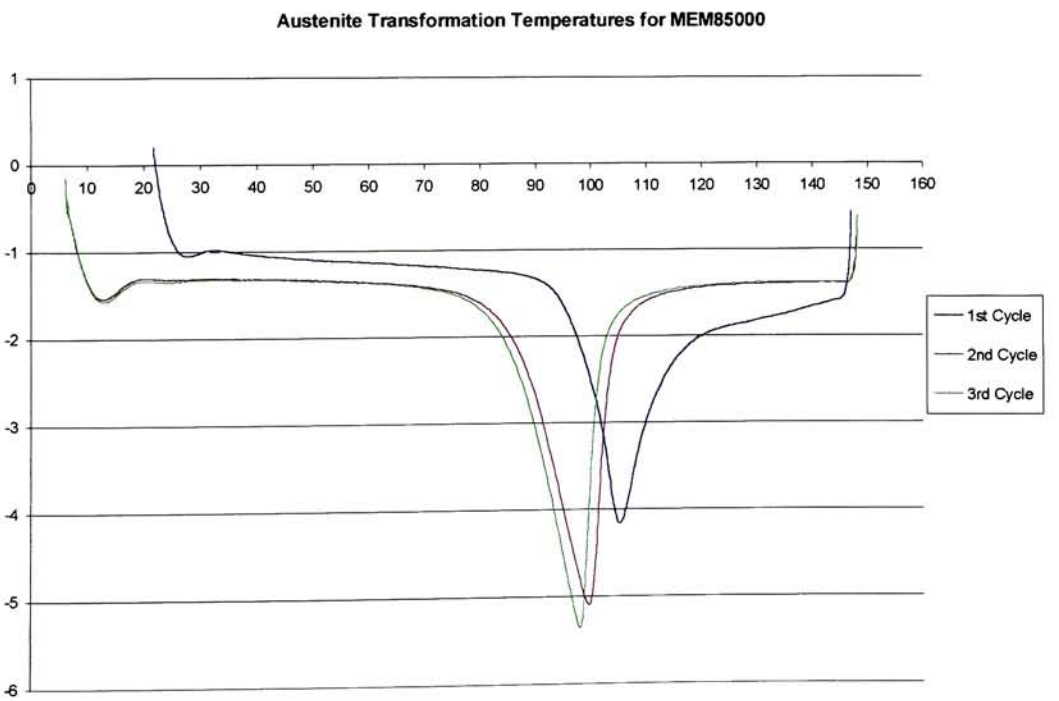

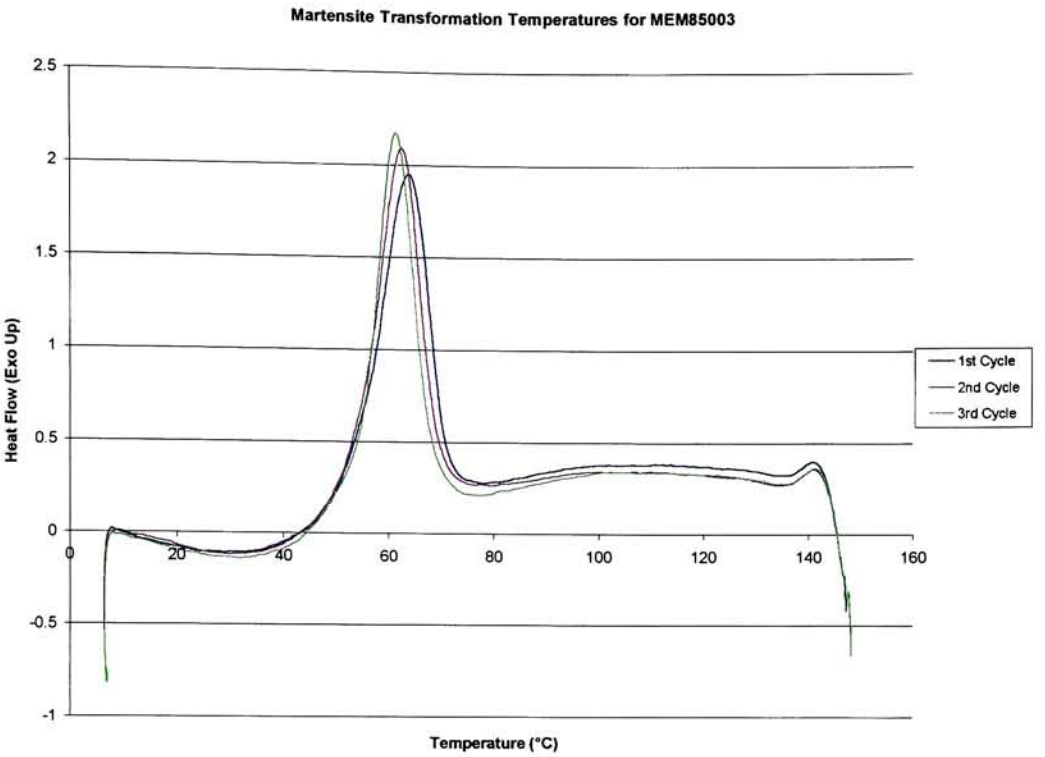
Martensite Transformation Temperatures for MEM85003
Heat Flow (Exo Up)
Temperature (°C)
1st Cycle
2nd Cycle
3rd Cycle

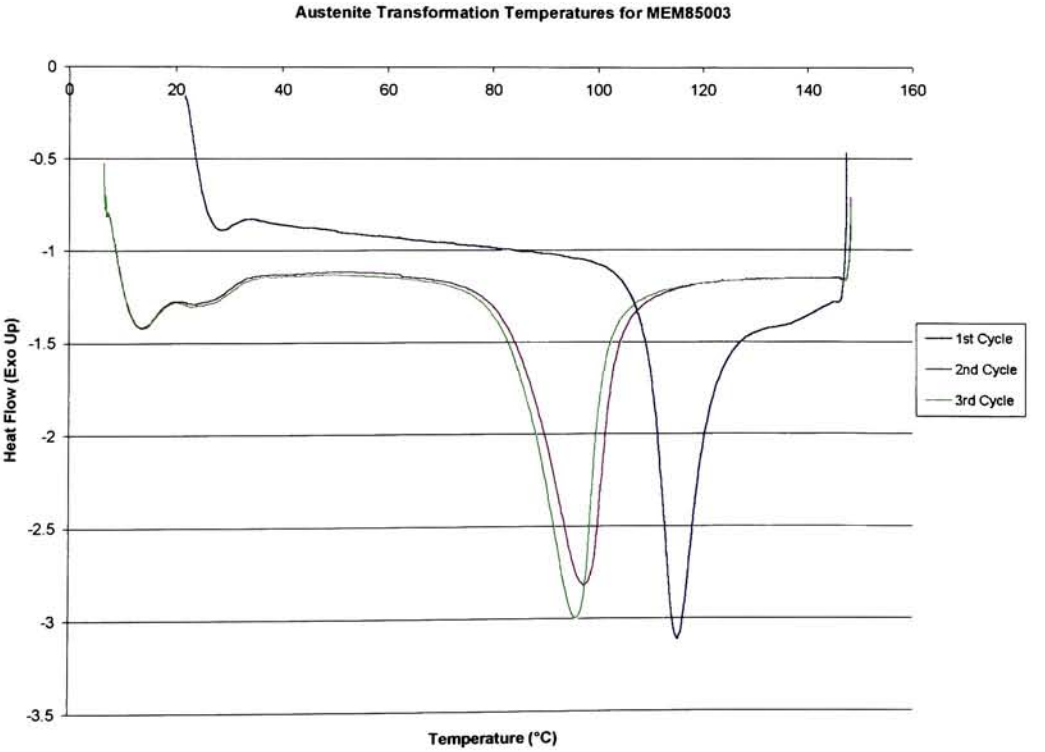
Austenite Transformation Temperatures for MEM85003
Heat Flow (Exo Up)
Temperature (°C)
1st Cycle
2nd Cycle
3rd Cycle

Martensite Transformation Temperatures for MEM85005

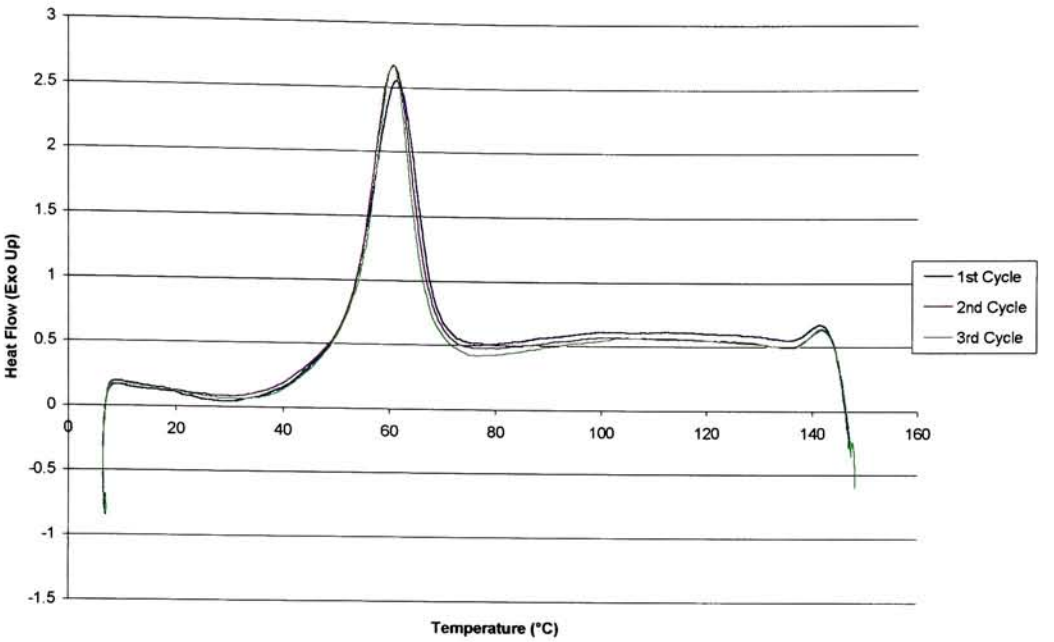

Austenite Transformation Temperatures for MEM85005

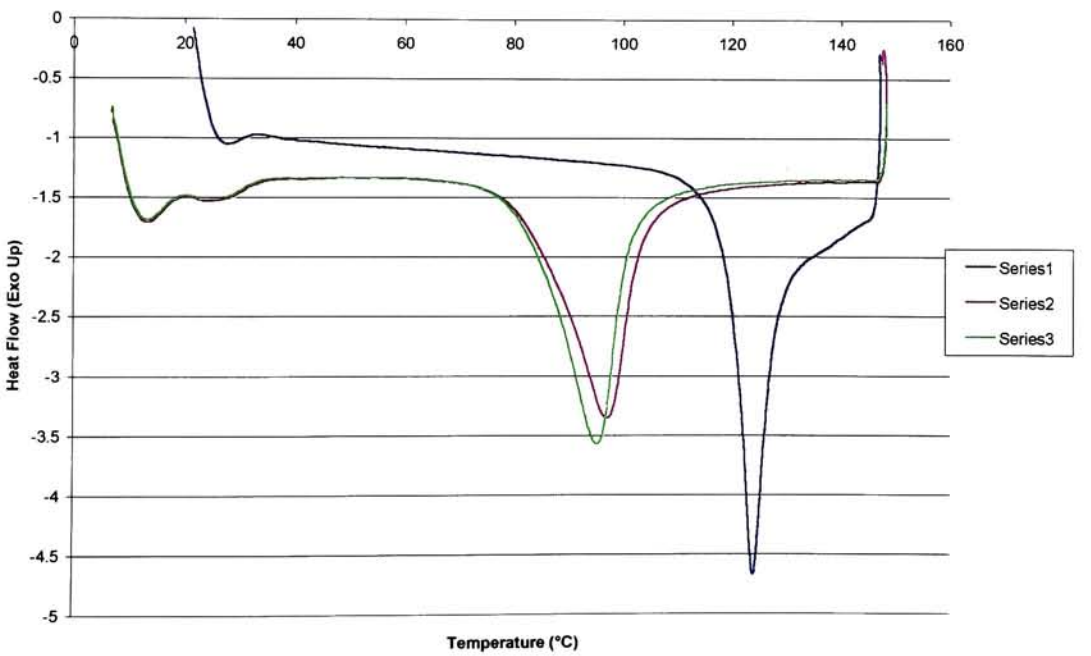

Martensite Transformation Temperatures for MEM85010

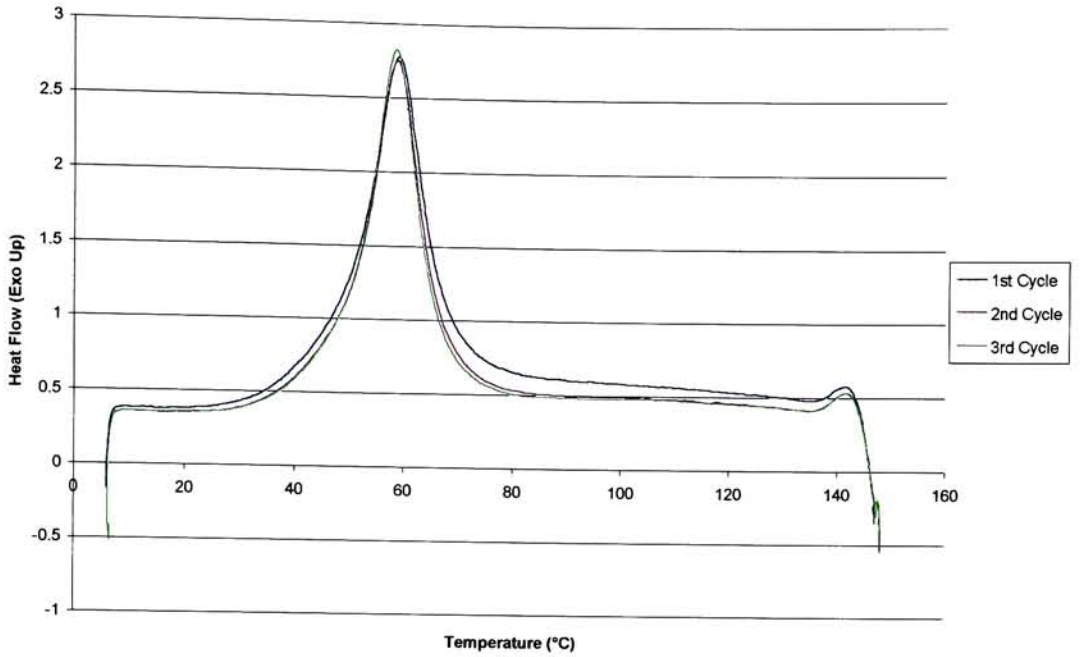

Austenite Transformation Temperatures for MEM85010

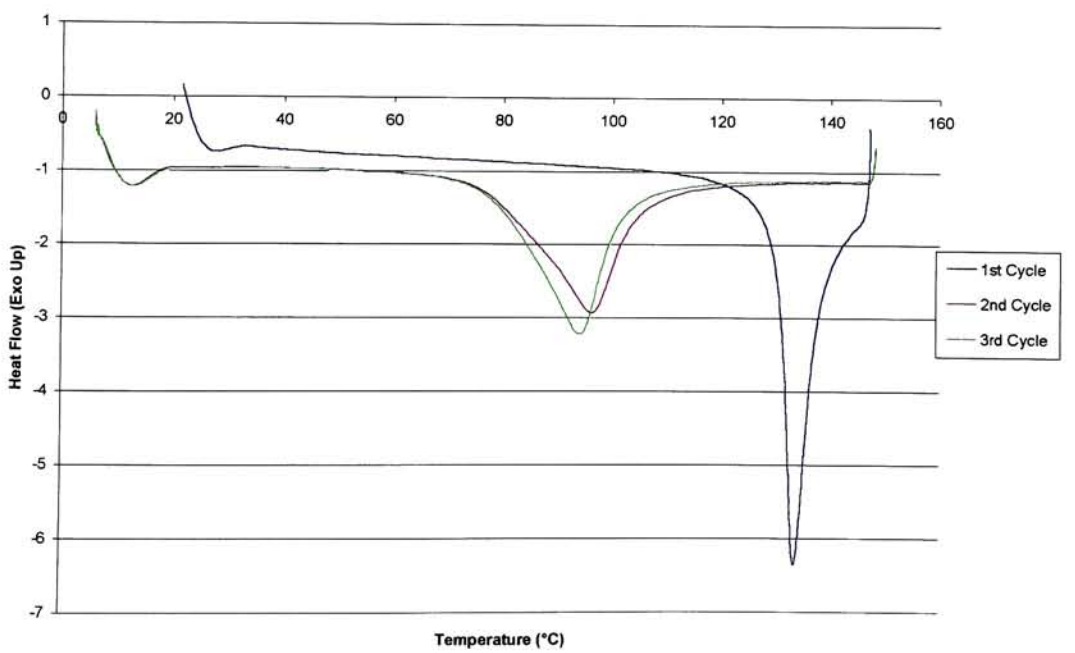

Martensite Transformation Temperatures for MEM85015

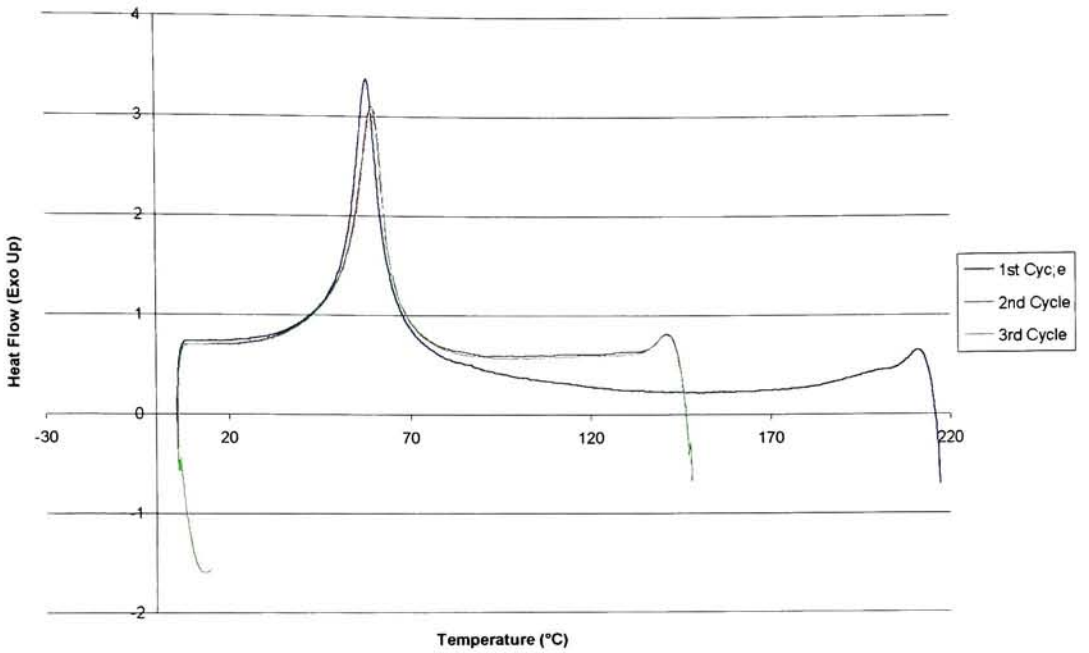

Austenite Transformation Temperatures for MEM85015

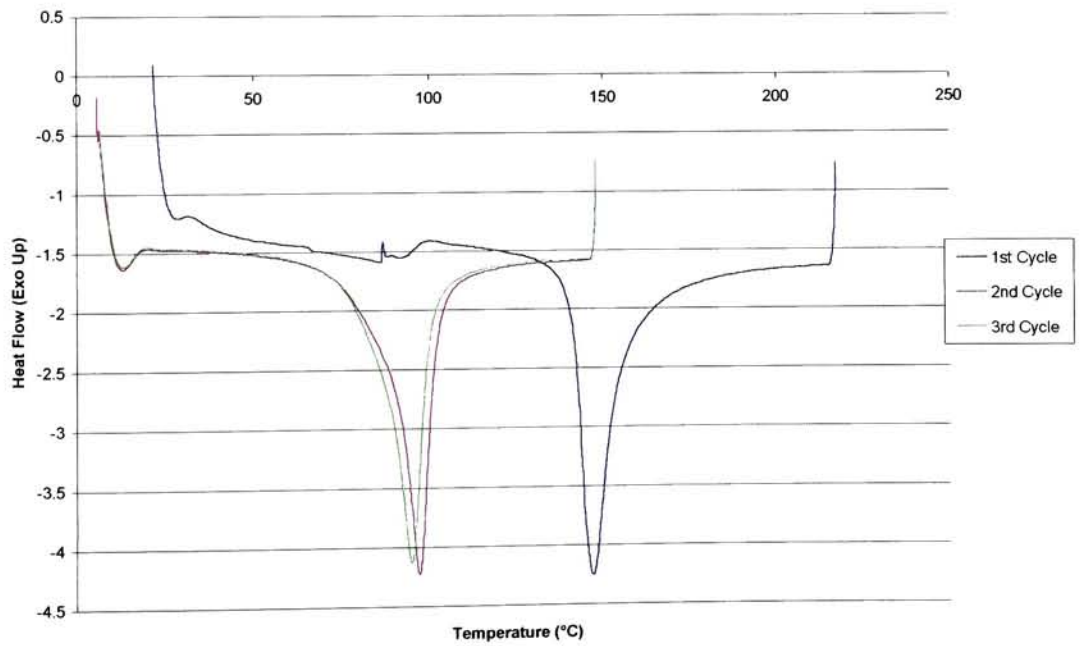

Martensite Transformation Temperatures for MEM85017

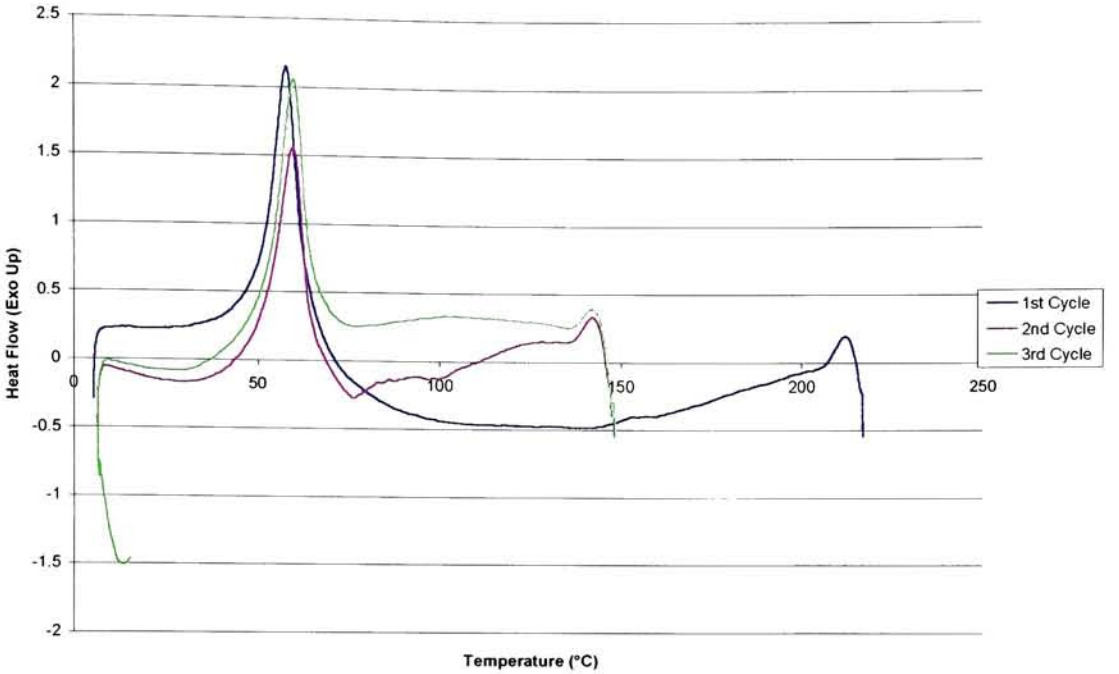

Austenite Transformation Temperatures for MEM85017

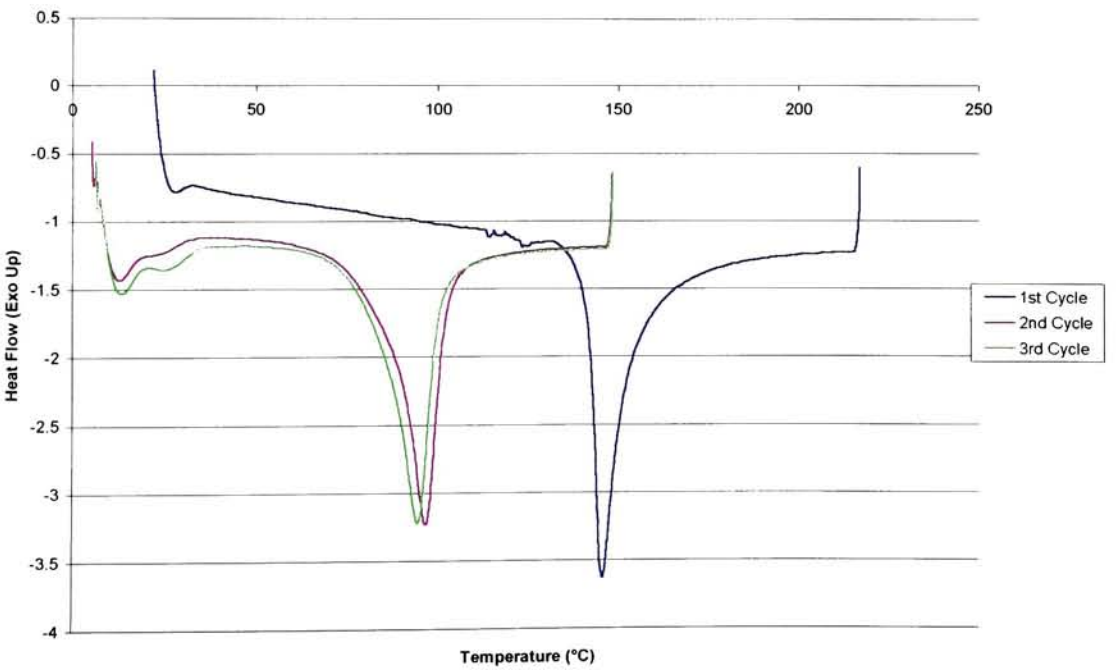

Martensite Transformation Temperatures for MEM85020

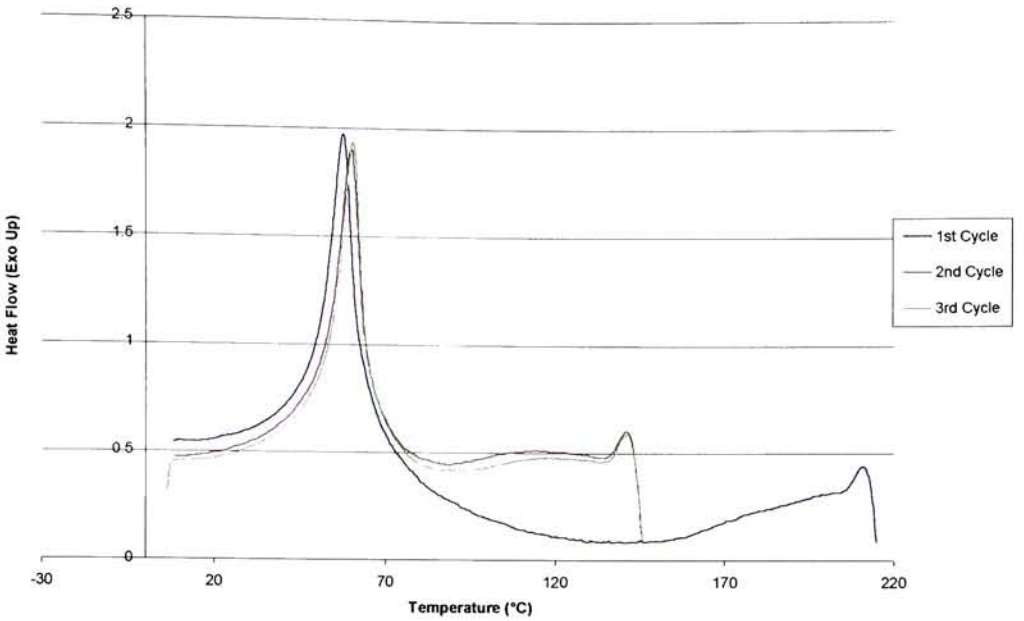

Austenite Transformation Temperatures for MEM85020

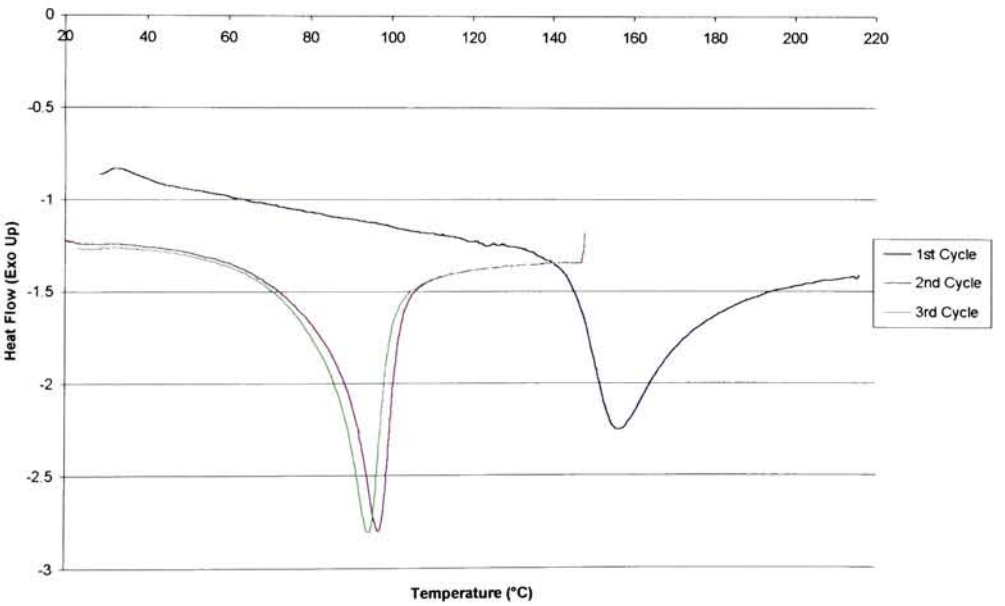

Appendix G

DMA Heating and Cooling Curves

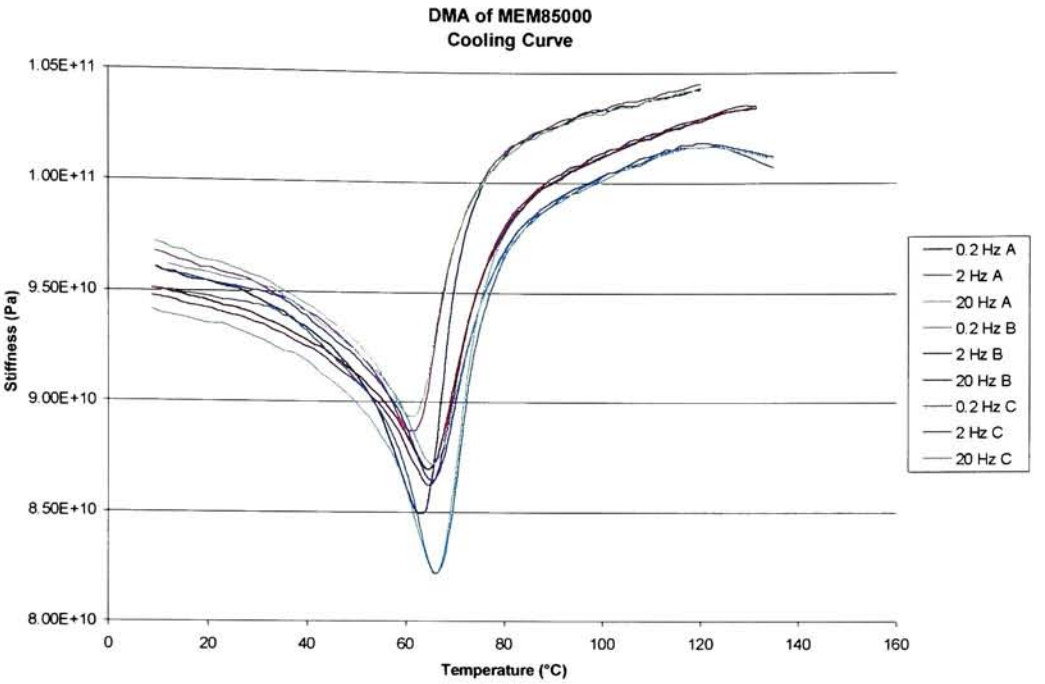

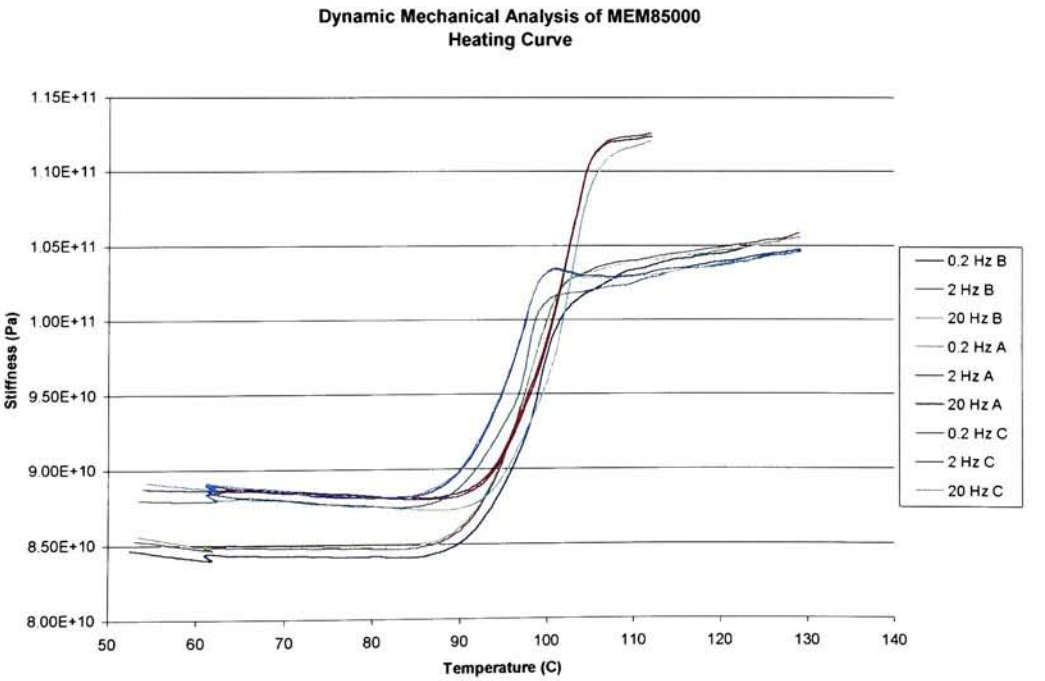

A = First Cycle, B = Second Cycle, C = Third Cycle

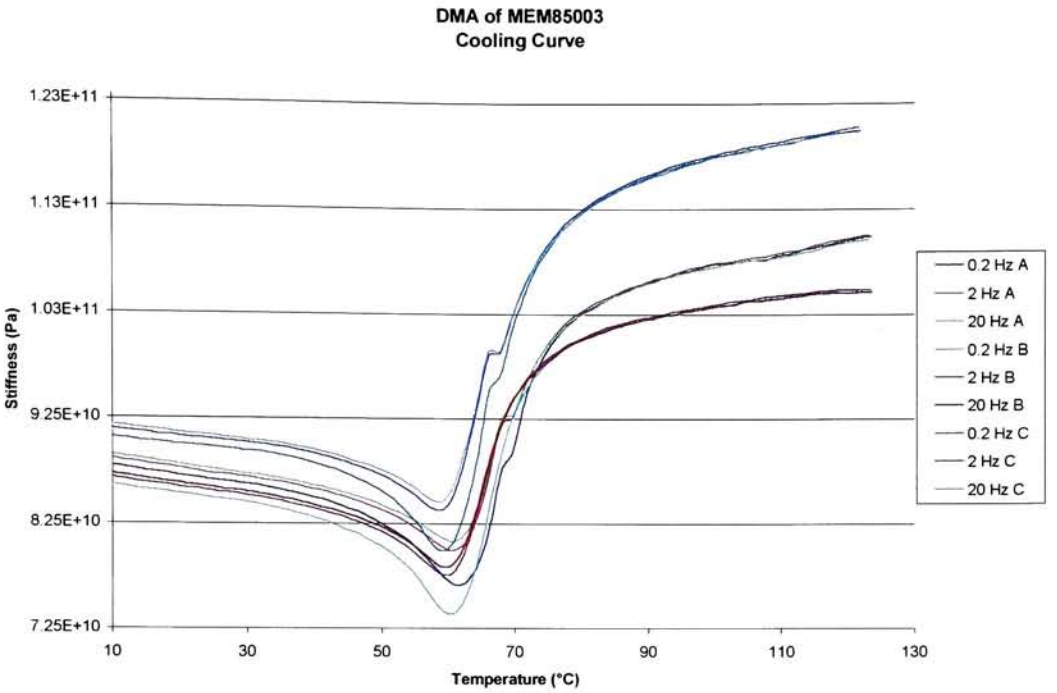

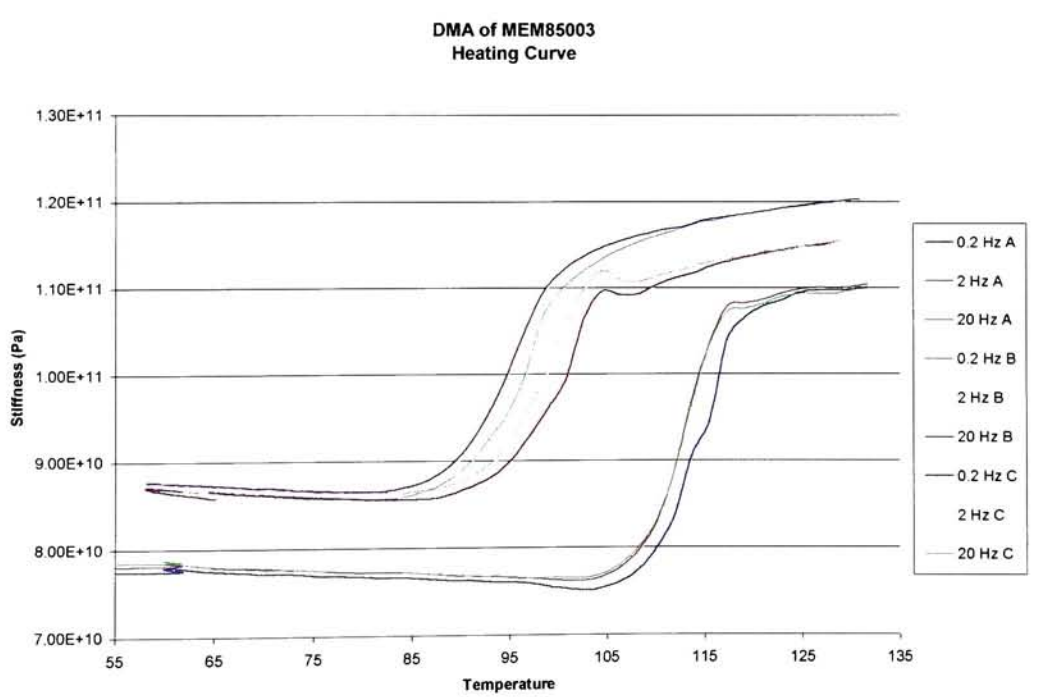

A = First Cycle, B = Second Cycle, C = Third Cycle

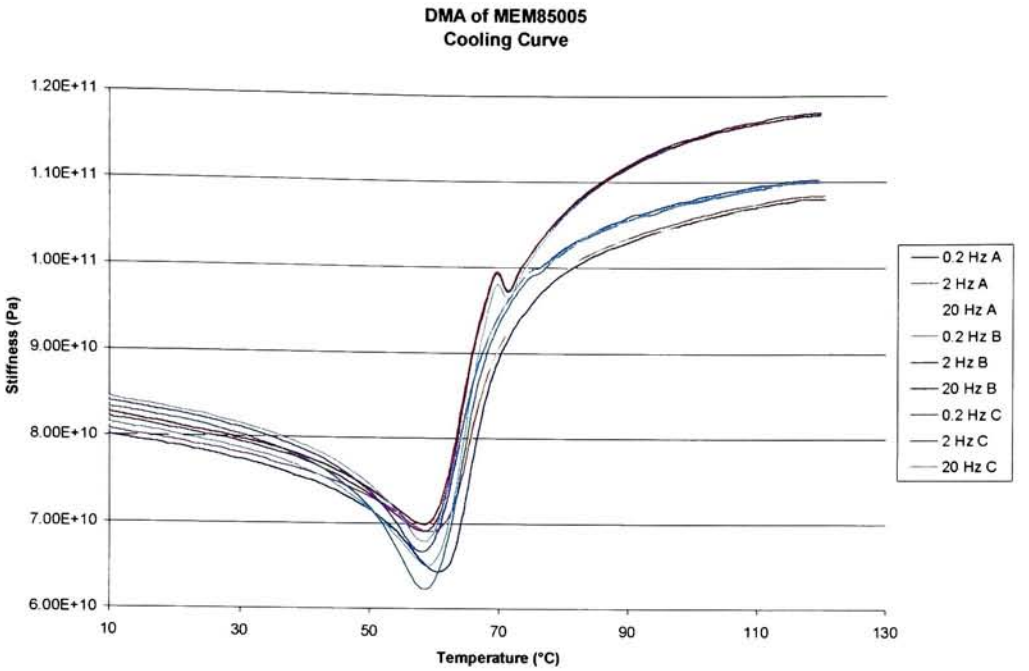

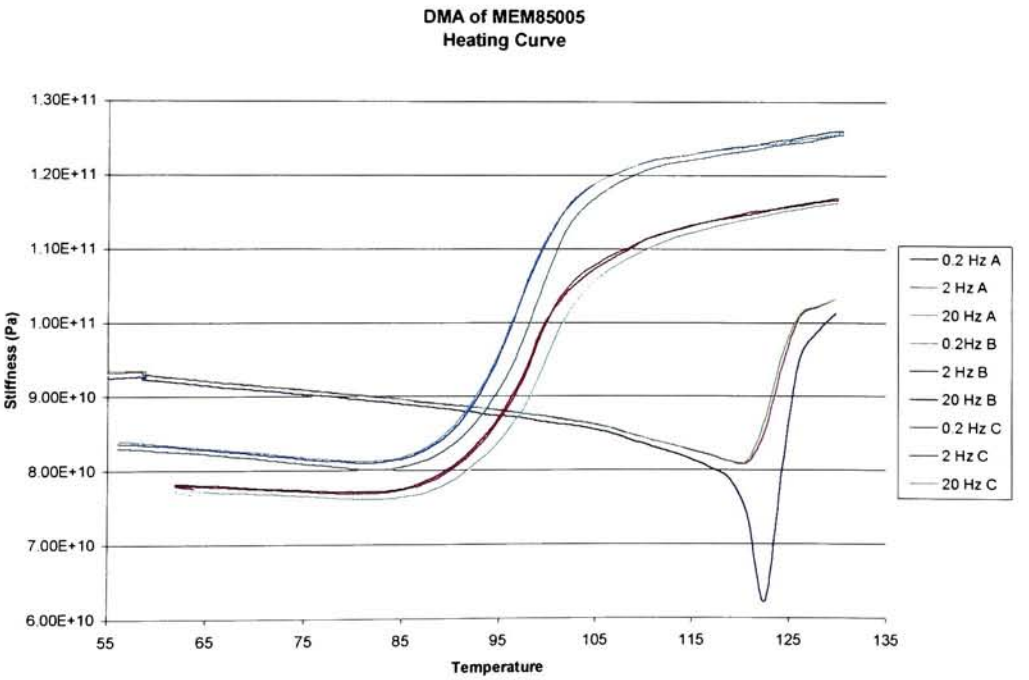

A = First Cycle, B = Second Cycle, C = Third Cycle

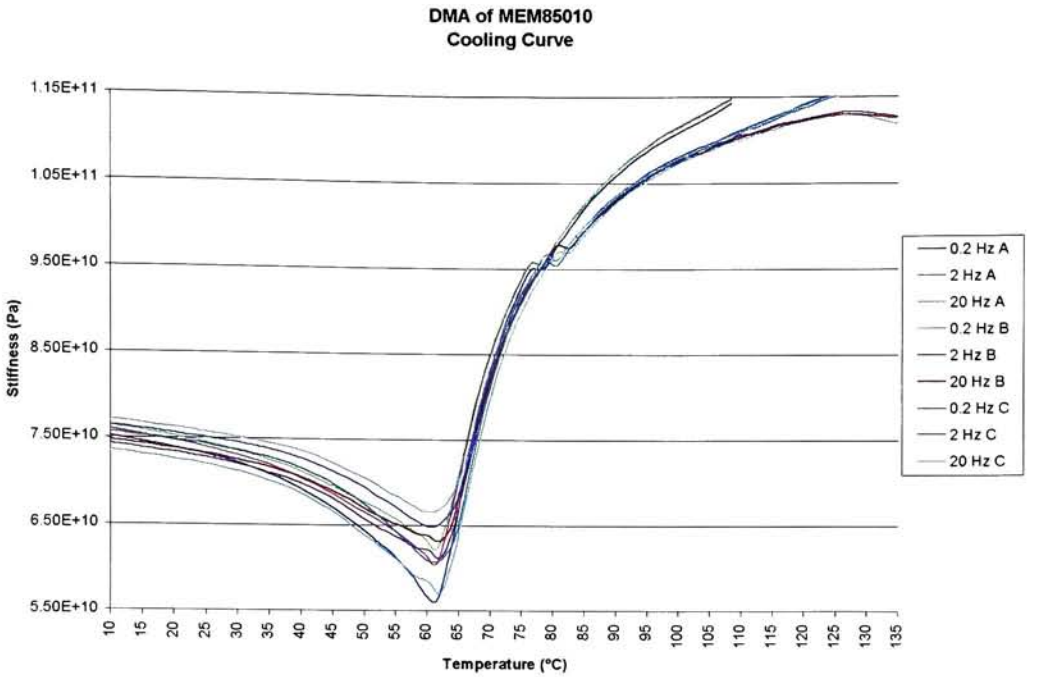

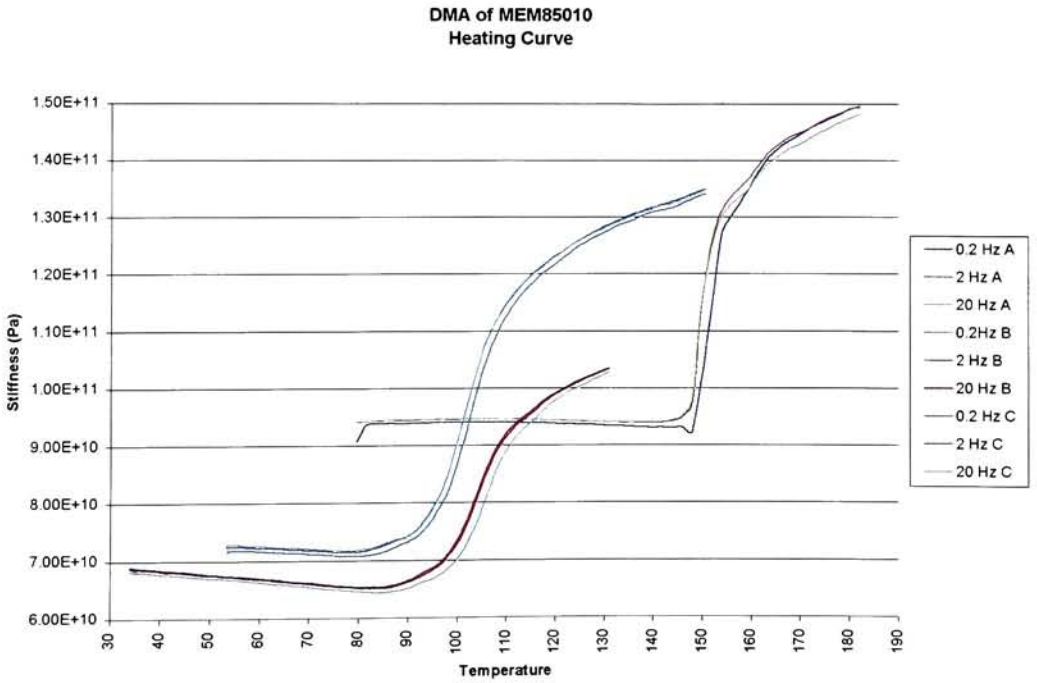

A = First Cycle, B = Second Cycle, C = Third Cycle

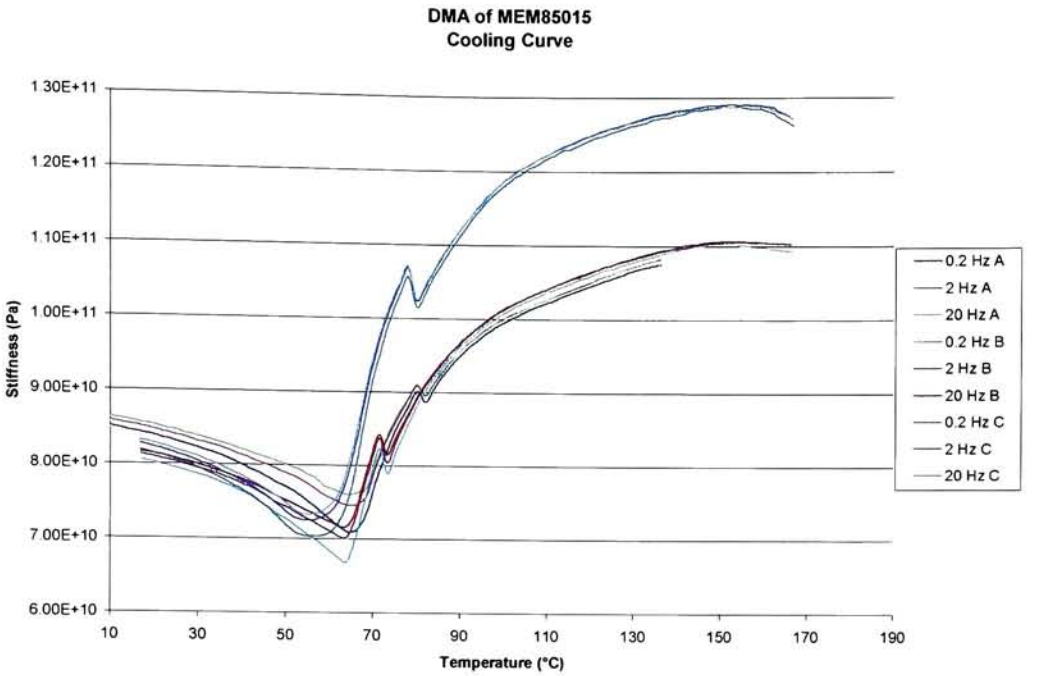

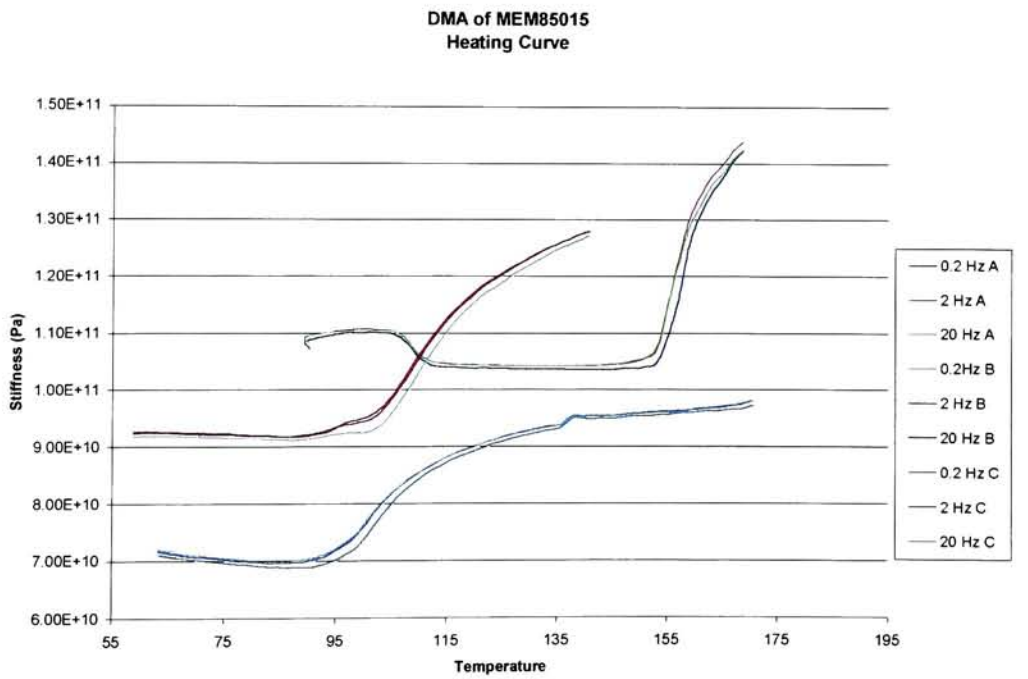

A = First Cycle, B = Second Cycle, C = Third Cycle

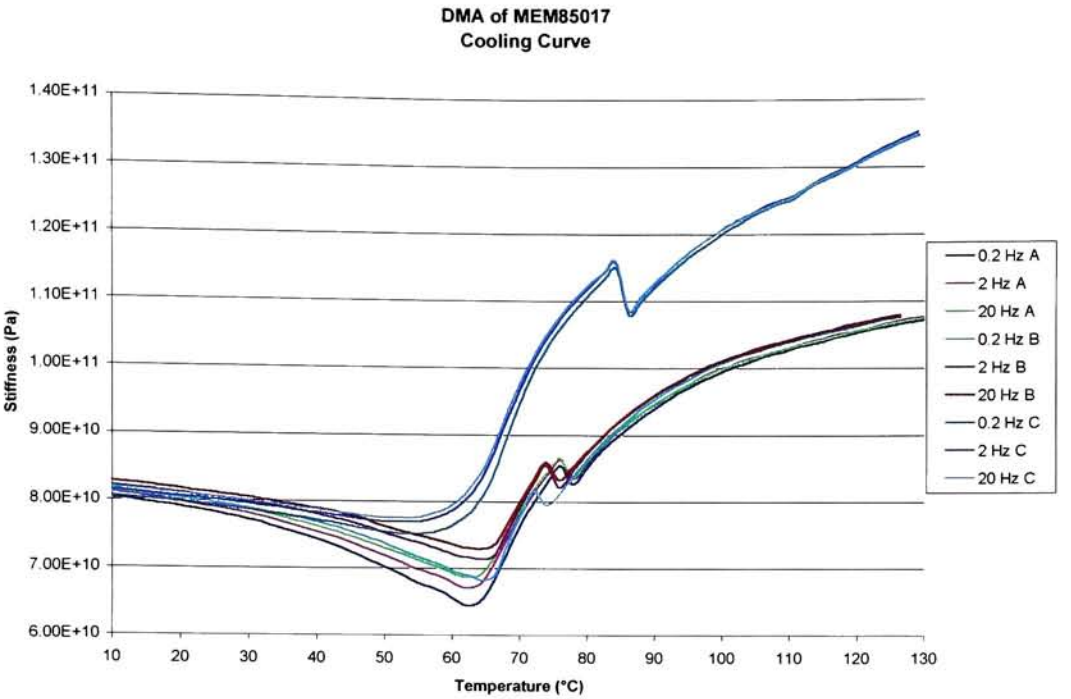

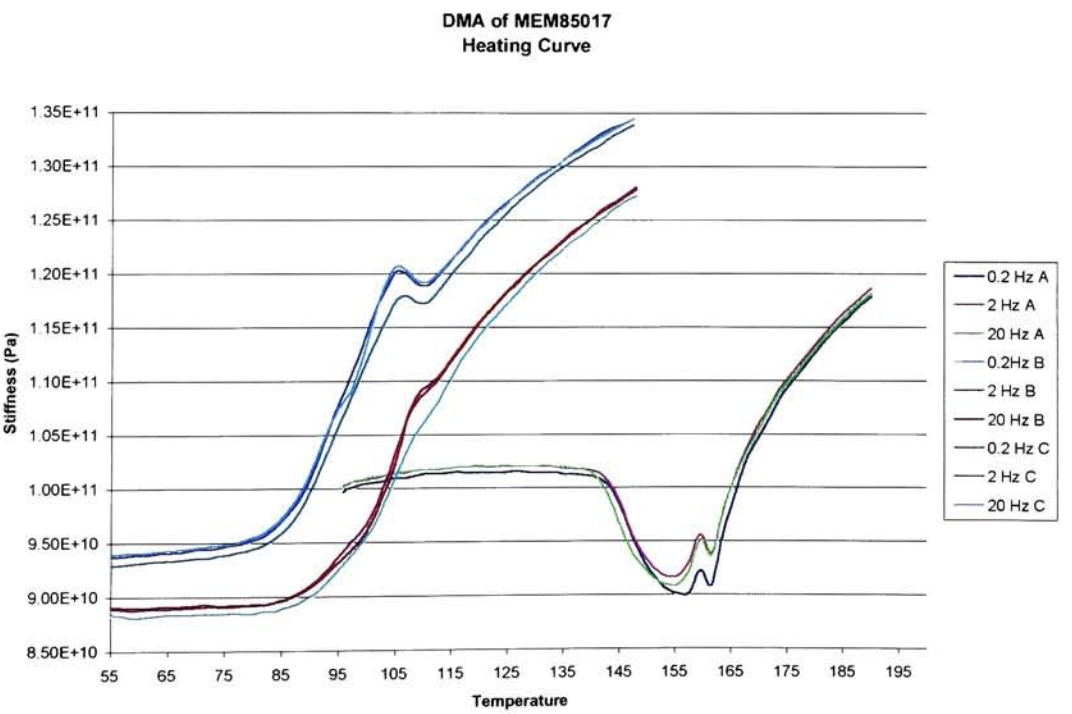

A = First Cycle, B = Second Cycle, C = Third Cycle

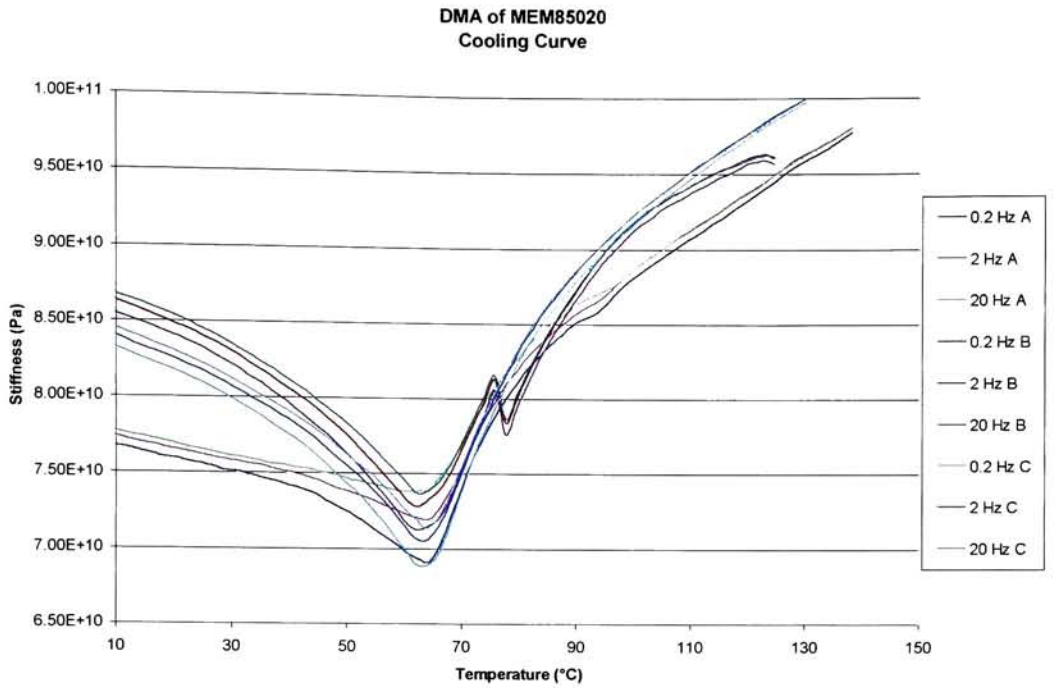

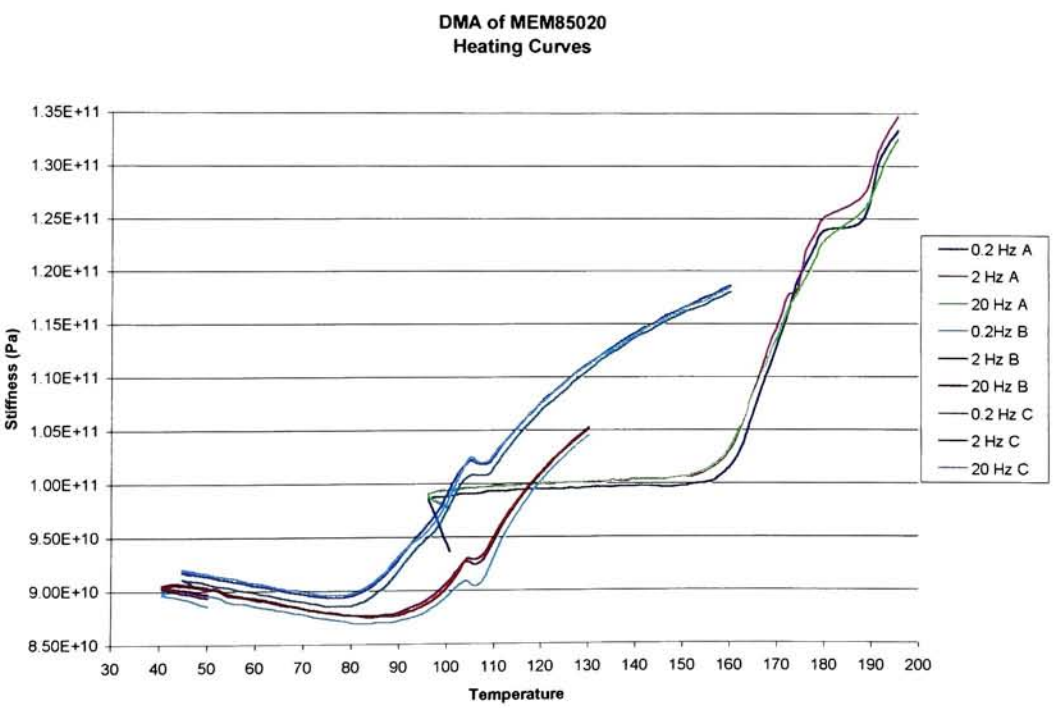

A = First Cycle, B = Second Cycle, C = Third Cycle

References

1 Duerig, T.W., K.N. Melton, D Stockel, C.M. Wayman. *Engineering Aspects of Shape Memory Alloys.* Butterworth-Heinemann: Boston, 1990.

2 K. Otsuka, and C.M. Wayman. *Shape Memory Materials.* Cambridge University Press: New York, 1998.

3 Funakubo, Hiroyasu. *Shape Memory Alloys.* Gordon and Breach Science Publishers: New York. 1987.

4 Askeland, Donald. *The Science and Engineering of Materials.* PWS Publishing Company: Boston, 1994.

5 Sinclair, R and G. M. Michael. "The Structure of TiNi Martensite." *Acta crystallographica,* B37 (1981) 1803-1807.

6 Miyazaki, S. and M. Fremond. *Shape Memory Alloys.* Springer-Verlag: New York, 1996.

7 Bhattagharya, K. "Self-Accommodation in Martensite." *Archive for Rational Mechanics and Analysis.* V.120 1992 pp 201.244.

8 Dieter, George E. *Mechanical Metallurgy.* McGraw-Hill Book Company, New York 1986.

9 Hodgson, Darel E, Ming H. Wu and Robert J. Biermann. "Shape Memory Alloys," *Metals Handbook 10th Ed. Vol 2.* ASM International: Materials Park, 1990

10 Duerig, T.W. and A.R. Pelton. "Ti-Ni Shape Memory Alloys." Materials Properties Handbook, Titanium Alloys. ASM International Materials Park, 1998.

11 Liu, Y., Z. Xie, J Van Humbeeck and L. Delaey. "Some Results on the Detwinning Process in NiTi Shape Memory Alloys." *Scripta Materialia,* 41(1999): 1273-1281.

12 Filip, Peter, and Karel Mazanec. "Influence of workhardening on the reactive stress in a TiNi shape memory alloy." *Materials Science and Engineering,* A174, (1994): L41-L43.

13 Huang, W and Y. L. Wong. "Effects of pre-strain on transformation temperatures of NiTi shape memory alloy." *Journal of Materials Science Letters,* 18 (1999): 1797-1798.

14 Beer, Ferdinand P. and E. Russel Johnson Jr. *Mechanics of Materials.* New York: McGraw-Hill, Inc. 1992.

15 Menard, Kevin P. *Dynamic Mechanical Analysis: A Practical Introduction.* CRC Press: New York, 1999.

16 Cullity, B. D. *Elements of X-ray Diffraction.* Addison-Wesley Publishing Company: Reading, 1978.

17 Hornbogen, Erhard and Erhard Kobus. "Characterization of Shape Memory Alloys by Hardness Indentations." *Praktische Metallographi,* 30 (1993) 507-518.

18 ASTM E384 Standard Test Method for Microhardness of Materials.

19 Wiesendanger, Roland. *Scanning Probe Microscopy and Spectroscopy.* Cambridge University Press: New York, 1994.

20 Information regarding Atomic Force Microscopy and Tapping mode taken from Digital Instruments, Veeco Metrology Group, Santa Barbara, CA. http://www.di.com.

21 Macleod, Allan J. "Numerical Differentiation by the Regularization Method." *Communications in Applied Numerical Methods.* 2, (1986): 625-632.

22 Cullum, Jane. "Numerical Differentiation and Regularization". *SIAM Journal of Numerical Analysis,* 8, (1971): 254-265.

23 ASTM E 1356-91 Standard Test Method for Glass Transition Temperatures by Differential Scanning Calorimetry or Differential Thermal Analysis.

24 ASTM D 5023-95a Measuring the Dynamic Mechanical Properties of Plastics Using Three Point Bending.

25 ASTM E 1640-94 Test Method for Assignment of the Glass Transition Temperature By Dynamic Mechanical Analysis.

26 Huang, W. "Effects of internal stress and martensite variants on phase transformation of NiTi shape memory alloy." *Journal of Materials Science Letters,* 7 (1998): 1843-1844.

27 Wu, S. K., L. C. Lin, and P. C. Cheng. "Multi-Strengthening effects on the martensitic transformation temperatures of TiNi shape Memory alloys." *Journal of Materials Science,* 34 (1999) 5669-5675.

28 Carballo, M., Z. J. Pu and K.H. Wu. "Variation of Electrical Resistance and the Elastic Modulus of Shape Memory Alloys under Different Loading and Temperature Conditions." *Journal of Intelligent Material Systems and Structures, 6 (1995) 557-565.*